# Development of Active Photocatalysts for $CO_2$ Conversion by High-Pressure Torsion

# （高圧ねじりによる $CO_2$ 変換用活性光触媒の開発）

**Akrami Saeid**

アクラミ サイード

**March 2023**

**Doctor of Engineering at Department of Life Science and Applied Chemistry**

**Nagoya Institute of Technology**

**Gokiso-Cho, Showa-Ku, Nagoya, Aichi, 466-8555 Japan**

# Abstract

Excessive $CO_2$ emission from fossil fuel usage has resulted in global warming and environmental crises. To solve this problem, photocatalytic conversion of $CO_2$ to CO or useful components is a new strategy that has received significant attention. The main challenge in this regard is exploring photocatalysts with high efficiency for $CO_2$ photoreduction, as discussed in chapter 1. Severe plastic deformation (SPD) through the high-pressure torsion (HPT) process was used in this study to develop novel active photocatalysts for $CO_2$ conversion. These active photocatalysts were designed based on four main strategies (i) oxygen vacancy and strain engineering, (ii) stabilization of high-pressure phases, (iii) synthesis of defective high-entropy oxides (HEOs), and (iv) synthesis of low-bandgap high-entropy oxynitrides (HEONs).

In chapter 2, to overcome the drawbacks of $BiVO_4$ for $CO_2$ conversion, oxygen vacancies and lattice strain are simultaneously introduced in this oxide using the HPT process. The processed material not only shows a low recombination rate and enhanced conduction band level but also exhibits bandgap narrowing. The oxygen-deficient and highly-strained $BiVO_4$ shows a high photocatalytic $CO_2$ conversion rate with an activity comparable to the P25 $TiO_2$ benchmark photocatalyst. The enhancement of photocatalytic activity is discussed based on the modification of band structure, enhanced light absorbance, the lifetime of excited electrons, and the role of oxygen vacancies as activation sites for $CO_2$ photoreduction. This chapter introduces a feasible pathway to develop active photocatalysts for $CO_2$ conversion by lattice strain and defect engineering.

In chapter 3, the nanocrystalline high-pressure $TiO_2$-II polymorph, synthesized by HPT, shows higher photocurrent and better photocatalytic activity for $CO_2$ to CO conversion compared to the anatase phase. The photocatalytic activity of the material is further enhanced by the thermal annihilation of oxygen vacancies generated in the bulk of $TiO_2$-II during the high-pressure treatment. The high potential of the $TiO_2$-II phase for $CO_2$ conversion is discussed based on the light absorbance, band structure, charge carrier mobility and $CO_2$ adsorption.

In chapter 4 and inspired by the inherent defective and strained structure of HEOs, photocatalytic $CO_2$ conversion is examined on a dual-phase $TiZrNbHfTaO_{11}$ synthesized by a two-step mechanical alloying by HPT and high-temperature oxidation. The HEO, which had various structural defects, showed simultaneous photocatalytic activity for $CO_2$ to CO and $H_2O$ to $H_2$

conversion without the addition of a co-catalyst. The photocatalytic activity of this HEO for $CO_2$ conversion was better than conventional photocatalysts such as anatase $TiO_2$ and $BiVO_4$ and similar to P25 $TiO_2$. The high activity of HEO was discussed in terms of lattice defects, lattice strain, light absorbance, band structure, photocurrent generation and charge carrier mobility to activation centers. The current study confirms the high potential of HEOs as a new family of photocatalysts for $CO_2$ conversion.

In chapter 5, a HEON was introduced as an active photocatalyst for photoreduction. The material had a chemical composition of $TiZrNbHfTaO_6N_3$ and was produced by HPT processing followed by oxidation and nitriding. It showed higher photocatalytic $CO_2$ to CO conversion compared to corresponding high-entropy oxide, benchmark photocatalyst P25 $TiO_2$, and almost all catalysts introduced in the literature. The high activity of this oxynitride, which also showed good chemical stability, was attributed to the large absorbance of light and easy separation of electrons and holes, the low recombination of charge carriers, and the high $CO_2$ adsorption on the surface. These findings introduce high-entropy oxynitrides as promising photocatalysts for $CO_2$ photoreduction.

# Contents

# Chapter 1. Introduction

## 1.1. Background

Nowadays, environmental crises especially global warming caused by $CO_2$ emissions from burning fossil fuels and humankind activities are considered one of the most significant challenges in the world. Reduction of $CO_2$ to reactive CO gas or useful components and fuels such as $CH_4$ and $CH_3OH$ using photocatalysts is one of the clean and new strategies which is developing rapidly [1-3]. The function of photocatalysts is the acceleration of reduction and oxidation reactions under light irradiation. Reduction and oxidation reactions occur on the surface of a photocatalyst using the electrons and holes, respectively to promote the $CO_2$ conversion [1-3]. In photocatalytic $CO_2$ conversion, photoexcited electrons contribute to the conversion of $CO_2$ to reactive and useful components such as carbon monoxide (CO), formic acid (HCOOH), formaldehyde (HCHO), methanol ($CH_3OH$) and methane ($CH_4$) [1-3]. The mechanism of photocatalytic $CO_2$ conversion is shown in Figs. 1a. To perform the reactions, a photocatalyst should have some features including high light absorbance, appropriate band structure, low recombination rate of electrons and holes, easy migration of charge carriers, and high surface affinity to adsorb $CO_2$ with abundant active sites [3,4].

Semiconductors such as $TiO_2$ [5-7], g-$C_3N_4$ [8,9], and $BiVO_4$ [10-12] are typical photocatalysts that have been engineered by various strategies to enhance the catalytic efficiency for $CO_2$ conversion. Doping with impurities [13-15], defect engineering [16,17], strain engineering [18,19], mesoporous structure production [20], and heterojunction introduction [21,22] are some of the most promising strategies which have been used so far to improve the optical properties and catalytic activity of various photocatalysts. Among these strategies, doping with impurities is the most investigated and feasible method, but impurities can increase the recombination rate of electrons and holes [13-15]. Therefore, finding new strategies to improve the photocatalytic activity and suppress the recombination rate of electrons and holes is a key issue.

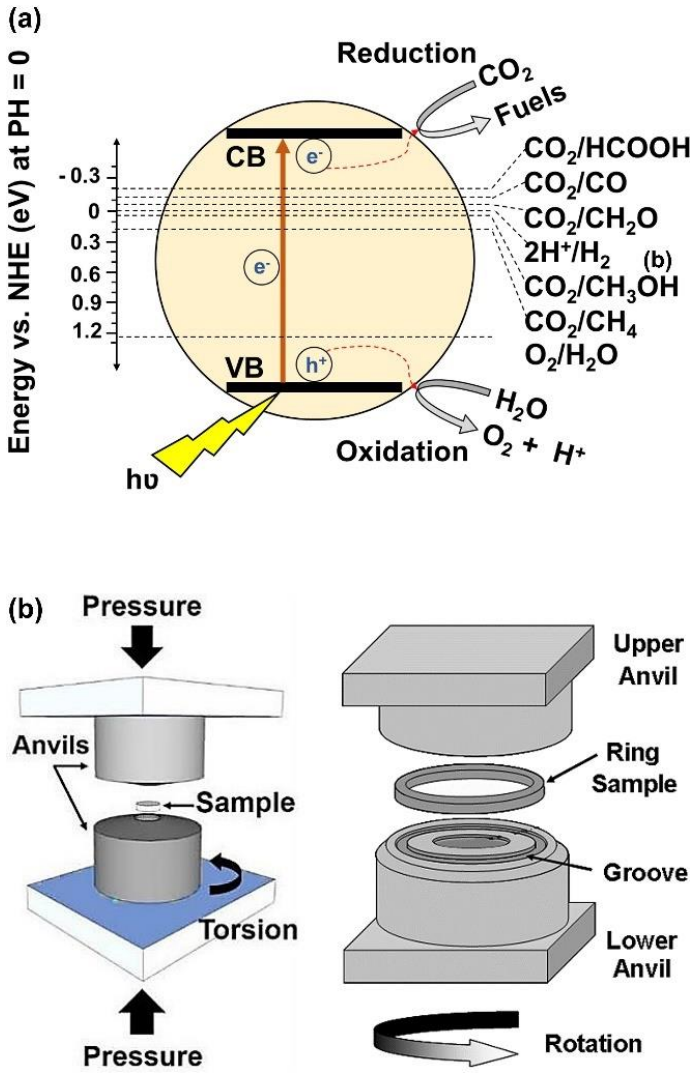


Fig. 1.1. Schematic illustration of (a) photocatalytic $CO_2$ conversion and (b) high-pressure torsion [41].

In this regard, severe plastic deformation (SPD) through the high-pressure torsion (HPT) method, which is schematically shown in Fig. 1.1b and mainly used for nanostructuring of metallic materials showed the potential to improve the electronic structure of semiconductors, narrow their bandgap and enhance the photocatalytic activity for water splitting [23-30] and dye degradation [31-34]. Fig. 1.2 shows the impact of HPT on photocatalytic $H_2$ evolution and dye degradation. In Fig. 1.2a it is observed that after HPT processing, the $H_2$ generation amount for $ZrO_2$ increased significantly [26]. Fig. 1.2b demonstrates the HPT method improved the photocatalytic activity of

$Al_2O_3$ effectively while the initial powder of this material could not degrade the dye [32]. It can be observed that the photocatalytic activity of $Al_2O_3$ after HPT is considerable compared to $TiO_2$ as a conventional semiconductor for this application [32]. Despite the application of HPT for these two photocatalytic processes, there are not any reports in the literature on the potential of this method to improve or synthesize the materials for photocatalytic $CO_2$ conversion.

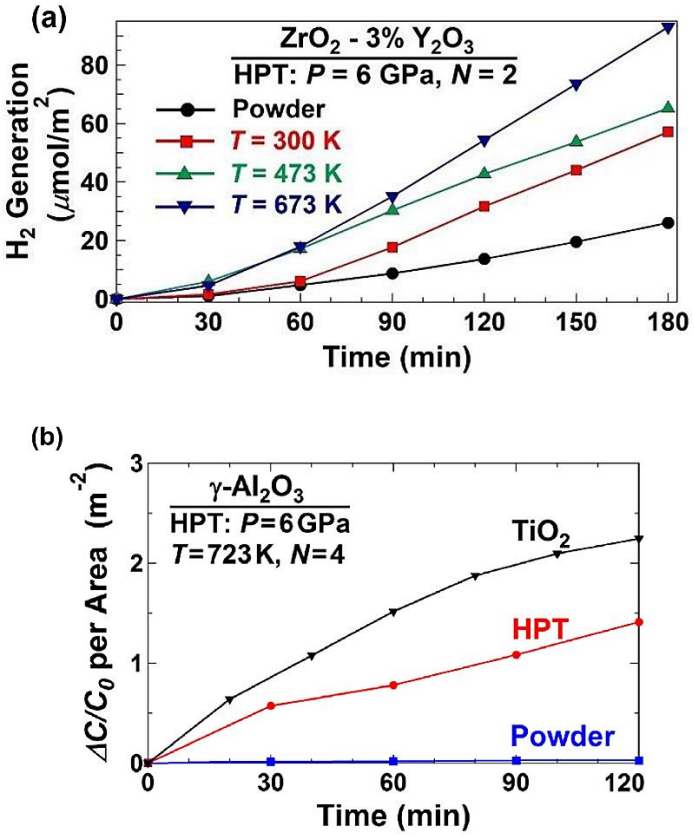


Fig. 1.2. Impact of HPT on photocatalytic $H_2$ evolution and dye degradation. (a) Photocatalytic $H_2$ production amount versus irradiation time for $ZrO_2$ and (b) photocatalytic dye degradation amount versus irradiation time for $Al_2O_3$ before and after HPT processing compared with $TiO_2$ [26,32].

### 1.2. High-pressure torsion (HPT)

The SPD process is usually used to form ultrafine-grained and nanostructured materials with enhanced mechanical and functional properties [35-37]. SPD has various methods including the HPT method, introduced by Bridgman in 1935 for the first time [35]. In this method, torsional strain under high pressure is applied to induce large plastic strain in various ranges of materials [37]. In the HPT process, a disc-shape sample that has typically a 10 mm diameter or a ring sample

is inserted between two anvils under high pressure and strained by rotation of anvils against each other [38,39]. A schematic illustration of HPT is shown in Fig. 1.1b. The applied shear strain ($\gamma$) to the sample can be calculated by the following equation [40].

$$\gamma = \frac{2\pi r N}{h} \tag{1.1}$$

where $r$, $N$ and $h$ are the distance from the center of the disc or ring, the number of turns and the sample height, respectively.

In addition to grain refinement, the HPT is widely used for hardening of pure metals [41,42], mechanical alloying of miscible and immiscible systems [43,44] and plastic deformation of hard-to-deform materials [45-47]. Phase transformation, consolidation of powders, the introduction of defects such as oxygen vacancies and dislocations, narrowing of the bandgap and improvement of functionalities were frequently reported after HPT processing [48]. The HPT method also can be utilized for the plastic deformation of ceramics which are hard and brittle materials at ambient temperature [35]. The presence of covalent or ionic bonding in ceramics results in their lower grain size after HPT processing compared to metals [35]. Moreover, such bonding features result in the formation of large densities of defects such as vacancies and dislocations which can improve the properties and functionality of ceramics [35].

Despite the high potential of ceramics for various applications, there are some limited publications on the effect of HPT on the structure, properties and functionality of ceramics. These HPT-processed ceramics, including oxides, nitrides, oxynitride and borides, have been investigated for photocatalysis [23-34], phase transformation [49-55], electrocatalysis [56], photocurrent generation [57,58], dielectric properties [59,60], bandgap narrowing [61], optical properties [62-65], mechanical properties [66,67], Li-ion batteries [68] and microstructural features [69-71]. Furthermore, the HPT method was also utilized to synthesize new ceramics for various applications [27,29]. A list of ceramics treated by HPT for various properties and applications is given in Table 1.1.

Table. 1.1. Summary of major publications about ceramics treated by HPT and their major applications or features.

| Materials | Investigated properties and application | Reference |
|---|---|---|
| | **Photocatalysis** | |
| $TiO_2$-II | Photocatalytic activity for hydrogen production | [23] |
| ZnO | Photocatalytic activity for dye degradation | [31] |
| γ-$Al_2O_3$ | Photocatalytic activity for dye degradation | [32] |
| MgO | Photocatalytic activity for dye degradation | [33] |
| $ZrO_2$ | Photocatalytic activity for hydrogen production | [26] |
| $SiO_2$ | Photocatalytic activity for dye degradation | [34] |
| $CsTaO_3$, $LiTaO_3$ | Photocatalytic activity for hydrogen production | [24] |
| GaN-ZnO | Photocatalytic activity for hydrogen production | [25] |
| $TiHfZrNbTaO_{11}$ | Photocatalytic activity for hydrogen production | [27] |
| $TiZrNbTaWO_{12}$ | Photocatalytic activity for oxygen production | [30] |
| $TiZrHfNbTaO_6N_3$ | Photocatalytic activity for hydrogen production | [29] |
| $TiO_2$-ZnO | Photocatalytic activity for hydrogen production | [28] |
| | **Reviews** | |
| | Review on HPT | [40] |
| Oxides | Review on HPT of oxides | [48] |
| | **Phase transformation** | |
| $SiO_2$, $VO_2$ | Phase transformation | [49] |
| $TiO_2$ | Grain coarsening and phase transformation | [50] |
| $ZrO_2$ | Phase transformation by ball milling and HPT | [57] |
| $ZrO_2$ | Allotropic phase transformations | [52] |
| $TiO_2$ | Plastic strain and phase transformation | [53] |
| BN | FEM modeling of plastic flow and strain-induced phase transformation | [54] |
| BN | Coupled elastoplasticity and plastic strain-induced phase transformation | [55] |
| | **Electrocatalysis** | |
| $TiO_2$-II | Electrocatalysis for hydrogen generation | [56] |
| | **Photocurrent** | |
| $Bi_2O_3$ | Enhanced photocurrent generation | [57] |
| $TiO_2$-II | Visible light photocurrent generation | [58] |
| | **Dielectric properties** | |
| $BaTiO_3$ | Optical and dielectric properties | [59] |

| | | |
|---|---|---|
| CuO | Dielectric properties | [60] |
| **Bandgap investigation** | | |
| ZnO | Bandgap narrowing | [61] |
| **Optical properties** | | |
| $Y_2O_3$ | Optical properties | [62] |
| CuO, $Y_3Fe_5O_{12}$, $FeBO_3$ | Optical properties and electronic structure | [63] |
| $Cu_2O$, CuO | Middle infrared absorption and X-ray absorption | [64] |
| CuO, $Y_3Fe_5O_{12}$, $FeBO_3$ | Optical properties | [65] |
| **Mechanical properties** | | |
| $\alpha$-$Al_2O_3$ | Microstructure and mechanical properties | [66] |
| $Fe_{53.3}Ni_{26.5}B_{20.2}$, $Co_{28.2}Fe_{38.9}Cr_{15.4}Si_{0.3}B_{17.2}$ | Microstructure and mechanical properties | [67] |
| **Lithium-ion batteries** | | |
| $Fe_3O_4$ | Lithium-ion batteries | [68] |
| **Microstructural features** | | |
| ZnO | Plastic flow and microstructural instabilities | [69] |
| $YBa_2Cu_3O_y$ | Microstructural investigation | [70] |
| $Fe_{71.2}Cr_{22.7}Mn_{1.3}N_{4.8}$ | Microstructural features | [71] |

### 1.3. Fundamentals and mechanism of photocatalytic $CO_2$ conversion

In photocatalysis, which is also called artificial photosynthesis, electrons in the valence band absorb the light photons, separate from the holes and transfer to the conduction band of the photocatalyst to form the electron-hole charge carriers. The charge carriers then migrate to the surface of the photocatalyst and finally take part in various chemical reactions [3]. In this process, both reduction and oxidation reactions occur on the surface of the photocatalyst, provided that the thermodynamic and kinetic conditions are satisfied [3]. From the thermodynamic point of view, a photocatalytic process will perform when the reduction and oxidation reaction potentials are between the valence band and the conduction band of a photocatalyst [3]. For the reduction reactions, potentials lower than the valence band top are desirable, while for the oxidation reactions, potentials higher than the conduction band bottom are desirable. From the kinetic point of view, the electron-hole separation time should be fast, and their recombination time should be slow. Here, the fundamentals of three main photocatalytic reactions are mentioned.

In photocatalytic $CO_2$ conversion, electrons in the conduction band along with protons ($H^+$) produced from water oxidation in the valence band, take part in various reduction reactions leading

to the formation of CO, $CH_4$ and some other hydrocarbons as shown in Fig. 1.1a. The first step in the photocatalytic $CO_2$ conversion process is the adsorption of $CO_2$ molecule on the surface of the photocatalyst which occurs in three modes including oxygen coordination, carbon coordination and mixed coordination [72,73], as shown in Fig. 1.3. These $CO_2$ adsorption modes determine the reaction pathway for photocatalytic $CO_2$ conversion. For instance, the oxygen coordination mode, with the bidentate bonding of oxygen atoms with the surface of the photocatalyst, leads to the fabrication of formate anion as an intermediate product and formic acid as the final product [73]. If the $CO_2$ molecules have the carbon coordination mode, with the monodentate binding of carbon and photocatalyst surface, the reaction results in carboxyl radical production [73]. After the adsorption step of $CO_2$ to the surface of the photocatalyst, the conversion reactions occur via different pathways.

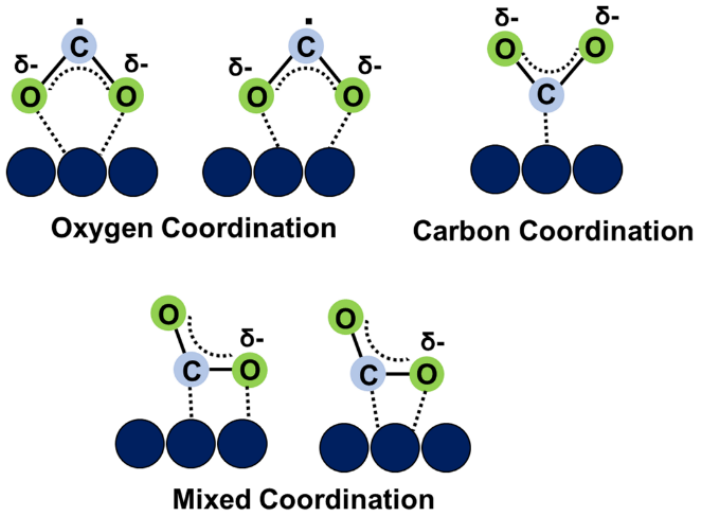


Fig. 1.3. $CO_2$ adsorption modes on the surface of photocatalyst.

It was reported that there are three main conventional pathways for $CO_2$ photoreduction: (i) carbene pathway (ii) formaldehyde pathway and (iii) glyoxal pathway [74,16]. The reactions for these three pathways are presented in Table 1.2. In all these pathways, the $CO_2^{\bullet-}$ radical is the main intermediate product which is formed by the reaction of adsorbed $CO_2$ and an electron. In the carbene pathway, $CO_2^{\bullet-}$ converts to $CO^{\bullet}$ and leads to the production of CO, $CH_2$, $CH_4$ and $CH_3OH$. In this pathway, carbon coordination is the main binding mode. In the formaldehyde pathway, $CO_2^{\bullet-}$ converts to $^{\bullet}COOH$ to produce HCOOH, $CH_3$ OH and $CH_4$ [74,75]. In this pathway,

$CO_2^{\bullet-}$ attaches to the catalyst by monodentate or bidentate binding. In monodentate binding, either one oxygen in $CO_2^{\bullet-}$ or one carbon atom in $CO_2^{\bullet-}$ are bonded to the surface of the photocatalyst. In the bidentate mode, both oxygen atoms in $CO_2^{\bullet-}$ are bonded to the photocatalyst surface [74]. In the glyoxal pathway, $C_2$ components are formed by some complicated reactions, although there are limitations to producing $C_2$ due to the low selectivity of the photocatalyst. In this pathway, $CO_2^{\bullet-}$ converts to the formyl radical $HOC^{\bullet}$ to form $C_2H_2O_2$, $C_2H_4O_2$, $C_2H_4O$, CO and $CH_4$ [74,16]. In all these pathways, $CO_2$ adsorption and activation are key parameters to adjust the selectivity of photocatalysts and this should be empowered by some strategies such as oxygen vacancy generation and strain engineering [73].

Table 1.2. Reactions of $CO_2$ photoreduction pathways [74].

| **Carbene Pathway** | **Formaldehyde Pathway** | **Glyoxal Pathway** |
|---|---|---|
| (1) $CO_2 + e^- \rightarrow CO_2^{\bullet-}$ | (1) $CO_2 + e^- \rightarrow CO_2^{\bullet-}$ | (1) $CO_2 + e^- \rightarrow CO_2^{\bullet-}$ |
| (2) $CO_2^{\bullet-} + e^- + H^+ \rightarrow CO + OH^-$ | (2) $CO_2^{\bullet-} + H^+ \rightarrow {}^{\bullet}COOH$ | (2) $CO_2^{\bullet-} + e^- + H^+ \rightarrow CHOO^-$ |
| (3) $CO + e^- \rightarrow CO^{\bullet-}$ | (3) ${}^{\bullet}COOH + e^- + H^+ \rightarrow HCOOH$ | (3) $CHOO^- + H^+ \rightarrow HCOOH$ |
| (4) $CO^{\bullet-} + e^- + H^+ \rightarrow C + OH^-$ | (4) $HCOOH + e^- + H^+ \rightarrow H_3OOC^{\bullet}$ | (4) $HCOOH + e^- \rightarrow HOC^{\bullet}$ |
| (5) $C + e^- + H^+ \rightarrow CH^{\bullet}$ | (5) $HCOOH_2^{\bullet} + e^- + H^+ \rightarrow HCOH + H_2O$ | (5) $HOC^{\bullet} + OH^- \rightarrow C_2H_2O_2$ |
| (6) $CH^{\bullet} + e^- + H^+ \rightarrow CH_2$ | (6) $HCOH + e^- \rightarrow H_2C^{\bullet}O^-$ | (6) $C_2H_2O_2 + e^- + H^+ \rightarrow H_3O_2C_2^{\bullet}$ |
| (7) $CH_2 + e^- + H^+ \rightarrow CH_3^{\bullet}$ | (7) $H_2C^{\bullet}O^- + H^+ \rightarrow H_2OHC^{\bullet}$ | (7) $H_3O_2C_2^{\bullet} + e^- + H^+ \rightarrow C_2H_4O_2$ |
| (8) $CH_3^{\bullet} + e^- + H^+ \rightarrow CH_4$ | (8) $H_2OHC^{\bullet} + e^- + H^+ \rightarrow CH_3OH$ | (8) $C_2H_4O_2 + e^- + H^+ \rightarrow H_3OC_2^{\bullet} + H_2O$ |
| (9) $CH_3^{\bullet} + OH^- \rightarrow CH_3OH$ | (9) $CH_3OH + e^- + H^+ \rightarrow {}^{\bullet}CH_3 + H_2O$ | (9) $H_3OC_2^{\bullet} + e^- + H^+ \rightarrow C_2H_4O$ |
| | (10) ${}^{\bullet}CH_3 + e^- + H^+ \rightarrow CH_4$ | (10) $C_2H_4O + h^+ \rightarrow H_3OC_2^{\bullet} + H^+$ |
| | | (11) $H_3OC_2^{\bullet} \rightarrow CH_3^{\bullet} + CO$ |
| | | (12) $CH_3^{\bullet} + e^- + H^+ \rightarrow CH_4$ |

## 1.4. Objectives and outline of thesis

Numerous studies in recent years reported that the HPT method can be used to improve the photocatalytic activity of ceramics for dye degradation and water splitting [23-34]. Bandgap narrowing for the easier transition of photoexcited electrons from the valence band to the conduction band, increasing the light absorbance in the visible region of light, electronic band structure alignment, decreasing the recombination rate of electrons and holes and accelerating the electron-hole separation and migration are some phenomena responsible for the high activity of photocatalysts processed or synthesized by HPT [23-34]. Since there are significant efforts

worldwide to reduce the $CO_2$ emissions by its conversion, in the present thesis, the HPT method is utilized for the first time to develop active photocatalysts for $CO_2$ conversion by using four main strategies.

1) Simultaneous strain and oxygen vacancy engineering
2) Introduction of high-pressure phases
3) Formation of defective high-entropy phases
4) Production of low-bandgap high-entropy oxynitride phases

This thesis contains six chapters:

In chapter 1, the research background of this thesis is summarized. A brief description of the HPT method and mechanism of photocatalytic $CO_2$ conversion is presented.

In chapter 2, $BiVO_2$ as a conventional photocatalyst is treated by HPT using simultaneous strain and oxygen vacancy engineering. Impact of HPT on oxygen vacancy concentration and lattice strain is evaluated by various characterization methods. Electronic structure, charge carrier dynamics and photocatalytic $CO_2$ conversion are investigated to realize the influence of employed strain and oxygen vacancy engineering on catalytic efficiency.

In chapter 3, the high-pressure $TiO_2$-II phase is synthesized by HPT to investigate its potential for photocatalytic $CO_2$ conversion for the first time. Impact of this new phase on light absorbance, narrowing the bandgap, charge carrier dynamics and photocatalytic activity of $TiO_2$ for $CO_2$ conversion is evaluated.

In chapter 4, a new high-entropy oxide is produced using the HPT method and subsequent high-temperature oxidation and evaluated for photocatalytic $CO_2$ conversion for the first time. This oxide is characterized by various technique in terms of crystal structure, microstructure, light absorbance, electronic structure, charge carrier dynamic and photocatalytic activity for $CO_2$ conversion.

In chapter 5, to decrease the bandgap and improve the photocatalytic activity of fabricated high-entropy oxide in previous chapter, a high-entropy oxynitride is synthesized and evaluated by various characterization methods for photocatalytic properties and activity for $CO_2$ conversion.

In chapter 6, the conclusions and outlook of this thesis are summarized.

## References


[1] M. Forkel, N. Carvalhais, C. Rodenbeck, R. Keeling, M. Heimann, K. Thonicke, S. Zaehle and M. Reichstein: Enhanced seasonal $CO_2$ exchange caused by amplified plant productivity in northern ecosystems, Science 351 (2016) 696–699.

[2] A.J. Morris, G.J. Meyer and E. Fujita: Molecular approaches to the photocatalytic reduction of carbon dioxide for solar fuels, Acc. Chem. Res. 42 (2009) 1983–1994.

[3] H. Tong, S. Ouyang, Y. Bi, N. Umezawa, M. Oshikiri and J. Ye: Nano-photocatalytic materials: possibilities and challenges, Adv. Mater. 24 (2012) 229–251.

[4] X. Li, J. Yu and C. Jiang: Chapter 1 - Principle and surface science of photocatalysis, Interface Sci. Technol. 31 (2020) 1–38.

[5] O. Ola and M.M. Maroto-Valer: Synthesis, characterization and visible light photocatalytic activity of metal based $TiO_2$ monoliths for $CO_2$ reduction, Chem. Eng. J. 283 (2016) 1244–1253.

[6] S. Neatu, J.A. Macia-Agullo, P. Concepcion and H. Garcia: Gold-copper nanoalloys supported on $TiO_2$ as photocatalysts for $CO_2$ reduction by water, J. Am. Chem. Soc. 136 (2014) 15969–15976.

[7] K. Kocí, K. Mateju, L. Obalova, S. Krejcikova, Z. Lacny, D. Placha, L. Capek, A. Hospodkova and O. Solcova: Effect of silver doping on the $TiO_2$ for photocatalytic reduction of $CO_2$, Appl. Catal. B 96 (2010) 239–244.

[8] A. Akhundi, A. Habibi-Yangjeh, M. Abitorabi and S.R. Pouran: Review on photocatalytic conversion of carbon dioxide to value-added compounds and renewable fuels by graphitic carbon nitride-based photocatalysts, Catal. Rev. Sci. Eng. 61 (2019) 595–628.

[9] P. Xia, M. Antonietti, B. Zhu, T. Heil, J. Yu and S. Cao: Designing defective crystalline carbon nitride to enable selective $CO_2$ photoreduction in the gas phase, Adv. Funct. Mater. 29 (2019) 1900093.

[10] K. Wang, L. Zhang, Y. Su, S. Sun, Q. Wang, H. Wang and W. Wang: Boosted $CO_2$ photoreduction to methane via Co doping in bismuth vanadate atomic layers, Catal, Sci. Technol. 8 (2018) 3115–3122.

[11] L. Huang, Z. Duan, Y. Song, Q. Li and L. Chen: $BiVO_4$ microplates with oxygen vacancies decorated with metallic Cu and Bi nanoparticles for $CO_2$ photoreduction, ACS Appl. Nano Mater. 4 (2021) 3576–3585.

[12] Z. Zhu, C.X. Yang, Y.T. Hwang, Y.C. Lin and R.J. Wu: Fuel generation through photoreduction of $CO_2$ on novel Cu/$BiVO_4$, Mater. Res. Bull. 130 (2020) 110955.

[13] G.J. Lee, S. Anandan, S.J. Masten and J.J. Wu: Photocatalytic hydrogen evolution fromwater splitting using Cu doped ZnS microspheres under visible light irradiation, Renew. Energy 89 (2016) 18–26.

[14] B. Liu, L. Ye, R. Wang, J. Yang, Y. Zhang, R. Guan, L. Tian and X. Chen: Phosphorus-doped graphitic carbon nitride nanotubes with amino-rich surface for efficient $CO_2$ capture, enhanced photocatalytic activity, and product selectivity, ACS Appl. Mater. Interfaces 10 (2018) 4001–4009.

[15] A.T. Kuvarega, R.W.M. Krause and B.B. Mamba: Nitrogen/palladium-codoped $TiO_2$ for efficient visible light photocatalytic dye degradation, J. Phys. Chem. C 115 (2011) 22110–22120.

[16] K. Wang, J. Lu, Y. Lu, C.H. Lau, Y. Zheng and X. Fan: Unravelling the C-C coupling in $CO_2$ photocatalytic reduction with $H_2O$ on Au/$TiO_{2-x}$: combination of plasmonic excitation and oxygen vacancy, Appl. Catal. B 292 (2021) 120147.

[17] J. Di, C. Zhu, M. Ji, M. Duan, R. Long, C. Yan, K. Gu, J. Xiong, Y. She, J. Xia, H. Li and Z. Liu: Defect-rich $Bi_{12}O_{17}Cl_2$ nanotubes self-accelerating charge separation for boosting photocatalytic $CO_2$ reduction, Angew. Chem. 57 (2018) 14847–14851.

[18] X. Cai, F. Wang, R. Wang, Y. Xi, A.n. Wang, J. Wang, B. Teng and S. Bai: Synergism of surface strain and interfacial polarization on Pd@Au core-shell cocatalysts for highly efficient photocatalytic $CO_2$ reduction over $TiO_2$, J. Mater. Chem. A 8 (2020) 7350–7359.

[19] Z. Liu, C. Menendez, J. Shenoy, J.N. Hart, C.C. Sorrell and C. Cazorl: Strain engineering of oxide thin films for photocatalytic applications, Nano Energy 72 (2020) 104732.

[20] Y. Li, W.N. Wang, Z. Zhan, M.H. Woo, C.Y. Wu and P. Biswas: Photocatalytic reduction of $CO_2$ with $H_2O$ on mesoporous silica supported Cu/$TiO_2$ catalysts, Appl. Catal. B 100 (2010) 386–392.

[21] S. Cao, B. Shen, T. Tong, J. Fu and J. Yu: 2D/2D heterojunction of ultrathin MXene/ $Bi_2WO_6$ nanosheets for improved photocatalytic $CO_2$ reduction, Adv. Funct. Mater. 28 (2018) 1800136.

[22] J. Li, W. Shao, M. Geng, S. Wan, M. Ou and Y. Chen: Combined Schottky junction and doping effect in $Cd_xZn_{1-x}S$@Au/$BiVO_4$ Z-Scheme photocatalyst with boosted carriers charge separation for $CO_2$ reduction by $H_2O$, J. Colloid Interface Sci. 606 (2022) 1469–1476.

[23] H. Razavi-Khosroshahi, K. Edalati, M. Hirayama, H. Emami, M. Arita, M. Yamauchi, H. Hagiwara, S. Ida, T. Ishihara, E. Akiba, Z. Horita and M. Fuji: Visible- light-driven photocatalytic hydrogen generation on nanosized $TiO_2$-II stabilized by high-pressure torsion, ACS Catal. 6 (2016) 5103–5107.

[24] K. Edalati, K. Fujiwara, S. Takechi, Q. Wang, M. Arita, M. Watanabe, X. Sauvage, T. Ishihara and Z. Horita: Improved photocatalytic hydrogen evolution on tantalate perovskites $CsTaO_3$ and $LiTaO_3$ by strain-induced vacancies, ACS Appl. Energy Mater. 3 (2020) 1710–1718.

[25] K. Edalati, R. Uehiro, S. Takechi, Q. Wang, M. Arita, M. Watanabe, T. Ishihara and Z. Horita: Enhanced photocatalytic hydrogen production on GaN-ZnO oxynitride by introduction of strain-induced nitrogen vacancy complexes, Acta Mater. 185 (2020) 149–156.

[26] Q. Wang, K. Edalati, Y. Koganemaru, S. Nakamura, M. Watanabe, T. Ishihara and Z. Horita: Photocatalytic hydrogen generation on low-bandgap black zirconia ($ZrO_2$) produced by high-pressure torsion, J. Mater. Chem. A 8 (2020) 3643–3650.

[27] P. Edalati, Q. Wang, H. Razavi-Khosroshahi, M. Fuji, T. Ishihara and K. Edalati: Photocatalytic hydrogen evolution on a high entropy oxide, J. Mater. Chem. A 8 (2020) 3814–3821.

[28] J. Hidalgo-Jimeneza, Q. Wang, K. Edalatib, J.M. Cubero-Sesína, H. Razavi-Khosroshahid, Y. Ikomac, D. Gutiérrez-Fallase, Fernando A. Dittel-Mezaa, J.C. Rodríguez-Rufinoa, M. Fujid and Z. Horita: Phase transformations, vacancy formation and variations of optical and photocatalytic properties in $TiO_2$-ZnO composites by high pressure torsion, Int. J. Plast. 124 (2020) 170–185.

[29] P. Edalati, X.F. Shen, M. Watanabe, T. Ishihara, M. Arita, M. Fuji and K. Edalati: High-entropy oxynitride as a low-bandgap and stable photocatalyst for hydrogen production, J. Mater. Chem. A 9 (2021) 15076–15086.

[30] P. Edalati, Y. Itagoe, H. Ishihara, T. Ishihara, H. Emami, M. Arita, M. Fuji and K. Edalati: Visible-light photocatalytic oxygen production on a high-entropy oxide by multiple-heterojunction introduction, J. Photochem. Photobiol. A 433 (2022) 114167.

[31] H. Razavi-Khosroshahi, K. Edalati, J. Wu, Y. Nakashima, M. Arita, Y. Ikoma, M. Sadakiyo, Y. Inagaki, A. Staykov, M. Yamauchi, Z. Horita and M. Fuji: High-pressure zinc oxide phase as visible-light-active photocatalyst with narrow band gap, J. Mater. Chem. A, 5 (2017) 20298–20303.

[32] K. Edalati, I. Fujita, S. Takechi, Y. Nakashima, K. Kumano, H. Razavi-Khosroshahi, M. Arita, M. Watanabe, X. Sauvage, T. Akbay, T. Ishihara, M. Fuji and Z. Horita: Photocatalytic activity of aluminum oxide by oxygen vacancy generation using high-pressure torsion straining, Scr. Mater. 173 (2019) 120–124.

[33] I. Fujita, K. Edalati, Q. Wang, M. Arita, M. Watanabe, S. Munetoh, T. Ishihara, Z. Horita, High-pressure torsion to induce oxygen vacancies in nanocrystals of magnesium oxide: Enhanced light absorbance, photocatalysis and significance in geology, Materialia 11 (2020) 100670.

[34] Q. Wang, K. Edalati, I. Fujita, M. Watanabe, T. Ishihara and Z. Horita: High-pressure torsion of $SiO_2$ quartz sand: Phase transformation, optical properties, and significance in geology, J. Am. Ceram. Soc. 103 (2020) 6594–6602.

[35] K. Edalati, A. Bachmaier, V.A. Beloshenko, Y. Beygelzimer, V.D. Blank, W.J. Botta, K. Bryła, J. Čížek, S. Divinski, N.A. Enikeev, Y. Estrin, G. Faraji, R.B. Figueiredo, M. Fuji, T. Furuta, T. Grosdidier, J. Gubicza, A. Hohenwarter, Z. Horita, J. Huot, Y. Ikoma, M. Janeček, M. Kawasaki, P. Krăl, S. Kuramoto, T.G. Langdon, D.R. Leiva, V.I. Levitas, A. Mazilkin, M. Mito, H. Miyamoto, T. Nishizaki, R. Pippan, V.V. Popov, E.N. Popova, G. Purcek, O. Renk, Á. Révész, X. Sauvage, V. Sklenicka, W. Skrotzki, B.B. Straumal, S. Suwas, L.S. Toth, N. Tsuji, R.Z. Valiev, G. Wilde, M.J. Zehetbauer, X. Zhu, Nanomaterials by severe plastic deformation: review of historical developments and recent advances, Mater. Res. Lett. 10 (2022) 163-256.

[36] R. Valiev, Nanostructuring of metals by severe plastic deformation for advanced properties, Nat. Mater. 3 (2004) 511-516.

[37] Y. Estrin, A.Vinogradov, Extreme grain refinement by severe plastic deformation: A wealth of challenging science, Act. Mater. 61 (2013) 782-817.

[38] PW. Bridgman, Effects of high shearing stress combined with high hydrostatic pressure. Phys Rev. 48 (1935) 825-847.

[39] K. Edalati, Z. Horita, Scaling-up of high pressure torsion using ring shape, Mater. Trans. 50 (2009) 92-95.

[40] K. Edalati, Z. Horita, A review on high-pressure torsion (HPT) from 1935 to 1988, Mater. Sci. Eng. A 652 (2016) 325-352.

[41] M.J. Starink, X. Cheng, S. Yang, Hardening of pure metals by high-pressure torsion: A physically based model employing volume-averaged defect evolutions, Act. Mater. 61 (2013) 183-192.

[42] K. Edalati, Z. Horita, High-pressure torsion of pure metals: Influence of atomic bond parameters and stacking fault energy on grain size and correlation with hardness, Act. Mater. 59 (2011) 6831-6836.

[43] K. Edalati, Metallurgical alchemy by ultra-severe plastic deformation via high-pressure torsion process, Mater. Trans. 60 (2019) 1221-1229.

[44] K. Edalati, H. Emami, A. Staykov, D.J. Smith, E. Akiba, Z. Horita, Formation of metastable phases in magnesium-titanium system by high-pressure torsion and their hydrogen storage performance, Acta Mater. 99 (2015) 150-156.

[45] K. Edalati, Z. Horita, Y. Mine, High-pressure torsion of hafnium, Mater. Sci. Eng. A 527 (2010) 2136-2141.

[46] K. Edalati, Y. Yokoyama, Z. Horita, High-pressure torsion of machining chips and bulk discs of amorphous Zr50Cu30Al10Ni10, Mater. Trans. 51 (2010) 23-26.

[47] Y. Ikoma, K. Hayano, K. Edalati, K. Saito, Q. Guo, Z. Horita, Phase transformation and nanograin refinement of silicon by processing through high-pressure torsion, Appl. Phys. Lett. 101 (2012) 121908.

[48] K. Edalati, Review on recent advancements in severe plastic deformation of oxides by high-pressure torsion (HPT), Adv. Eng. Mater. 21 (2019) 1800272.

[49] K. Edalati, I. Fujita, X. Sauvage, M. Arita, Z. Horita, Microstructure and phase transformations of silica glass and vanadium oxide by severe plastic deformation via high-pressure torsion straining, J. Alloys Compd. 779 (2019) 394-398.

[50] K. Edalati, Q. Wang, H. Razavi-Khosroshahi, H. Emami, M. Fuji, Z. Horita, Low-temperature anatase-to-rutile phase transformation and unusual grain coarsening in titanium oxide nanopowders by high-pressure torsion straining, Scr. Mater. 162 (2019) 341-344.

[51] F. Delogu, Are processing conditions similar in ball milling and high-pressure torsion? The case of the tetragonal-to-monoclinic phase transition in $ZrO_2$ powders, Scr. Mater. 67 (2012) 340-343.

[52] K. Edalati, S. Toh, Y. Ikomaa, Z. Horita, Plastic deformation and allotropic phase transformations in zirconia ceramics during high-pressure torsion, Scr. Mater. 65 (2011) 974-977.

[53] H. Razavi-Khosroshahi, K. Edalati, M. Arita, Z. Horita, M. Fuji, Plastic strain and grain size effect on high-pressure phase transformations in nanostructured $TiO_2$ ceramics, Scr. Mater. 124 (2016) 59-62.

[54] B. Feng, V.I. Levitas, W. Li, FEM modeling of plastic flow and strain-induced phase transformation in BN under high pressure and large shear in a rotational diamond anvil cell, Int. J. Plast. 113 (2019) 236-254.

[55] B. Feng, V.I. Levitas, coupled elastoplasticity and plastic strain-induced phase transformation under high pressure and large strains: Formulation and application to BN sample compressed in a diamond anvil cell, Int. J. Plast. 96 (2017) 156-181.

[56] K. Edalati, Q. Wang, H. Eguchi, H. Razavi-Khosroshahi, H. Emami, M. Yamauchi, M. Fuji, Z. Horita, Impact of $TiO_2$-II phase stabilized in anatase matrix by high-pressure torsion on electrocatalytic hydrogen production, Mater. Res. Lett. 7 (2019) 334-339.

[57] I. Fujita, P. Edalati, Q. Wang, M. Watanabe, M. Arita, S. Munetoh, T. Ishihara, K. Edalati, Novel black bismuth oxide ($Bi_2O_3$) with enhanced photocurrent generation, produced by high-pressure torsion straining, Scr. Mater. 187 (2020) 366-370.

[58] Q. Wang, M. Watanabe, K. Edalati, Visible-light photocurrent in nanostructured high-pressure $TiO_2$-II (Columbite) Phase, J. Phys. Chem. C 124 (2020) 13930-13935.

[59] K. Edalati, M. Arimura, Y. Ikoma, T. Daio, M. Miyata, D.J. Smith, Z. Horita, Plastic deformation of BaTiO3 ceramics by high-pressure torsion and changes in phase transformations, optical and dielectric properties, Mater. Res. Lett. 3 (2015) 216-221.

[60] A.A. Makhnev, L.V. Nomerovannaya, B.A. Gizhevskii, S.V. Naumov, N.V. Kostromitin, Effect of redistribution of the optical spectral weight in CuO nanostructured ceramics, Solid State Phenom. 168-169 (2011) 285-288.

[61] Y. Qi, Y. Kauffmann, A. Kosinova, A.R. Kilmametov, B.B. Straumal, E. Rabkin, Gradient bandgap narrowing in severely deformed ZnO nanoparticles, Matter. Res. Lett. 9 (2021) 58-64.

[62] H. Razavi-Khosroshahi, K. Edalati, H. Emami, E. Akiba, Z. Horita, M. Fuji, Optical properties of nanocrystalline monoclinic Y2O3 stabilized by grain size and plastic strain effects via high-pressure torsion, Inorg. Chem. 56 (2017) 2576-2580.

[63] B.A. Gizhevskii, Y.P. Sukhorukov, L.V. Nomerovannaya, A.A. Makhnev, Y.S. Ponosov, A.V. Telegin, E.V. Mostovshchikov, Features of optical properties and the electronic structure of nanostructured oxides of 3d-Metals, Solid State Phenom. 168-169 (2011) 317-320.

[64] E.V. Mostovshchikova, B.A. Gizhevskii, N.N. Loshkareva, V.R. Galakhov, S.V. Naumov, Y.S. Ponosov, N.A. Ovechkina, N.V. Kostromitina, A. Buling, M. Neumann, Infrared and X-ray absorption spectra of Cu2O and CuO nanoceramics, Solid State Phenom. 190 (2012) 683-686.

[65] A.V. Telegin, B.A. Gizhevskii, L.V. Nomerovannaya, A.A. Makhnev, The optical and magneto-optical properties of nanostructured oxides of 3d-metals, J. Supercond. Nov. Magn. 25 (2012) 2683-2686.

[66] K. Edalati, Z.Horita, Application of high-pressure torsion for consolidation of ceramic Powders, Scr. Mater. 63 (2010) 174-177.

[67] I. Permyakova, A. Glezer, Amorphous-nanocrystalline composites prepared by high-pressure torsion, Metals 10 (2020) 511.

[68] C. Qian, Z. He, C. Liang, W. Ji, New in situ synthesis method for $Fe_3O4$/flake graphite nanosheet composite structure and its application in anode materials of lithium-ion batteries, 2018 (2018) J. Nanomater. 2417949.

[69] Y. Qi, A. Kosinova, A.R. Kilmametov, B.B. Straumal, E. Rabkin, Plastic flow and microstructural instabilities during high-pressure torsion of Cu/ZnO composites, Mater. Charact. 145 (2018) 389-401.

[70] E.I. Kuznetsova, M.V. Degtyarev, N.A. Zyuzeva, I.B. Bobylev, V.P. Pilyugin, Microstructure of YBa2Cu3Oy subjected to severe plastic deformation by high pressure torsion, Phys. Met. Metallogr. 118 (2017) 815-823.

[71] V.A. Shabashov, A.V. Makarov, K.A. Kozlov, V.V. Sagaradze, A.E. Zamatovskii, E.G. Volkova, S.N. Luchko, Deformation-induced dissolution and precipitation of nitrides in austenite and ferrite of a high-nitrogen stainless steel, Phys. Met. Metallogr. 119 (2018) 193-204.

[72] H. Lu, J. Tournet, K. Dastafkan, Y. Liu, Y.H. Ng, S.K. Karuturi, C. Zhao, Z. Yin, Noble-metal-free multicomponent nanointegration for sustainable energy conversion, Chem. Rev. 2021, 121 (2021) 10271–10366.

[73] J. Fu, K. Jiang, X. Qiu, J. Yu, M. Liu, Product selectivity of photocatalytic $CO_2$ reduction reactions, Mater. Today 32 (2020) 222-243.

[74] A.S.N. Habisreutinger, L. Schmidt-Mende, J.K. Stolarczyk, Photocatalytic reduction of $CO_2$ on $TiO_2$ and other semiconductors, Angew. Chem. Int. Ed. 52 (2013) 7372-7408.

[75] K. Maeda, K. Domen, New non-oxide photocatalysts designed for overall water splitting under visible light, J. Phys. Chem. C 111 (2007) 7851-7861.

# Chapter 2. Enhanced $CO_2$ conversion on highly-strained and oxygen-deficient $BiVO_4$ photocatalyst

## 2.1. Introduction

Among various photocatalysts developed for photocatalytic $CO_2$ conversion, $BiVO_4$ (as a mixed-metal oxide or salt) has recently received significant attention due to its high stability and low direct bandgap (2.4-2.5 eV) [1,2]. The main drawbacks of $BiVO_4$ which limit its photocatalytic $CO_2$ conversion efficiency are its low conduction band energy level and high rate of electron and hole recombination [2,3]. To improve the photocatalytic $CO_2$ conversion on $BiVO_4$, most reported studies introduced heterojunctions as a strategy: $BiVO_4/C_4N_3$ [3], $BiVO_4\{010\}/Au/Cu_2O$ [4], $BiVO_4/C/Cu_2O$ [5], $ZnIn_2S_4/BiVO_4$ [6], $BiVO_4/Bi_4Ti_3O_{12}$ [7], and $Cd_xZn_{1-x}S@Au/BiVO_4$ [8]. Doping with other elements such as Bi, Cu and Ag [9-13] and formation of vanadium-deficient layers [14] were also reported as other strategies to enhance the photocatalytic $CO_2$ reduction on $BiVO_4$. Despite the well-known importance of engineering the defects and lattice strain on photocatalytic $CO_2$ conversion, there have been limited studies on this issue for pure $BiVO_4$ without the addition of impurities.

There are some reported methods in the literature to introduce the defects and strain in photocatalysts. Thermal treatment under hydrogen or inert atmospheres at high temperature, chemical reduction, vacuum activation, ultraviolet irradiation, phase transformation via fast heating, plasma etching, lithium-induced conversion and low-valence metal doping are some methods used to introduce lattice defects such as oxygen vacancies [15-17]. Most of these methods need chemical reactions, high temperature or impurity addition. In the case of $BiVO_4$ for photocatalytic $CO_2$ conversion, doping with other elements or producing oxygen- and vanadium-deficient layers by chemical reactions are the methods utilized for oxygen vacancy generation [9-14]. There are few studies on strain engineering of $BiVO_4$-based photocatalysts, although strain engineering can be conducted by the formation of layered and core-shell structures or by chemical methods such as solvothermal technique [18,19].

In this chapter, $BiVO_4$ was treated by a high-pressure torsion (HPT) method to simultaneously introduce both defects and strain and improve the electronic structure, carrier dynamics and photocatalysis $CO_2$ conversion. The HPT method, in which a material is torsionally

strained under high pressure [20], was used in this study because the method can introduce defects and strain in oxides without a need for impurity atoms [21,22]. The highly-strained and oxygen-deficient $BiVO_4$ exhibited narrow optical bandgap, enhanced conduction band bottom, low electron-hole recombination rate and high photocatalytic $CO_2$ conversion, which was comparable to the conversion rate on P25 $TiO_2$ as a benchmark photocatalyst. This study introduces an effective strategy based on defect and strain engineering to enhance the photocatalytic $CO_2$ conversion on $BiVO_4$, although the strategy is easily applicable to a wider range of photocatalysts for $CO_2$ conversion.

## 2.2. Experimental procedure

### *2.2.1. Sample synthesis*

Initial $BiVO_4$ with 99.9% purity was purchased from Sigma Aldrich and further processed by HPT, as schematically shown in Fig. 2.1a [20]. For HPT processing, about 410 mg of initial powder was first compressed under 380 MPa to form pellets with 10 mm diameter and 0.8 mm thickness. The pellets were then compressed between two HPT anvils under a pressure of 6 GPa at room temperature (300 K). When the pressure was stabilized, the sample was plastically strained by rotating the lower anvil with respect to the upper anvil for either 0.25, 1 or 4 turns with a rotation speed of 1 rpm. It should be noted that larger plastic deformation is introduced in the sample with increasing the number of HPT turns [20]. The appearance of the initial powder and of the three samples processed by HPT after compacting to disc shapes are shown in Fig. 2.1b. The color of samples became darker with increasing the number of HPT turns and changed from yellow to orange and rose, respectively. These color changes indicate that photons with lower energies can be absorbed after HPT processing, as shown in the Itten color wheel of Fig. 2.1c [23].

### *2.2.2. Characterization*

The initial powder and the samples processed by HPT for 0.25, 1 and 4 turns were characterized by various techniques, as described below.

- Crystal structure was examined by X-ray diffraction (XRD) utilizing the Cu Kα radiation ($\lambda$ = 0.1542 nm wavelength) and a zero-diffraction amorphous silicon holder with a scanning speed of 1 °/min. A Rigaku SmartLab 9kW AMK machine equipped with automatic alignment systems for beam, detector and sample (height and angle) was used for the XRD analysis. The

precision of diffraction angle, confirmed by using a standard crystalline silicon sample, was better than 0.01°. XRD profiles were analyzed using PDXL software to determine the lattice parameters and lattice volume. Moreover, the crystallite size was determined by the Halder-Wagner method [24].

- $$\left(\frac{\beta}{\tan^2\theta}\right)^2 = \frac{K\lambda}{D}\left(\frac{\beta\cos(\theta)}{\sin^2\theta}\right) + 16\varepsilon^2 \quad (2.1)$$

where, $\beta$, $\theta$, $K$, $\lambda$, $D$ and ε are full width at half maximum after subtracting the instrumental broadening, Bragg angle, shape factor, wavelength, crystallite size and lattice distortion (caused by planar and line defects), respectively.

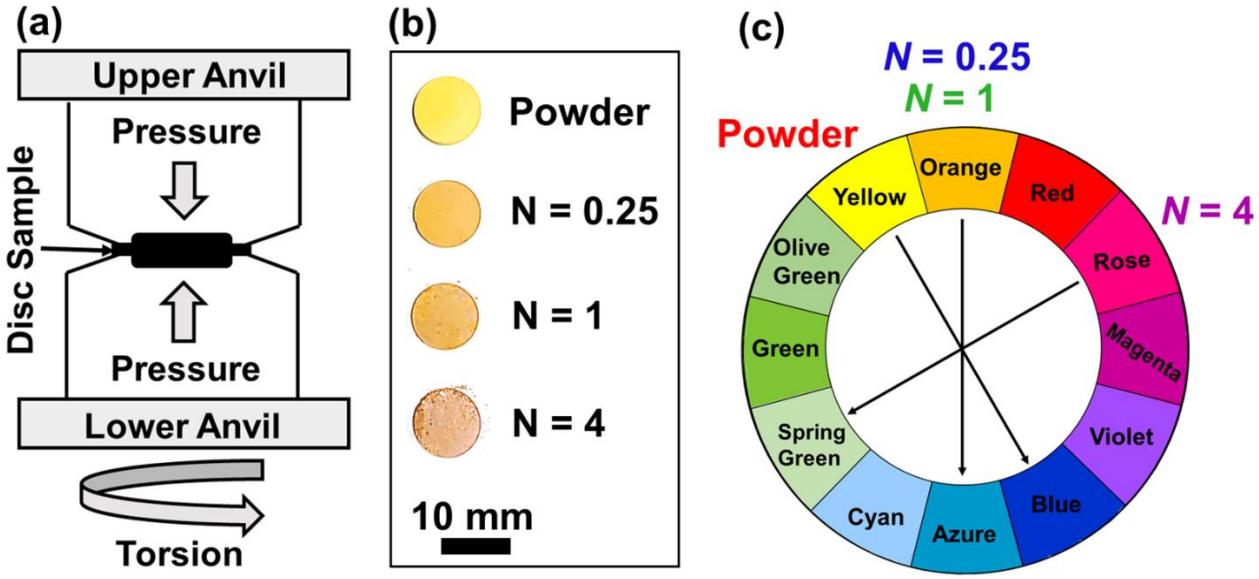


Fig. 2.1. (a) Schematics of HPT method, (b) appearance of $BiVO_4$ samples before and after HPT processing for 0.25, 1 and 4 turns, and (c) color of samples in comparison with Itten color wheel. Samples in (b) were compacted to disc form to show color changes clearly.

- Crystal structure was also examined by Raman spectroscopy using a laser source with $\lambda$ = 532 nm wavelength. A Renishaw inVia Raman WiRE 4 machine equipped with an optic alignment

tool was used. The precision of Raman shift, confirmed using a standard single-crystal silicon sample, was better than 0.1 $cm^{-1}$.

- Particle size was measured by the dynamic light scattering (DLS) method utilizing a Zetasizer Nano-S machine equipped with a 4 mW He-Ne laser (633 nm) with 173° diffraction angle. The specific surface area was measured from the average particle size as: surface area ($m^2g^{-1}$) = 6000 / [average particle size (nm) * (density ($gcm^{-3}$)].
- Microstructure was investigated by transmission electron microscopy (TEM) using the bright-field (BF) images, dark-field (DF) images, selected area electron diffraction (SAED) analysis, high-resolution images and fast Fourier transform (FFT) diffractograms. For these observations, small amounts of samples were crushed in ethanol and dispersed on a carbon grid and examined in an aberration-corrected TEM under a voltage of 200 keV.
- X-ray photoelectron spectroscopy (XPS) using the Al Kα radiation with a wavelength of λ = 0.834 nm was used to determine the oxidation state of elements and the presence of oxygen vacancies. Peak deconvolution of O 1s XPS spectrum was also performed to calculate the oxygen vacancies concentration [25].
- Electron paramagnetic resonance (EPR) using a 9.4688 GHz microwave source was used to investigate the formation of oxygen vacancies.
- Light absorbance of samples was examined by UV-vis diffuse reflectance spectroscopy and then the optical bandgap was calculated by the Kubelka-Munk analysis.
- The valence band top was determined using the ultraviolet photoelectron spectroscopy (UPS) with the He-I UV irradiation and a DC bias of -4 V. The conduction band bottom was determined by adding the bandgap to the valence band top.
- Recombination rate of electrons and holes was investigated by steady-state photoluminescence (PL) emission spectroscopy with a 325 nm laser light source.
- Time-resolved photoluminescence decay (PL decay) with a 285 nm laser source was performed to investigate the average lifetime of excited electrons.

### *2.2.3. Photocurrent test*

Photocurrent measurement was conducted under the full arc of a xenon lamp (300 W, Asashi Spectra, Japan, HAL-320W) in a 1 M $Na_2SO_4$ electrolyte to study the electron separation potential. A thin film of $BiVO_4$ samples on FTO (fluorine-doped tin oxide, 8 Ω/sq, Aldrich) glass

was used as a working electrode, and Pt wire and Ag/AgCl were utilized as the counter and reference electrodes, respectively. To measure the photocurrent generation, an electrochemical analyzer (ALS C. Ltd., Japan, BAS1230C) was used in potentiostatic amperometry mode under a voltage of 0.7 V versus Ag/AgCl (0.5 min light ON and 1 min light OFF). To prepare the thin film samples, 5 mg of $BiVO_4$ were crushed in 0.2 mL ethanol and dispersed on 2.25 mm thick FTO glass with 15×25 $mm^2$ surface area and baked in a muffle furnace at 473 K for 1 h, as described in detail in an earlier study [26].

### *2.2.4. Photocatalysis test*

For the photocatalytic $CO_2$ conversion test, 120 mg of each sample was dissolved in 500 mL of deionized water and 1 M $NaHCO_3$ under $CO_2$ bubbling with a flow rate of 3 $mLmin^{-1}$. Photocatalytic test was performed in an 858 mL cylindrical quartz photoreactor with continuous flow, as described earlier [27]. A high-pressure mercury light source with 0.5 $Wcm^{-2}$ light intensity (Sen Lights continuous flow Corporation, HL400BH-8, 400 W) with no filtering was used for irradiation. The process was first performed without irradiation for 2 h to be sure about the absence of reaction products. The light source was then placed in the inner space of the reactor and the reactor temperature was adjusted to 288 K by a water chiller. The reaction mixture was stirred continuously by a magnetic stirrer and the $CO_2$ gas was injected into the reactor by an inlet hole on the top of the reactor. The reaction products continuously flowed out of the reactor through an outlet hole on the top of the reactor, as shown in Fig. 2.1a. The outlet gas from the reactor was divided into two parts and moved either to vent or a gas chromatograph (Shimadzu GC-8A, Ar Carrier). The formation of CO and $CH_4$ was determined by a flame ionization detector equipped with a methanizer (Shimadzu MTN-1). To measure $H_2$ and $O_2$ production rate, a thermal conductivity detector was also used. Fig. 2.2a shows the system used for photocatalytic $CO_2$ conversion along with the relevant spectral composition of the mercury light source in Fig. 2.2b. It should be noted that a blank test without the catalyst addition but with light irradiation was also conducted to be sure about the absence of reaction products.

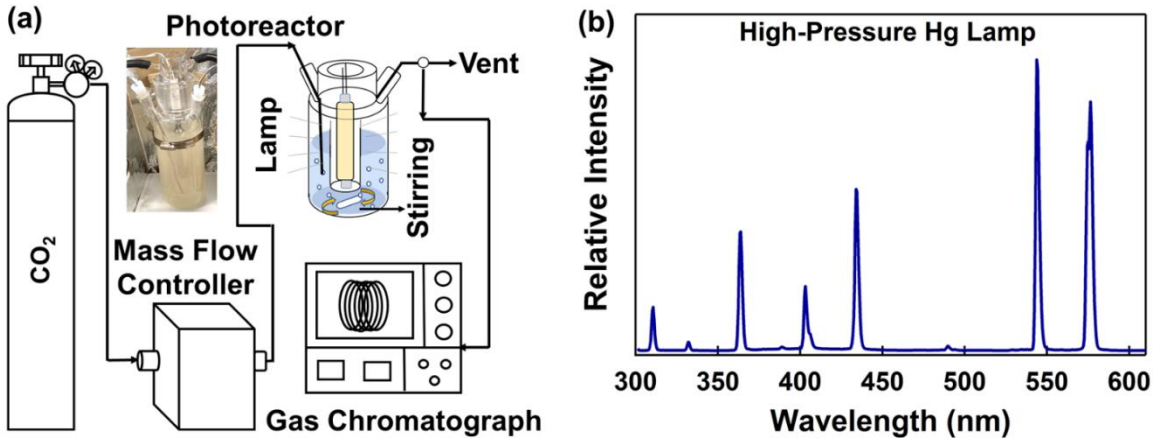


Fig. 2.2. (a) Schematics of photocatalytic experiment for $CO_2$ conversion, (b) spectral composition of light source employed for photocatalytic experiment.

## 2.3. Results

### *2.3.1. Lattice strain and microstructure*

Fig. 2.3a shows the crystal structure analysis of four samples using the XRD method. It is evident that the initial powder and the HPT-processed samples have a monoclinic phase (C12/c1 space group with $a$ = 0.519 nm, $b$ = 1.170 nm, $c$ = 0.509 nm; $\alpha$ = 90°, $\beta$ = 90.38° and $\gamma$ = 90°). XRD profiles in a higher magnification are shown in Fig. 2.3b for the (004) atomic plane with a diffraction angle of ~30.5°. There is a peak shift to higher angles after HPT processing and the shift becomes more significant with increasing the number of turns (i.e., with increasing plastic deformation). The peak shift is an indication of lattice expansion, which can be due to lattice strain and vacancy-type defect formation [28,29]. Furthermore, a peak broadening occurs, and the broadening becomes more significant with increasing the number of turns. The peak broadening is usually due to the formation of dislocation-type defects or planar imperfections such as grain boundaries [30]. Fig. 2.3c shows the crystallite size of four samples measured by the Halder-Wagner method. It is evident that the crystallite size increases from 65.7 nm for the initial powder to 24.6, 12.2 and 8.8 nm for the samples proceeded by HPT for 0.25, 1 and 4 turns, respectively. Fig. 2.3a also summarizes the volumetric lattice strain which was calculated as the increase in the lattice volume of the HPT-processed sample compared to the lattice volume of the initial powder, $\Delta V/V_0$. The estimated volumetric lattice strains for the samples proceeded by HPT for 0.25, 1 and 4 turns are 0.52%, 0.68% and 0.86%, respectively.

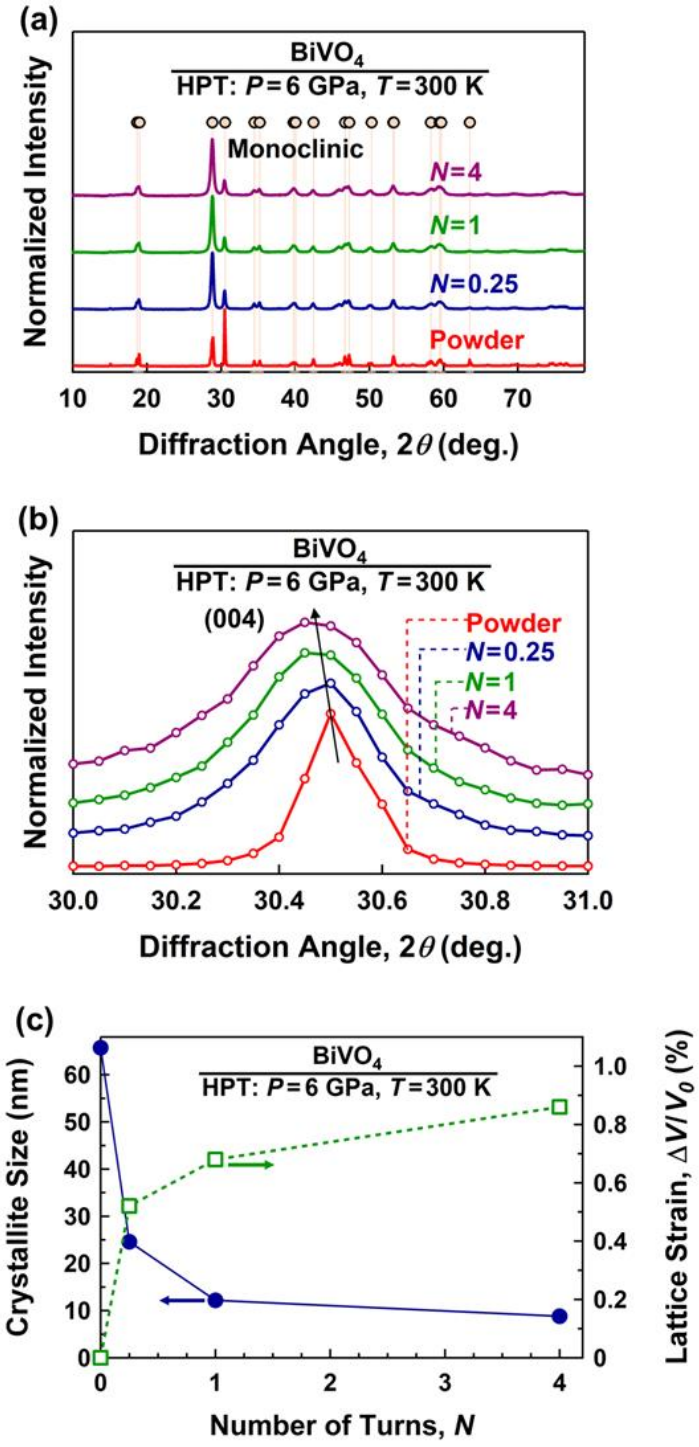


Fig. 2.3. Formation of strained nanocrystals in monoclinic phase $BiVO_4$ by HPT processing. (a) XRD analysis, (b) XRD analysis in high magnification for (004) atomic plane and (c) crystallite size and volumetric lattice strain versus number of HPT turns for powder and samples processed for 0.25, 1 and 4 turns.

Fig. 2.4a illustrates the crystal structure analysis using the Raman spectroscopy method for the four samples. All peaks in the Raman spectra correspond to the monoclinic phase in good agreement with the XRD analyses. The peaks located at 124 and 210 $cm^{-1}$ are relevant to the external mode of $BiVO_4$; the peaks located at 330 and 365 $cm^{-1}$ are relevant to asymmetric (($\delta_{as}(VO_4^{-3})$) and symmetric (($\delta_s(VO_4^{-3})$) deformation modes of the $VO_4^{3-}$, respectively; and the peak located at 827 $cm^{-1}$ is due to stretching vibration mode of the V-O bonds in the $VO_4^{-3}$ ($\upsilon_s$) [31]. Since the peak at 827 $cm^{-1}$ shows the length of V-O bonds, it is usually used to analyze the lattice strain in $BiVO_4$ [32].

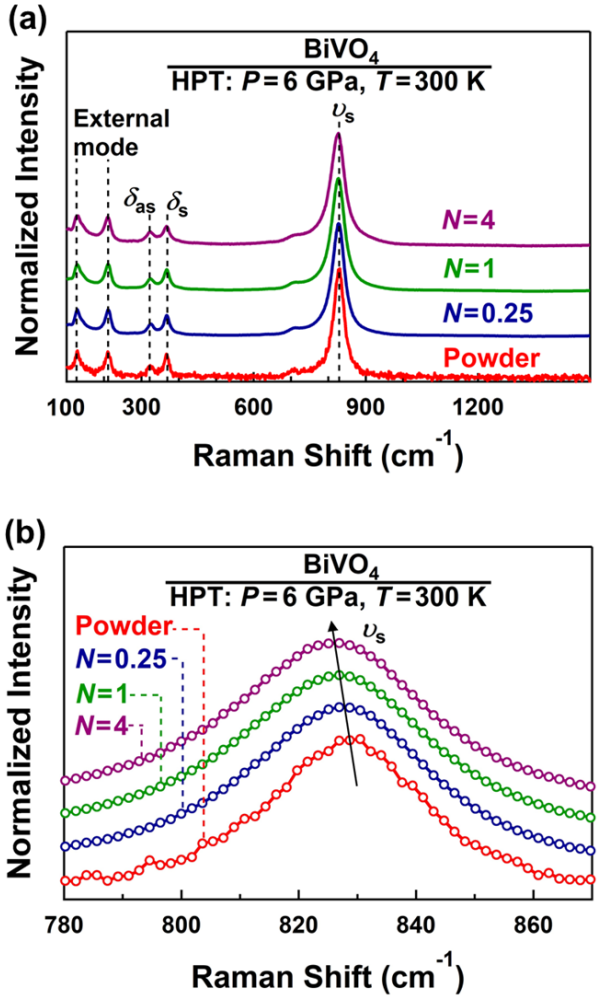


Fig. 2.4. Introduction of lattice strain in $BiVO_4$ by HPT processing. (a) Raman spectroscopy, and (b) Raman spectroscopy in high magnification for stretching vibration mode of V-O bonds for initial powder and samples processed for 0.25, 1 and 4 turns.

Fig. 2.4b shows the Raman spectra of stretching vibration mode of the V-O bonds in higher magnification. It is evident that there is a peak shift to the lower wavenumbers after HPT processing and the shift is enhanced by increasing the number of turns. This shift indicates that a lattice expansion (tensile strain) occurs in the samples [33].

The distribution of particle size of the four samples measured by DLS is shown in Fig. 2.5. The average particles size for the initial powder is 370 nm, but it increases to 420, 540 and 540 nm after HPT processing for 0.25, 1 and 4 turns, respectively. It is concluded that despite decreasing the crystallite size by HPT processing, the specific surface area decreases after HPT processing: 3.8 $m^2g^{-1}$ for the initial powder and 3.4, 2.6 and 2.6 $m^2g^{-1}$ for the samples processed by HPT for 0.25, 1 and 4 turns, respectively. Such a decrease in specific surface area, which is a consequence of high applied pressure and large plastic deformation, was reported in a wide range of HPT-processed materials [20,21].

Fig. 2.6 shows the microstructure analysis by TEM for four samples in the BF, DF and SAED modes. It should be noted the dark and bright colors in the BF and DF images are due to the diffraction contrasts. The white regions in the DF images correspond to grains having the diffracted beam indicated by arrows in the SAED profiles. The SAED profile has a dotted pattern, and only one grain with the submicrometer size is observed in the initial powder. After HPT processing for 0.25 turns, a combination of doted and ring patterns is observed in the SAED profiles, indicating grain refinement to the nanometer sizes partially occurs, as is also evident in the DF images with some nanosized white regions. The ring pattern of SAED analyses after 1 and 4 turns and the presence of many white nanosized regions in DF images confirm that the initial submicrometer grain sizes are refined to the nanometer sizes. The average grain size after 4 HPT turns is 15 nm, which is in reasonable agreement with the crystallite size value measured by the XRD analysis in Fig. 2.3c. Such a decrease in the crystal size is a consequence of large plastic deformation, as reported in a wide range of HPT-processed oxides [21,22,26].

The nanostructural evolution is shown more clearly in Fig. 2.7 using the TEM high-resolution images for (a) the initial powder, and for the samples processed by HPT for (b) 0.25, (c, d) 1 and (e, f) 4 turns. The high-resolution images confirm the presence of monoclinic lattice structure in all samples in good agreement with the XRD analysis and Raman spectroscopy. Moreover, while the initial powder contains large crystals, numerous nanograins are formed after HPT processing. In addition to the formation of nanograins with high-angle grain boundaries,

dislocations are also detected within some crystals, as shown in Fig. 2.7d. The presence of large fractions of grain boundaries and dislocations and resultant lattice distortion is consistent with the XRD peak broadening. The evolution of nanostructure to a defective and distorted state is supposed to contribute to an easier electron and hole separation in this material [16].

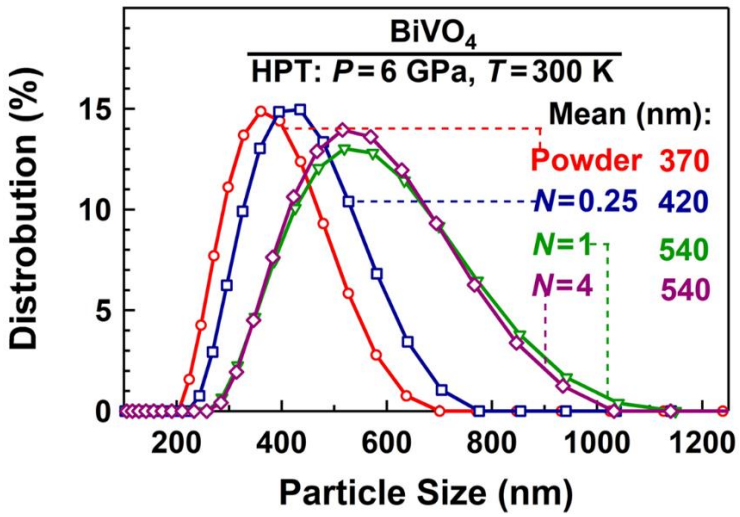


Fig. 2.5. Increasing average particle size of $BiVO_4$ by HPT processing. Particle size distribution, determined using DLS method, for initial powder and samples processed for 0.25, 1 and 4 turns.

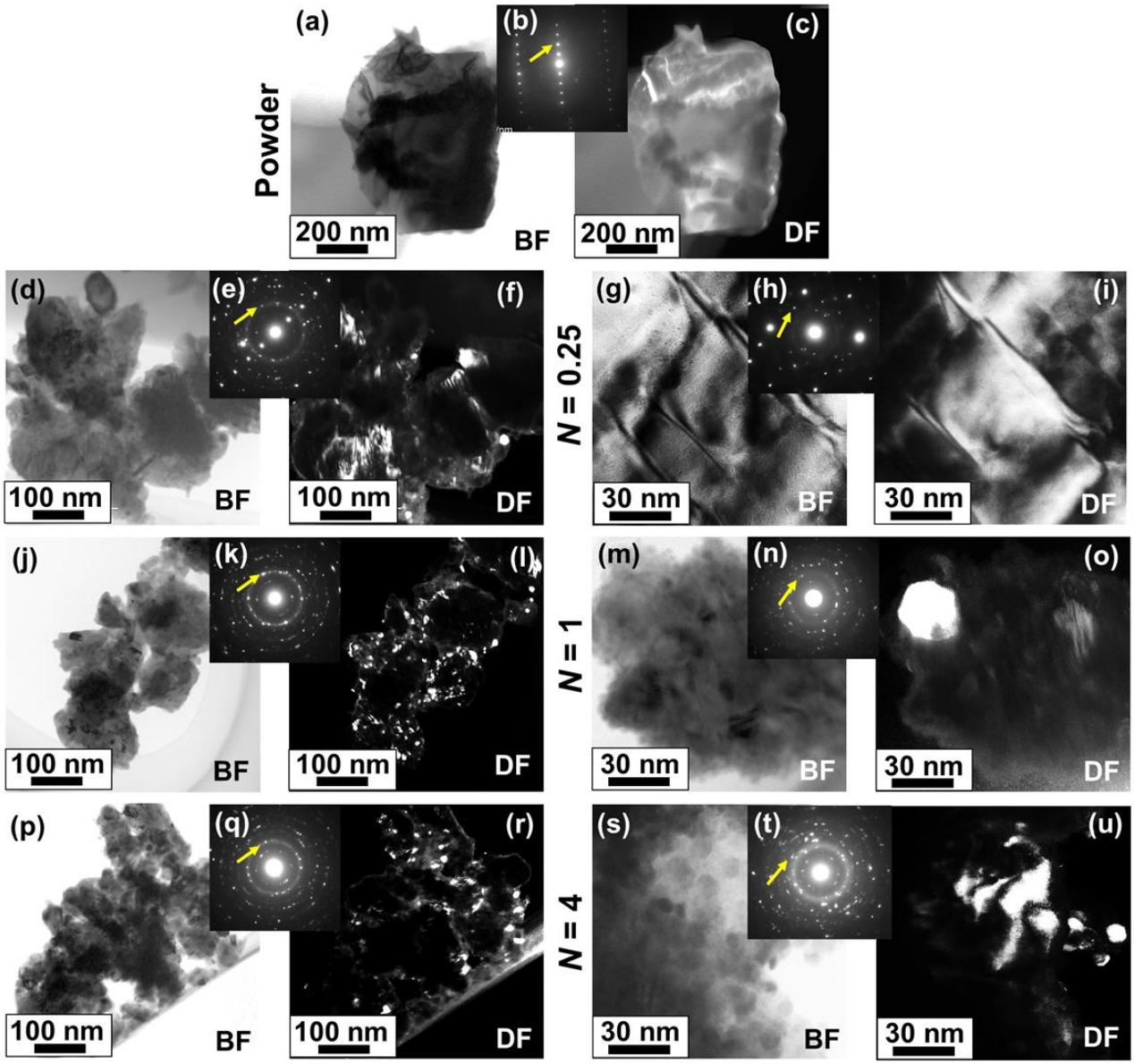


Fig. 2.6. Formation of nanograins in $BiVO_4$ by HPT processing. TEM BF images, SAED analyses and DF images taken with diffracted beams indicated by arrows in SAED analyses for (a-c) initial powder and samples processed for (d-i) 0.25, (j-o) 1 and (p-u) 4 turns.

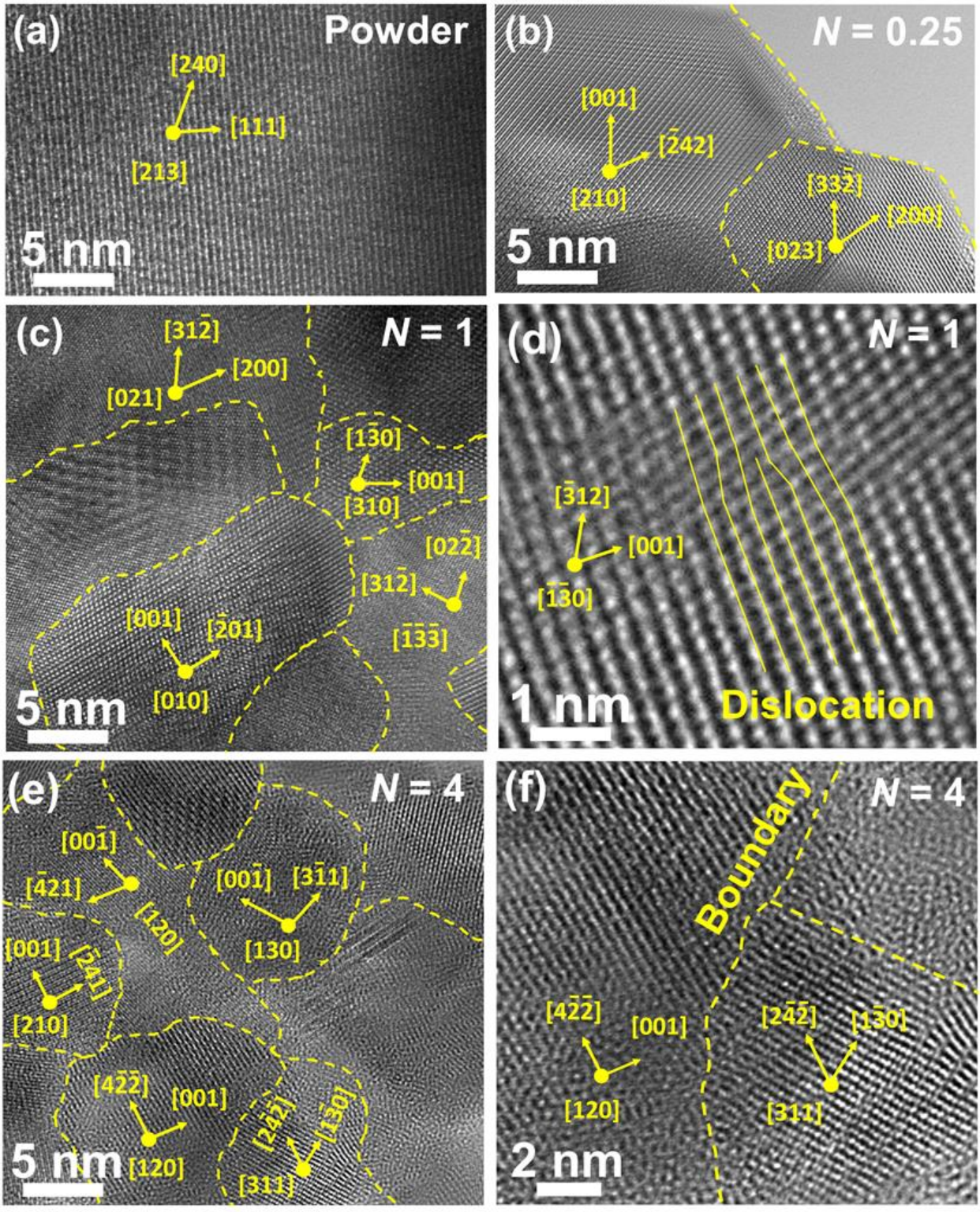


Fig. 2.7. Coexistence of grain boundaries and dislocations in $BiVO_4$ after HPT processing. TEM high-resolution images for (a) initial powder and for samples processed for (b) 0.25, (c, d) 1 and (e, f) 4 turns.

### *2.3.2. Oxygen vacancy formation*

The changes of the color of samples from yellow for the initial powder to orange for the samples processed with 0.25 and 1 turns and to rose for the sample processed with 4 turns (Fig. 2.1c) indicates that the color centers such as oxygen vacancies should have formed after HPT processing [26]. The lattice expansion, confirmed by XRD peak shift in Fig. 3b and by Raman spectroscopy in Fig. 2.4b, also indirectly suggests that vacancy-type defects can be formed by HPT processing [28,29,32]. In addition to these evidences, the presence of oxygen vacancies can be analyzed by XPS and EPR analyses.

The XPS spectra of initial powder and samples processed by HPT are shown in Fig. 2.8 for (a) Bi 4f, (b) V 2p and (c) O 1s. Examination of XPS data confirms that the main oxidation states of three elements are $Bi^{3+}$, $V^{5+}$ and $O^{2-}$. The Bi 4f and V 2p spectra do not show a clear change after HPT processing. However, the O 1s spectra in Fig. 2.8c after HPT processing show small shoulders at high energies, indicating the formation of oxygen vacancies [25]. To quantify, the concentration of oxygen vacancies using XPS, peak deconvolution for the O 1s spectra was conducted by considering two components in the spectra: (i) oxygen at lattice sites $O_L$, and (ii) oxygen vacancies $O_V$. The peak positions for $O_L$ and $O_V$ in Fig. 2.8c were considered at 529.9 and 530.7 eV, respectively [34,35]. It is evident that the intensity of oxygen vacancy peak systematically increases with increasing the number of HPT turns. The intensity ratio for $O_V$ to $O_V+O_L$, as an indication for surface oxygen vacancy concentration, is plotted in Fig. 2.8d for the four samples. The concentration of surface oxygen vacancy reaches ~15% after HPT processing for 4 turns, although this value may be overestimated due to the influence of adsorbed oxygen on O 1s spectra [35].

The EPR spectra for the four samples are shown in Fig. 2.8e, in which the electron spin resonance intensity is plotted against the dimensionless magnetic moment or $g$ factor ($g = h\nu/\mu_B B_0$, h: Planck constant, $\nu$: frequency, $\mu_B$: magnetic field; $B_0$: Bohr magneton constant [36,37]). For all samples, peak pairs with opposite curvatures are observed, while the intensity of these peaks increases with increasing the number of HPT turns. For the sample processed for 4 turns, the turning points of these peaks are close to a $g$ factor of 2. Since it was reported that a $g$ factor of 1.978 for $BiVO_4$ corresponds to oxygen vacancies [39], it is concluded that some amounts of oxygen vacancies are present after HPT processing and particularly after 4 turns. The formation of vacancies by HPT processing, which was reported in both metallic [40,41] and non-metallic

materials [22,23], is due to the plastic deformation effects on vacancy formation and due to the high-pressure effects on suppressing the vacancy annihilation.

### *2.3.3. Electronic structure*

UV-vis spectroscopy and UPS analysis were employed to examine the light absorbance, bandgap and electronic band structure of $BiVO_4$. Fig. 2.9a shows the light absorbance of the four samples. All samples mainly absorb the light in the UV region, but the light absorbance in the visible region improves after HPT processing and particularly after 4 turns, indicating a better electron-hole separation after HPT processing. Light absorbance edge tends to transfer from the blue light region to the green light region after HPT processing for 4 turns, which is in agreement with the prediction of the Itten color wheel in Fig. 2.1c. The Kubelka-Munk analysis is shown in Fig. 2.9b for estimation of the direct bandgap. A bandgap narrowing occurs by HPT processing and the bandgap decreases from 2.4 eV for the initial powder to 2.3 eV for the samples processed with 0.25 and 1 turns and to 2.1 eV for the sample processed with 4 turns. Since no phase transformations occur in $BiVO_4$ by HPT processing, such a bandgap narrowing should be due to the introduction of lattice defects and strain [42-45,18].

Fig. 2.9c shows the UPS spectra of four samples which are used to determine the top of the valence band from the vacuum level. The top of the valence band from the vacuum level was calculated as cutoff energy from the Fermi level ($E_0$ indicated by arrows in Fig 2.9c) - valence band top energy from the Fermi level ($E_B$ indicated by arrows in Fig. 2.9c) - UV He-I energy (21.2 eV) [46]. The top of the valence band for the initial powder and the samples processed by HPT for 0.25, 1 and 4 turns is -6.4, -6.0, -6.0 and -6.0 eV versus the vacuum level, respectively. By the addition of bandgap values to the top of the valence band, the bottom of the conduction band can be determined as -4.7, -3.7, -3.7 and -3.9 eV for the initial powder and the samples processed by HPT for 0.25, 1 and 4, respectively.

Fig. 2.9d shows the band structure of four samples, while the numbers in the figure are the positions of the top of the valence band and the bottom of the conduction band versus the normal hydrogen electrode (NHE): energy vs. NHE = -4.4 - energy vs. vacuum [46]. For the initial powder, the bandgap, the top of the valence band and the bottom of the conduction band are in agreement with the reported data in the literature [47].

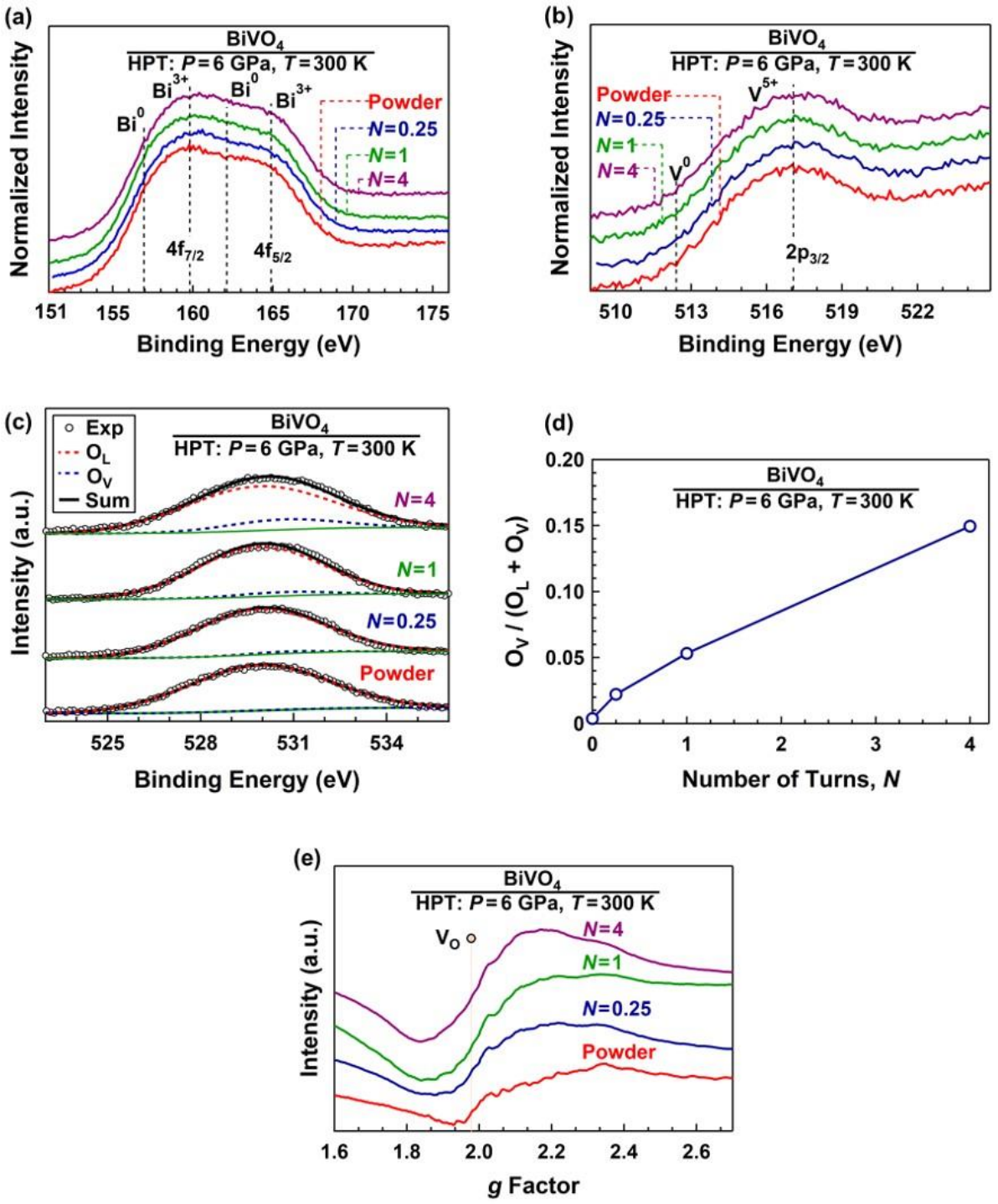


Fig. 2.8. Formation of oxygen vacancies in $BiVO_4$ after HPT processing. XPS spectroscopy of (a) Bi 4f, (b) V 2p and (c) O 1s and its peak deconvolution; (d) ratio of surface oxygen vacancy peak ($O_V$) to sum of lattice oxygen and vacancy peaks ($O_L$ + $O_V$) plotted versus number of HPT turns; and (e) EPR spectroscopy for initial powder and samples processed for 0.25, 1 and 4 turns.

After HPT processing, in addition to bandgap narrowing the bottom of the conduction band increases, suggesting that the problem of low conduction band bottom of $BiVO_4$ [2,3] can be successfully solved by the introduction of lattice defects and strain. As shown in Fig. 2.9d, the electronic structure of all four samples can support the $CO_2$ conversion reactions by considering the relevant chemical potentials for different reactions [48,49]. However, the HPT-processed samples have a higher overpotential for $CO_2$ conversion, which is thermodynamically desirable for photocatalysis.

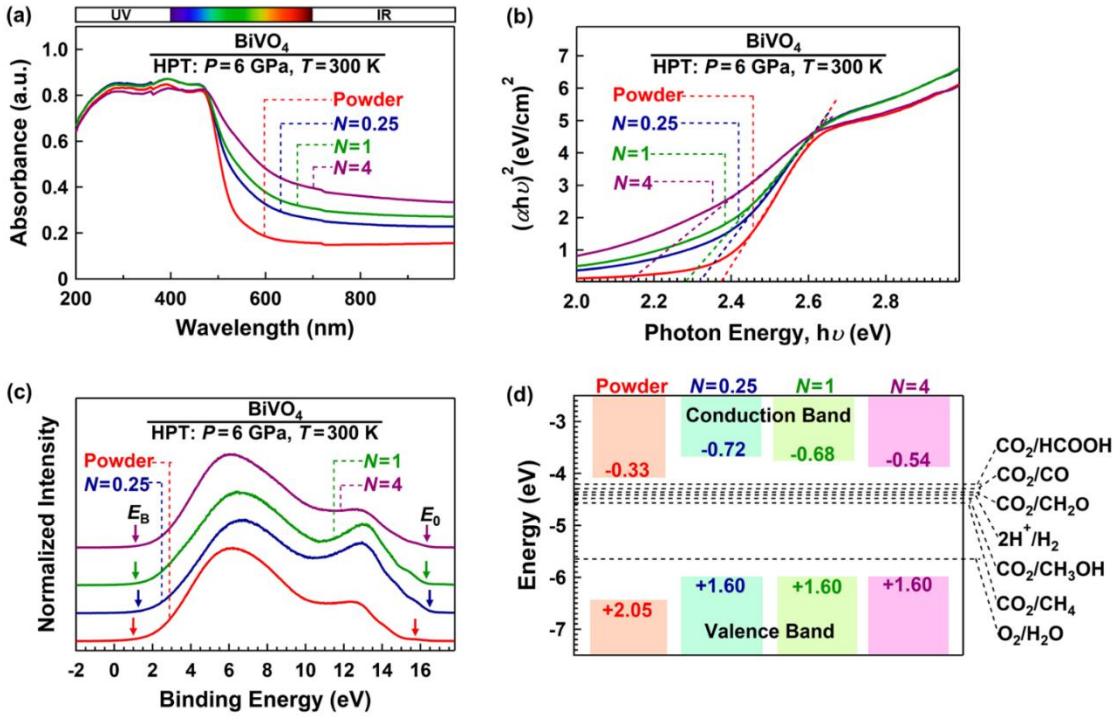


Fig. 2.9. Bandgap narrowing and improvement of electronic band structure of $BiVO_4$ for photocatalytic $CO_2$ conversion by HPT processing (a) UV-vis spectroscopy, (b) Kubelka-Munk analysis for direct bandgap calculation ($\alpha$: light absorption, h: Planck's constant, $v$: photon frequency), (c) UPS spectroscopy using bias of -4 V to measure the top of the valence band, and (d) electronic band structure including chemical potentials for $CO_2$ reduction reactions for initial powder and samples processed for 0.25, 1 and 4 turns. Arrows on left and right in (c) indicate the valence band top energy ($E_B$) and cutoff energy ($E_0$) shifted 4 eV lower from Fermi level, respectively. Numbers in (d) shows energy levels versus normal hydrogen electrode (NHE).

While earlier studies used the heterojunctions to solve the problem of the electronic structure of $BiVO_4$ [3-8], this study confirms that engineering the lattice defects and strain is effective to improve the electronic structure of pure $BiVO_4$ without any need for a second phase or impurity atoms.

### *2.3.4. Charge carrier dynamics*

Fig. 2.10 shows (a) PL spectroscopy, (b) PL decay analysis and (c) photocurrent measurements which can give information about charge carrier dynamics including the recombination of electrons and holes, mobility of charge carriers and defect trapping [49]. Fig. 2.10a shows a significant decrease in PL intensity after HPT processing, indicating that the recombination rate of electrons and holes decreases effectively after HPT processing. These results suggest that the HPT-induced defects and strain act positively as electron-hole separation sites rather than recombination sites [4,11,26]. The PL peak for all samples appeared at a peak around 650 nm (1.9 eV) which is less than the bandgap of samples. Although electron-hole recombination in $BiVO_4$ can happen radiatively or nonradiatively, the emission detected around 650 nm in Fig. 2.10a was attributed to the radiative recombination of electrons and holes on defects [39,48].
PL decay spectra shown in Fig. 2.10b follow a relation shown below [49].

$$I(t) = A_1 \exp\left(-\frac{t}{\tau_1}\right) + A_2 \exp\left(-\frac{t}{\tau_2}\right) \quad (2.2)$$

where, $I(t)$, $A_1, A_2$, $\tau_1$ and $\tau_2$ are PL decay intensity at time $t$, the amplitude of the first exponential function, amplitude of the second exponential function, fast decay time and slow decay time, respectively. The average lifetime can be calculated using the following equation [49].

$$\tau_{ave} = \frac{A_1\tau_1^2 + A_2\tau_2^2}{A_1\tau_1 + A_2\tau_2} \quad (2.3)$$

Values of $A_1, A_2$, $\tau_1$, $\tau_2$ $\tau_{ave}$ for the initial powder and the samples processed by HPT are presented in Table 2.2. The average electron lifetime decreases from 12.90 ns for the initial powder to 11.48, 10.22 and 9.24 ns for the samples processed for 0.25, 1 and 4 turns, respectively. The decrease in the lifetime for HPT samples can be attributed to the formation of oxygen vacancies. Oxygen vacancies on the surface of photocatalyst act as shallow traps or active sites for the fast migration of electrons and participation in a reaction. Therefore, their formation can lead to a decrease in the exited electron lifetime and an increase in the photocatalytic activity [26,35]. It

should be noted that the oxygen vacancies in the bulk can also lead to electron migration and a decrease in the lifetime, but they do not necessarily improve the photocatalytic activity [16,50,51].

Photocurrent measurements in Fig. 2.10c demonstrate that the current density is the highest for the initial powder and decreases with HPT processing and increasing the number of turns. Since photocurrent generation is attributed to the migration of electrons from the surface under an external voltage, Fig. 2.10c suggests that electron separation from the surface of $BiVO_4$ becomes weaker after HPT processing. Such a decrease in photocurrent may not be due to enhanced electron-hole recombination because the PL intensity (as an indication of recombination) decreases after HPT processing, as shown in Fig. 2.10a. The decreases in photocurrent density after HPT processing should be due to the action of surface vacancies as electron trapping sites. It was shown earlier that polarity and localization of photoexcited electrons of $BiVO_4$ can lead to electron trapping in this material [52]. Such trapping can be enhanced on oxygen vacancies, making these defects active sites with sufficient electrons for chemical reactions (particularly if they form near the bottom of the conduction band and act as shallow donors) [53]. Theoretical studies suggested that a change of the oxygen vacancy states from the shallow donors to localized intragap states can reduce the photoconductivity and photocurrent of $BiVO_4$ [53], but this is not the case in this study because the PL spectra in Fig. 2.10a show similar peak energies for all four samples.

Table 2.2. Decreasing electron lifetime in $BiVO_4$ by HPT processing. PL decay parameters and electron lifetimes for initial powder and for samples processed for 0.25, 1 and 4 turns.

| Sample | $\tau_1$ (ns) | $\tau_2$ (ns) | $A_1$ | $A_2$ | $\tau_{ave}$ (ns) |
|---|---|---|---|---|---|
| Powder | 2.17 | 14.92 | 56.56 | 43.44 | 12.90 |
| $N$ = 0.25 | 1.92 | 13.08 | 53.19 | 46.81 | 11.48 |
| $N$ = 1 | 1.78 | 12.40 | 64.26 | 35.74 | 10.22 |
| $N$ = 4 | 1.62 | 10.35 | 48.09 | 51.91 | 9.24 |

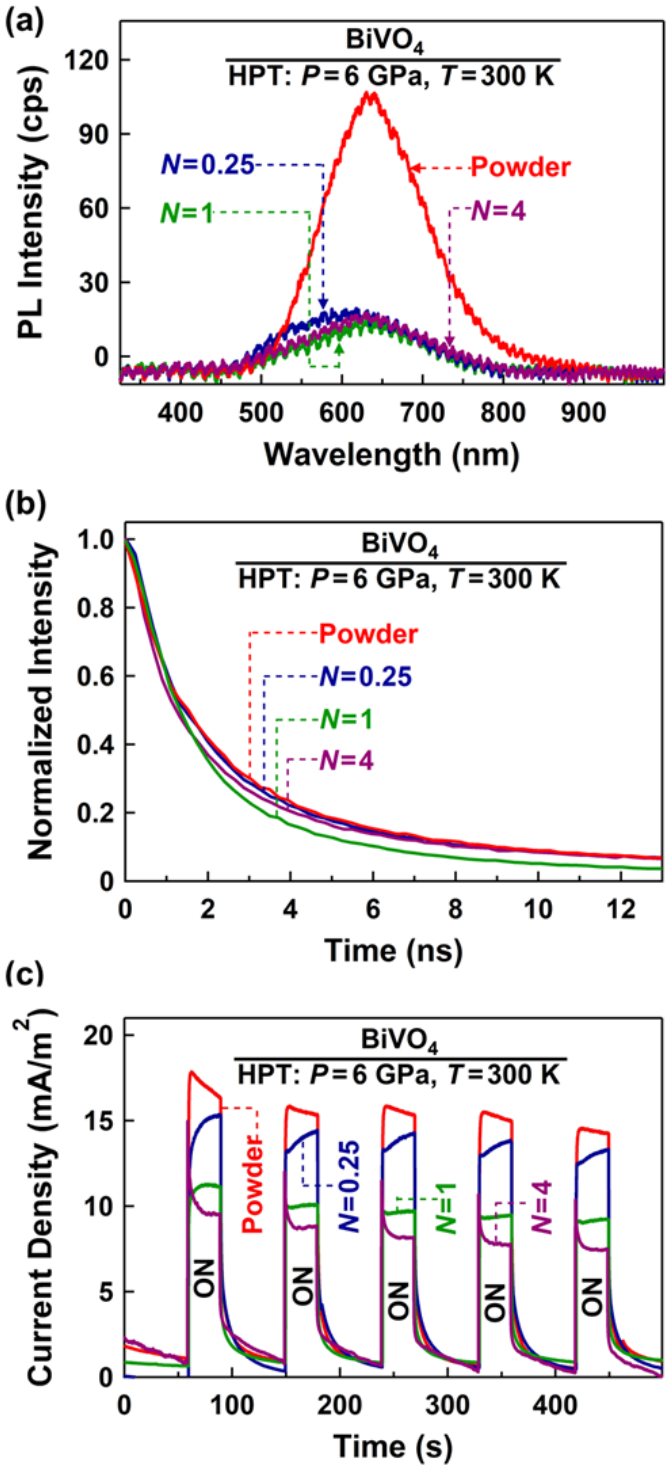


Fig. 2.10. Decreasing recombination of electrons and holes in $BiVO_4$ after HPT processing. (a) Steady-state PL emission spectra, (b) time-resolved PL decay spectra, and (c) photocurrent density versus time for initial powder and samples processed for 0.25, 1 and 4 turns.

### *2.3.5. Photocatalytic activity*

Photocatalytic $CO_2$ to CO conversion activity of the initial powder and the samples processed by HPT for 0.25, 1 and 4 turns are shown in Fig. 2.11a versus the catalyst mass unit and in Fig. 2.11b versus the catalyst surface area unit. Since the photocatalytic reactions occur on the surface of photocatalysts, normalizing the CO production rates per surface area is more reasonable to show the differences. It should be noted that the photocatalytic tests were conducted two times in Figs. 2.11a and 2.11b for the initial powder and for the sample processed with $N = 4$ to confirm the reproducibility of data. All samples could convert $CO_2$ to CO, but the photocatalytic performance of HPT-processed samples is better than the initial powder. The sample processed for 4 turns shows the highest activity. The average of CO production rate for the powder is 2.27 ± 0.24 $\mu molh^{-1}g^{-1}$ (0.60 ± 0.06 $\mu molh^{-1}m^{-2}$) which increases to 3.21 ± 0.23, 3.35 ± 0.27 and 3.97 ± 0.38 $\mu molh^{-1}g^{-1}$ (0.96 ± 0.07, 1.27± 0.10 and 1.45± 0.08 $\mu molh^{-1}m^{-2}$) for the samples proceeded for 0.25, 1 and 4 turns, respectively. Here, it should be noted that no hydrocarbons such as $CH_4$ and no oxidation products such as $O_2$ were detected within the detection limits of the experiments. The absence of the oxidation products should be a reason for the gradual decrease in the activity during the time. It should be mentioned that the result of the blank test before the photocatalytic activity test (addition of catalysts without light irradiation) shows that the production rate of CO is zero (the data point at $t = 0$ h). Moreover, a blank test without the addition of catalyst with light irradiation shows no CO production within 8 h, as shown in Fig. 2.11a and 2.11b. The improvement of photocatalytic activity of $BiVO_4$ after HPT processing should be due to the presence of oxygen vacancies as active sites for adsorption and conversion of $CO_2$ molecules as well as due to the effect of lattice strain on the improvement of band structure for $CO_2$ photoreduction [2,54].

Fig. 2.11c demonstrates the structure stability of powder and samples processed by HPT after photocatalytic test using the XRD analysis. All samples are stable and retain their monoclinic structure after use for photocatalytic $CO_2$ conversion. No chemical reaction, corrosion or degradation products are detected by XRD analysis. Since some photocatalysts are negatively influenced by photocorrosion phenomenon, finding the photocorrosion-resistant catalysts is a critical issue [55,56]. In some $BiVO_4$-based catalysts, it was reported that the photocorrosion and formation of bismuth oxides can occur by dissolving vanadium into the solution through the

accumulation of holes on the surface [55,56]. The absence of such photocorrosion products confirms the stability of current HPT-processed photocatalysts.

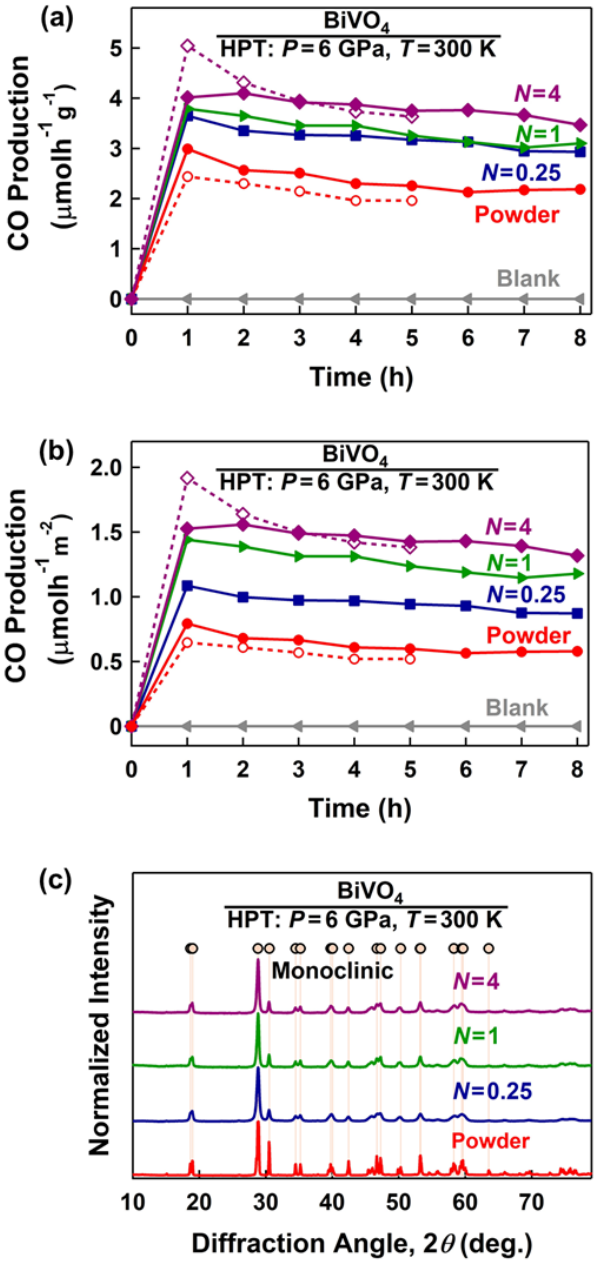


Fig. 2.11. Improvement of photocatalytic $CO_2$ conversion on highly-stable $BiVO_4$ after HPT processing. CO production rate under UV irradiation versus time normalized by (a) mass unit and (b) surface area of catalysts; and (c) XRD profiles after photocatalytic test for initial powder and samples processed for 0.25, 1 and 4 turns. Photocatalytic tests were repeated two times for initial powder and sample processed for 4 turns.

## 2.4. Discussion

This chapter shows that the simultaneous introduction of strain and oxygen vacancies into $BiVO_4$ can lead to improving the light absorbance, narrowing the bandgap, modifying the electronic band structure, decreasing the recombination rate of electrons and holes and finally enhancing the photocatalytic activity for $CO_2$ conversion. Unlike earlier strategies that mainly used heterojunctions [3-8] or doping [9-13] to deal with the low level of the conduction band in $BiVO_4$ [2,3], this study shows that the level can be enhanced even in pure $BiVO_4$ by the accumulation of oxygen vacancies and lattice strain. Due to the presence of unpaired electrons in surface oxygen vacancies, they can act as adsorption sites to uptake $CO_2$ as a Lewis acid [43,57]. These vacancies also contribute to the activation of adsorbed $CO_2$ and $H_2O$ for conversion to intermediate and final products by weakening the carbon-oxygen and oxygen-hydrogen bondings [43]. The oxygen vacancies on the surface do not usually act as recombination sites for electrons and holes, but they trap the excited electrons and provide active sites for photocatalytic reactions [57-59]. Here, it should be noted that the concentration of oxygen vacancies in $BiVO_4$ as activation sites should be an optimum level because large fractions of oxygen vacancies can reduce $V^{5+}$ to $V^{4+}$, resulting in electron scattering due to a large ionic diameter of $V^{4+}$ [29,60,61]. A high concentration of $V^{4+}$ can lead to decreasing the length of effective diffusion of holes and accordingly reduce the photocatalytic activity [62]. Despite these expected effects of oxygen vacancies, the overall effect of oxygen vacancies in this study is the improvement of photocatalytic activity. On the other hand, lattice strain can lead to electronic band structure modification such as changing the level of the conduction band bottom or decreasing the bandgap [18,19,45]. Therefore, in the current HPT-processed $BiVO_4$ photocatalysts, increasing the light absorbance, decreasing the bandgap, and increasing the bottom of the conduction band energy are the results of the contribution of lattice strain, while decreasing the electron-hole recombination and improvement of surface catalytic activity are the main contribution of oxygen vacancies.

Here, to have a clear view regarding the improvement of photocatalytic $CO_2$ conversion of highly-strained and defective $BiVO_4$, some comparisons can be made. Fig. 2.12 compares the CO production rate of this material with P25 $TiO_2$, which is a typical benchmark photocatalyst. Note that both materials were examined exactly under similar conditions by the current authors. The average of photocatalytic CO production of P25 $TiO_2$ is $4.63 \pm 0.33$ $\mu molh^{-1}g^{-1}$ which is close to the productivity of HPT-processed $BiVO_4$ after 4 turns ($3.97 \pm 0.38$ $\mu molh^{-1}g^{-1}$). Here, it should

be noted that the surface area of P25 $TiO_2$ is 38.70 $m^2g^{-1}$ which is much higher than the surface area of HPT-processed $BiVO_4$ (2.6 $m^2g^{-1}$). Despite the negative effect of the HPT method on the reduction of the surface area [21,28], Fig. 2.12 confirms the efficiency of the defect and strain engineering in improving the photocatalytic activity to high levels comparable with one of the most active photocatalysts. Another comparison is given in Table 2.3, in which photocatalytic activity of HPT-processed $BiVO_4$ was compared with some data for $BiVO_4$-based photocatalysts [4-13]. It should be noted that data in Table 2.3 should be compared with care because of the differences in experimental conditions in various studies (e.g., light source, photoreactor type, the mass of catalyst, etc.). Despite these differences, the range of reported photocatalytic CO production rate for these materials is between 0.05-13.5 $\mu molh^{-1}g^{-1}$, while the HPT-processed $BiVO_4$ shows one of the highest activities.

Finally, it is worth mentioning that the HPT method used in this study for the generation of defects and strain is applicable to any kind of conventional oxides [20,21] and multi-component ceramics and salts [63]. Although the method was used earlier by the authors to improve the photocatalytic $CO_2$ conversion by synthesis of high-pressure phases [27] or high-entropy oxides [28], its current application to introduce strain and defects is applicable to a wider range of materials to develop advanced photocatalysts for $CO_2$ conversion. Since the specific surface area is usually small after HPT processing, other alternative mechanical or chemical routes may be employed in the future for simultaneous generation of strain and defects in photocatalysts, while keeping their surface area large.

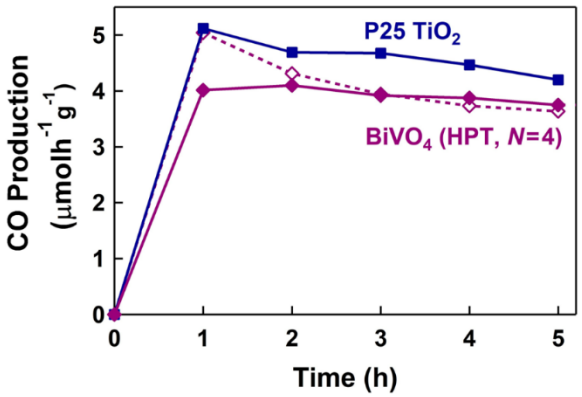


Fig. 2.12. High photocatalytic $CO_2$ conversion activity of highly-strained and oxygen-deficient $BiVO_4$ in comparison with P25 $TiO_2$ as benchmark photocatalyst. CO production rate versus irradiation time for $BiVO_4$ processed by HPT for 4 turns and P25 $TiO_2$.

Table 2.3. Photocatalytic CO evolution rate of $BiVO_4$ processed by HPT for 4 turns compared with other $BiVO_4$-based photocatalysts.

| Photocatalyst | Catalyst Mass (mg) | Light Source | CO Production ($\mu molh^{-1}g^{-1}$) | Reference |
|---|---|---|---|---|
| $BiVO_4${110}-Au- $Cu_2O$ | 100 | 300 W Xe (> 420nm) | 1.12 | [4] |
| $BiVO_4${010}-Au- $Cu_2O$ | 100 | 300 W Xe (> 420nm) | 2.02 | [4] |
| $BiVO_4${010}-$Cu_2O$ | 100 | 300 W Xe (> 420nm) | 0.45 | [4] |
| $BiVO_4${010}-Au-($Cu_2O$-Au) | 100 | 300 W Xe (> 420nm) | 2.08 | [4] |
| $BiVO_4$-$Cu_2O$ | ------ | 300 W Xe (> 420nm) | ~0.5 | [5] |
| $BiVO_4$-C- $Cu_2O$ | ------ | 300 W Xe (> 420nm) | 3.01 | [5] |
| $ZnIn_2S_4$-$BiVO_4$ | 100 | 300 W Xe | 4.75 | [6] |
| $BiVO_4$-5 % $Bi_4Ti_3O_{12}$ | 10 | 300 W Xe | ~6.75 | [7] |
| $BiVO_4$-10 % $Bi_4Ti_3O_{12}$ | 10 | 300 W Xe | ~13.5 | [7] |
| $BiVO_4$-20 % $Bi_4Ti_3O_{12}$ | 10 | 300 W Xe | ~6.75 | [7] |
| Bi-$BiVO_4$ | 10 | 300 W Xe (> 420nm) | ~0.75 | [9] |
| Cu-Bi-$BiVO_4$ | 10 | 300 W Xe (> 420nm) | ~11 | [9] |
| $BiVO_4$ | 10 | 300 W Xe (> 420nm) | 0.42 | [11] |
| Bi-$BiVO_4$ | 10 | 300 W Xe (> 420nm) | 1.29 | [11] |
| Ag-Bi-$BiVO_4$ (Ag/Bi = 0.3) | 10 | 300 W Xe (> 420nm) | 3.4 | [11] |
| Ag-Bi-$BiVO_4$ (Ag/Bi = 0.6) | 10 | 300 W Xe (> 420nm) | 5.19 | [11] |
| Ag-Bi-$BiVO_4$ (Ag/Bi = 0.9) | 10 | 300 W Xe (> 420nm) | 4.54 | [11] |
| 1.0%Cu-$BiVO_4$ | 50 | 400 W High-Pressure Hg | 2 | [12] |
| 0.5%Cu-$BiVO_4$ | 50 | 400 W High-Pressure Hg | 4.1 | [12] |
| 0.3%Cu-$BiVO_4$ | 50 | 400 W High-Pressure Hg | 3.9 | [12] |
| Au-$BiVO_4$ | 50 | 300 W Xe (> 420nm) | ~0.05 | [8] |
| CdS-$BiVO_4$ | 50 | 300 W Xe (> 420nm) | ~0.75 | [8] |
| $Cd_{0.5}Zn_{0.5}S$-$BiVO_4$ | 50 | 300 W Xe (> 420nm) | ~1.2 | [8] |
| CdS-Au-$BiVO_4$ | 50 | 300 W Xe (> 420nm) | ~1.1 | [8] |
| $Cd_{0.2}Zn_{0.8}S$-Au-$BiVO_4$ | 50 | 300 W Xe (> 420nm) | ~1.6 | [8] |
| $Cd_{0.5}Zn_{0.5}S$-Au-$BiVO_4$ | 50 | 300 W Xe (> 420nm) | ~2.15 | [8] |
| $Cd_{0.8}Zn_{0.2}S$-Au-$BiVO_4$ | 50 | 300 W Xe (> 420nm) | ~1.3 | [8] |
| $BiVO_4$-2%Co | 30 | 25 W 254 nm Ultraviolet | 0.62 | [13] |
| $BiVO_4$-5%Co | 30 | 25 W 254 nm Ultraviolet | 0.68 | [13] |
| $BiVO_4$-10%Co | 30 | 25 W 254 nm Ultraviolet | 0.83 | [13] |
| $BiVO_4$-15%Co | 30 | 25 W 254 nm Ultraviolet | 1.04 | [13] |
| $BiVO_4$-20%Co | 30 | 25 W 254 nm Ultraviolet | 2.08 | [13] |
| $BiVO_4$ (HPT: $N$ = 4) | 120 | 400 W High-Pressure Hg | 3.97 ± 0.38 | This study |

## 2.5. Conclusion

A photocatalyst with low bandgap, improved band structure and low recombination rate of electrons and holes was produced by simultaneous introduction of oxygen vacancies and lattice strain in $BiVO_4$ via a high-pressure torsion process. The material showed high photocatalytic activity for $CO_2$ to CO conversion with an activity comparable to P25 $TiO_2$ as a benchmark photocatalyst. This study suggests that simultaneous engineering of lattice strain and defects is an effective strategy to produce active photocatalysts for $CO_2$ conversion.

## References


[1] P. Yue, H. She, L. Zhang, B. Niu, R. Lian, J. Huang, L. Wang, Q. Wang, Super-hydrophilic CoAl-LDH on $BiVO_4$ for enhanced photoelectrochemical water oxidation activity, Appl. Catal. B 286 (2021) 119875.

[2] H.L. Tan, R. Amal, Y.H. Ng, Alternative strategies in improving the photocatalytic and photoelectrochemical activities of visible light-driven $BiVO_4$: a review, J. Mater. Chem. A 5 (2017) 16498–16521.

[3] J. Wu, L. Xiong, Y. Hu, Y. Yang, X. Zhang, T. Wang, Z. Tang, A. Sun, Y. Zhoud, J. Shen, Z. Zou, Organic half-metal derived erythroid-like $BiVO_4$/hm-$C_4N_3$ Z-Scheme photocatalyst: Reduction sites upgrading and rate-determining step modulation for overall $CO_2$ and $H_2O$ conversion, Appl. Catal. B 295 (2021) 120277.

[4] C. Zhou, S. Wang, Z. Zhao, Z. Shi, S. Yan, Z. Zou, A facet-dependent schottky- junction Electron shuttle in a $BiVO_4$ {010}-Au-$Cu_2O$ Z-Scheme photocatalyst for efficient charge separation, Adv. Funct. Mater. 28 (2018) 181214.

[5] C. Kim, K.M. Cho, A. Al-Saggaf, I. Gereige, H.T. Jung, Z-scheme photocatalytic $CO_2$ conversion on three-dimensional $BiVO_4$/Carbon-Coated $Cu_2O$ nanowire arrays under visible light, ACS Catal. 8 (2018) 4170–4177.

[6] Q. Han, L. Li, W. Gao, Y. Shen, L. Wang, Y. Zhang, X. Wang, Q. Shen, Y. Xiong, Y. Zhou, Z. Zou, Elegant construction of $ZnIn_2S_4$/$BiVO_4$ hierarchical heterostructures as Direct Z-scheme photocatalysts for efficient $CO_2$ photoreduction, ACS Appl. Mater. Interfaces 13 (2021) 15092–15100.

[7] X. Wang, Y. Wang, M. Gao, J. Shen, X. Pu, Z. Zhang, H. Lin, X. Wang, $BiVO_4$ /$Bi_4Ti_3O_{12}$ heterojunction enabling efficient photocatalytic reduction of $CO_2$ with $H_2O$ to $CH_3OH$ and CO, Appl. Catal. B 270 (2020) 118876.

[8] J. Li, W. Shao, M. Geng, S. Wan, M. Ou, Y. Chen, Combined Schottky junction and doping effect in $Cd_xZn_{1-x}S$@Au/$BiVO_4$ Z-Scheme photocatalyst with boosted carriers charge separation for $CO_2$ reduction by $H_2O$, J. Colloid Interface Sci. 606 (2022) 1469–1476.

[9] L. Huang, Z. Duan, Y. Song, Q. Li, L. Chen, $BiVO_4$ microplates with oxygen vacancies decorated with metallic Cu and Bi nanoparticles for $CO_2$ photoreduction, ACS Appl. Nano Mater. 4 (2021) 3576–3585.

[10] J.F. deBrito, P.G. Corradini, M.V.B. Zanoni, F. Marken, L.H. Mascaro, The influence of metallic Bi in $BiVO_4$ semiconductor for artificial photosynthesis, J. Alloys Compd. 851 (2021) 156912.

[11] Z. Duan, X. Zhao, C. Wei, L. Chen, Ag-Bi/$BiVO_4$ chain-like hollow microstructures with enhanced photocatalytic activity for $CO_2$ conversion, Appl. Catal. A 594 (2020) 117459.

[12] Z. Zhu, C.X. Yang, Y.T. Hwang, Y.C. Lin, R.J. Wu, Fuel generation through photoreduction of $CO_2$ on novel Cu/$BiVO_4$, Mater. Res. Bull. 130 (2020) 110955.

[13] K. Wang, L. Zhang, Y. Su, S. Sun, Q. Wang, H. Wang, W. Wang, Boosted $CO_2$ photoreduction to methane via Co doping in bismuth vanadate atomic layers, Catal. Sci. Technol. 8 (2018) 3115–3122.

[14] S. Gao, B. Gu, X. Jiao, Y. Sun, X. Zu, F. Yang, W. Zhu, C. Wang, Z. Feng, B. Ye, Y. Xie, Highly efficient and exceptionally durable $CO_2$ photoreduction to methanol over freestanding defective single-unit-cell bismuth vanadate layers, J. Am. Chem. Soc. 139 (2017) 3438–3445.

[15] J. Xiong, J. Di, J. Xia, W. Zhu, H. Li, Surface defect engineering in 2D nanomaterials for photocatalysis, Adv. Funct. Mater. 28 (2018) 1801983.

[16] L. Ran, J. Hou, S. Cao, Z. Li, Y. Zhang, Y. Wu, B. Zhang, P. Zhai, L. Sun, Defect engineering of photocatalysts for solar energy conversion, Sol. RRL 4 (2020) 1900487.

[17] Y. Huang, Y. Yu, Y. Yu, B. Zhang, Oxygen vacancy engineering in photocatalysis, Sol. RRL 4 (2020) 2000037.

[18] J. Di, P. Song, C. Zhu, C. Chen, J. Xiong, M. Duan, R. Long, W. Zhou, M. Xu, L. Kang, B. Lin, D. Liu, S. Chen, C. Liu, H. Li, Y. Zhao, S. Li, Q. Yan, L. Song, Z. Liu, Strain-

engineering of $Bi_2O_{17}Br_2$ nanotubes for boosting photocatalytic $CO_2$ reduction, ACS Mater. Lett. 2 (2020) 1025–1032.

[19] X. Cai, F. Wang, R. Wang, Y. Xi, A. Wang, J. Wang, B. Teng, S. Bai, Synergism of surface strain and interfacial polarization on Pd@Au core-shell cocatalysts for highly efficient photocatalytic $CO_2$ reduction over $TiO_2$, J. Mater. Chem. A 8 (2020) 7350–7359.

[20] K. Edalati, Z. Horita, A review on high-pressure torsion (HPT) from 1935 to 1988, Mater. Sci. Eng. A 652 (2016) 325–352.

[21] K. Edalati, Review on recent advancements in severe plastic deformation of oxides by high-pressure torsion (HPT), Adv. Eng. Mater. 21 (2019) 1800272.

[22] K. Edalati, A. Bachmaier, V.A. Beloshenko, Y. Beygelzimer, V.D. Blank, W.J. Botta, K. Bryła, J. Čížek, S. Divinski, N.A. Enikeev, Y. Estrin, G. Faraji, R.B. Figueiredo, M. Fuji, T. Furuta, T. Grosdidier, J. Gubicza, A. Hohenwarter, Z. Horita, J. Huot, Y. Ikoma, M. Janeček, M. Kawasaki, P. Krăl, S. Kuramoto, T.G. Langdon, D.R. Leiva, V.I. Levitas, A. Mazilkin, M. Mito, H. Miyamoto, T. Nishizaki, R. Pippan, V.V. Popov, E.N. Popova, G. Purcek, O. Renk, Á. Révész, X. Sauvage, V. Sklenicka, W. Skrotzki, B.B. Straumal, S. Suwas, L.S. Toth, N. Tsuji, R.Z. Valiev, G. Wilde, M.J. Zehetbauer, X. Zhu, Nanomaterials by severe plastic deformation: review of historical developments and recent advances, Mater. Res. Lett. 10 (2022) 163–256.

[23] K. Edalati, R. Uehiro, S. Takechi, Q. Wang, M. Arita, M. Watanabe, T. Ishihara, Z. Horita, Enhanced photocatalytic hydrogen production on GaN-ZnO oxynitride by introduction of strain-induced nitrogen vacancy complexes, Acta Mater. 185 (2020) 149–156.

[24] R.P.I. Halder, C.N.J. Wagner, X-Ray diffraction study of the effects of solutes on the occurrence of stacking faults in silver-base alloys, J. Appl. Phys. 33 (1962) 3451–3458.

[25] J. Chastain, Handbook of X-ray Photoelectron Spectroscopy, Perkin-Elmer Corporation, Eden Prairie, MN, USA, 1992.

[26] S. Akrami, M. Watanabe, T.H. Ling, T. Ishihara, M. Arita, M. Fuji, K. Edalati, High pressure $TiO_2$-II polymorph as an active photocatalyst for $CO_2$ to CO conversion, Appl. Catal. B 298 (2021) 120566.

[27] S. Akrami, Y. Murakami, M. Watanabe, T. Ishihara, M. Arita, M. Fuji, K. Edalati, Defective high-entropy oxide photocatalyst with high activity for $CO_2$ conversion, Appl. Catal. B 303 (2022) 120896.

[28] Z. Zhang, F. Zhou, E.J. Lavernia, On the analysis of grain size in bulk nanocrystalline materials via x-ray diffraction, Metall. Mater. Trans. 34 (2003) 1349–1355.

[29] Q. Luo, L. Zhang, X. Chen, O.K. Tan, K.C. Leong, Mechanochemically synthesized m-$BiVO_4$ nanoparticles for visible light photocatalysis, RSC Adv. 6 (2016) 15796-15802.

[30] K. Nakagawa, M. Hayashi, K. Takano-Satoh, H. Matsunaga, H. Mori, K. Maki, Y. Onuki, S. Suzuki, S. Sato, Characterization of dislocation rearrangement in FCC metals during work hardening using X-ray diffraction line-profile analysis, Quantum Beam Sci. 4 (2020) 36.

[31] J.M. Wu, Y. Chen, L. Pan, P. Wang, Y. Cui, D. Kong, L. Wang, X. Zhang, J.J. Zou, Multi-layer monoclinic $BiVO_4$ with oxygen vacancies and $V^{4+}$ species for highly efficient visible-light photoelectrochemical applications, Appl. Catal. B. 221 (2018) 187–195.

[32] P. Stathi, M. Solakidou, Y. Deligiannakis, Lattice defects engineering in W-, Zr-doped $BiVO_4$ by flame spray pyrolysis: enhancing photocatalytic $O_2$ evolution, Nanomaterials 11 (2021) 501.

[33] J. Xu, Z. Bian, X. Xin, A. Chen, H. Wang, Size dependence of nanosheet $BiVO_4$ with oxygen vacancies and exposed {0 0 1} facets on the photodegradation of oxytetracycline, Chem. Eng. J. 337 (2018) 684–696.

[34] M. Guo, Y. Wang, Q. He, W. Wang, W. Wang, Z. Fua, H. Wang, Enhanced photocatalytic activity of S-doped $BiVO_4$ photocatalysts, RSC Adv. 5 (2015) 58633–58639.

[35] X. Yuan, X. Sun, H. Zhou, S. Zeng, B. Liu, X. Li, D. Liu, Free-standing electrospun W-doped $BiVO_4$ porous nanotubes for the efficient photoelectrochemical water oxidation, Front. Chem.8 (2020) 311.

[36] Q. Pan, K. Yang, G. Wang, D. Li, J. Sun, B, Yang, Z. Zou, W. Hu, K. Wen, H. Yang, $BiVO_4$ nanocrystals with controllable oxygen vacancies induced by Zn-doping coupled with graphene quantum dots for enhanced photoelectrochemical water splitting, Chem. Eng. J. 372 (2019) 399–407.

[37] J.A. Weil, J.R. Bolton, Electron Paramagnetic Resonance: Elementary Theory and Practical Applications, John Wiley & Sons, 2007.

[38] A. Schweiger, G. Jeschke, Principles of Pulse Electron Paramagnetic Resonance, Oxford University Press on Demand, 2001.

[39] W. Qiu, S. Xiao, J. Ke, Z. Wang, S. Tang, K. Zhang, W. Qian, Y. Huang, D. Huang, Y. Tong, S. Yang, Freeing the polarons to facilitate charge transport in $BiVO_4$ from oxygen vacancies with an oxidative 2D precursor, Angew. Chem. 131 (2019) 19263–19271.

[40] B. Oberdorfer, B. Lorenzoni, K. Unger, W. Sprengel, M. Zehetbauer, R. Pippan, R. Wurschum, Absolute concentration of free volume-type defects in ultrafine-grained Fe prepared by high-pressure torsion, Scr. Mater. 63 (2010) 452–455.

[41] J. Čížek, M. Janeček, T. Vlasák, B. Smola, O. Melikhova, R.K. Islamgaliev, S.V. Dobatkin, The development of vacancies during severe plastic deformation, Mater. Trans. 60 (2019) 1533–1542.

[42] J. Di, C. Zhu, M. Ji, M. Duan, R. Long, C. Yan, K. Gu, J. Xiong, Y. She, J. Xia, H. Li, Z. Liu, Defect-rich $Bi_{12}O_{17}Cl_2$ nanotubes self-accelerating charge separation for boosting photocatalytic $CO_2$ reduction, Angew. Chem. 57 (2018) 14847–14851.

[43] K. Wang, J. Lu, Y. Lu, C.H. Lau, Y. Zheng, X. Fan, Unravelling the C-C coupling in $CO_2$ photocatalytic reduction with $H_2O$ on $Au/TiO_{2-x}$: combination of plasmonic excitation and oxygen vacancy, Appl. Catal. B 292 (2021) 120147.

[44] M. Tahir, N. Aishah, S. Amin, Indium-doped $TiO_2$ nanoparticles for photocatalytic $CO_2$ reduction with $H_2O$ vapors to $CH_4$, Appl. Catal. B 162 (2015) 98–109.

[45] Z. Liu, C. Menéndez, J. Shenoy, J.N. Hart, C.C. Sorrell, C. Cazorl, Strain engineering of oxide thin films for photocatalytic applications, Nano Energy 72 (2020) 104732.

[46] W.J. Chun, A. Ishikawa, H. Fujisawa, T. Takata, J.N. Kondo, M. Hara, M. Kawai, Y. Matsumoto, K. Domen, Conduction and valence band positions of $Ta_2O_5$, TaON, and $Ta_3N_5$ by UPS and electrochemical methods, J. Phys. Chem. B 107 (2003) 1798–1803.

[47] Y. Hermans, S. Murcia-López, A. Klein, R. van de Krol, T. Andreu, J.R. Morante, T. Toupance, W. Jaegermann, Analysis of the interfacial characteristics of $BiVO_4$/metal oxide heterostructures and its implication on their junction properties, Phys. Chem. Chem. Phys. 21 (2019) 5086–5096.

[48] H.L. Tan, X. Wen, R. Amal, Y.H. Ng, $BiVO_4$ {010} and {110} relative exposure extent: governing factor of surface charge population and photocatalytic activity, J. Phys. Chem. Lett. 7 (2016) 1400–1405.

[49] M.C. Wu, C.H. Chen, W.K. Huang, K.C. Hsiao, T.H. Lin, S.H. Chan, P.Y. Wu, C.F. Lu, Y.H. Chang, T.F. Lin, K.H. Hsu, J.F. Hsu, K.M. Lee, J.J. Shyue, K. Kordás, W.F. Su,

Improved solar-driven photocatalytic performance of highly crystalline hydrogenated $TiO_2$ nanofibers with core-shell structure, Sci. Rep. 7 (2017) 40896.

[50] I. Nakamura, N. Negishi, S. Kutsuna, T. Ihara, S. Sugihara, K.J. Takeuchi, Role of oxygen vacancy in the plasma-treated $TiO_2$ photocatalyst with visible light activity for NO removal, J. Mol. Catal. A 161 (2000) 205–212.

[51] J. Li, M. Zhang, Z. Guan, Q. Li, C. He, J. Yang, Synergistic effect of surface and bulk single-electron-trapped oxygen vacancy of $TiO_2$ in the photocatalytic reduction of $CO_2$, Appl. Catal. B 206 (2017) 300–307.

[52] Z.F. Huang, L. Pan, J.J. Zou, X. Zhang, L. Wang, Nanostructured bismuth vanadate-based materials for solar-energy-driven water oxidation: a review on recent progress, Nanoscale 6 (2014) 14044–14063.

[53] F.S. Hegner, D. Forrer, J.R. Galán-Mascarós, N. López, A. Selloni, Versatile nature of oxygen vacancies in bismuth vanadate bulk and (001) surface, J. Phys. Chem. Lett. 10 (2019) 6672–6678.

[54] K. Li, B. Peng, T. Peng, Recent advances in heterogeneous photocatalytic $CO_2$ conversion to solar fuels, ACS Catal. 6 (2016) 7485–7527.

[55] D.K. Lee, K.S. Choi, Enhancing long-term photostability of $BiVO_4$ photoanodes for solar water splitting by tuning electrolyte composition, Nat. Energy 3 (2018) 53-60.

[56] F.M. Toma, J.K. Cooper, V. Kunzelmann, M.T. McDowell, J. Yu, D.M. Larson, N.J. Borys, C. Abelyan, J.W. Beeman, K.M. Yu, J. Yang, L. Chen, M.R. Shaner, J. Spurgeon, F.A. Houle, K.A. Persson, I.D. Sharp, Mechanistic insights into chemical and photochemical transformations of bismuth vanadate photoanodes, Nat. Commun. 7 (2016) 12012.

[57] Z. Miao, G. Wang, X. Zhang, X. Dong, Oxygen vacancies modified $TiO_2/Ti_3C_2$ derived from MXenes for enhanced photocatalytic degradation of organic pollutants: the crucial role of oxygen vacancy to schottky junction, Appl. Surf. Sci. 528 (2020) 146929.

[58] X. Liang, G. Wang, X. Dong, G. Wang, H. Ma, X. Zhang, Graphitic carbon nitride with carbon vacancies for photocatalytic degradation of bisphenol A, ACS Appl. Nano Mater. 2 (2019) 517–524.

[59] G. Wang, Y. Zhao, H. Ma, C. Zhang, X. Dong, X. Zhang, Enhanced peroxymonosulfate activation on dual active sites of N vacancy modified g-$C_3N_4$ under visible-light assistance and its selective removal of organic pollutants, Sci. Total Environ. 756 (2021) 144139.

[60] G. Silversmit, D. Depla, H. Poelman, G.B. Marin, R. De Gryse, Determination of the V2p XPS binding energies for different vanadium oxidation states ($V^{5+}$ to $V^{0+}$), J. Electron Spectrosc. Relat. Phenom. 135 (2004) 167–175.

[61] Y. Park, K. J. McDonald and K. S. Choi, Progress in bismuth vanadate photoanodes for use in solar water oxidation, Chem. Soc. Rev. 42 (2013) 2321–2337.

[62] Y. Zhang, Y. Guo, H. Duan, H. Li, C. Sun, H. Liu, Facile synthesis of $V^{4+}$ self-doped, [010] oriented $BiVO_4$ nanorods with highly efficient visible light-induced photocatalytic activity, Phys. Chem. Chem. Phys. 16 (2014) 24519–24526.

[63] S. Akrami, P. Edalati, M. Fuji, K. Edalati, High-entropy ceramics: review of principles, production and applications, Mater. Sci. Eng. R 146 (2021) 100644.

# Chapter 3. High-pressure $TiO_2$-II polymorph as an active photocatalyst for $CO_2$ to CO conversion

## 3.1. Introduction

$TiO_2$ has three main polymorphs under ambient conditions (rutile and anatase with the tetragonal crystal structure and brookite with the orthorhombic crystal structure) [1], and among them, the anatase phase shows the highest photocatalytic activity due to its high electron effective mass and large specific surface area [2]. However, the large bandgap of anatase (3.0-3.2 eV) and its limited activity (due to short lifetime of charge carriers) have led to numerous studies to narrow its optical bandgap and improve its photocatalytic activity. The main focus of these studies is the addition of a third element or dopants to $TiO_2$ such as nitrogen [3], sulfur [4], iodine [5], fluorine [6], nickel [7], chromium [7], vanadium [7], cobalt [7], coper [8], silver [9] and gold [10]. Although addition of a third element to $TiO_2$ is an effective technique to reduce the bandgap, the method may not enhance the photocatalytic activity significantly due to the impurity-induced recombination effects [11]. Therefore, there are new trends to improve the photocatalytic $CO_2$ conversion on pure $TiO_2$ by nanostructure and polymorphic control and without addition of impurity elements [12-15].

In this study, to improve the photocatalytic $CO_2$ conversion on $TiO_2$ by nanostructure control and without addition of any impurity elements, the high-pressure columbite ($TiO_2$-II) phase with the orthorhombic crystal structure is introduced in $TiO_2$ (see the pressure-temperature phase diagram of $TiO_2$ in Fig. 3.1a [1]). A high-pressure torsion (HPT) method [16], as schematically shown in Fig. 3.1b, is used to stabilize the $TiO_2$-II phase because earlier studies confirmed the high capability of this method for controlling the polymorphic phase transformation in various oxides [17,18] including those with photocatalytic properties such as $TiO_2$ [19], ZnO [20] and $ZrO_2$ [21]. This first application of high-pressure $TiO_2$-II phase for photocatalytic $CO_2$ conversion confirms its higher activity compared with the pure anatase phase.

## 3.2. Experimental section

### *3.2.1. Sample preparation*

About 250 mg of $TiO_2$ anatase powder (Sigma Aldrich) with the purity level of 99.8% (impurities in mass ppm: 0.3 Be, 23.3 Na, 14.7 Mg, 116.6 Al, 1773.1 K, 26.0 Ca, 12.1 V, 0.6 Mn, 19.7 Fe, 2.7 Zn, 0.4 Sr, 144.8 Zr, 20.0 Pd, 18.7 Sn, 5.8 Ba, 13.0 Pt, 10.2 Pb, 22.9 Bi) and 50-250 nm particle sizes was compacted in the form of 10 mm disc under a pressure of 380 MPa. The compacted disc was then pressurized between two HPT anvils under a pressure of 6 GPa at ambient temperature ($T$ = 300 K) and concurrently strained by rotating the two anvils with respect to each other for $N$ = 3 turns with a rotation speed of 1 rpm (see the principles of HPT in [16,17]). Since the HPT method can generate oxygen vacancies in oxides [18,19], the HPT-processed samples were annealed in the air atmosphere at 773 K for 1 h to minimize the effect of oxygen vacancies on photocatalytic $CO_2$ conversion. The initial powder, the sample after HPT processing and the sample after annealing were crushed, as shown in Fig. 3.1c, and examined in detail using different techniques, as described below.

### *3.2.2. Characterization*

The specific surface area of the crushed samples was examined by nitrogen gas adsorption using the Brunauer-Emmett-Teller (BET) technique. The estimated surface areas were 10.2, 6.2 and 6.8 $m^2/g$ and no porosities were detected within the detection limits of the BET method.

X-ray diffraction (XRD) using the Cu Kα radiation with a wavelength of $\lambda$ = 0.1542 nm and Raman spectroscopy using a 532-nm laser source were utilized to investigate the crystal structures and phase transformations. The XRD profiles were evaluated by the Rietveld method using the FullProf Suite software and by refining the profiles using the Gaussian and Lorentzian functions ("Thompson-Cox-Hastings pseudo-Voigt" function) [22]. The average lattice strain was determined from the width of Gaussian function $H_G(\Delta 2\theta)$, and the average crystallite size ($D$) was determined from the width of Lorentzian function $H_L(\Delta 2\theta)$, using the following relationships ($\theta$: Bragg angle) [23,24].

$$D = \frac{2\lambda}{\pi\, H_L(\Delta 2\theta)\cos\theta} \tag{3.1}$$

$$\varepsilon = \frac{H_G(\Delta 2\theta)}{8\sqrt{\ln 2/\pi}\,\tan\theta} \tag{3.2}$$

Transmission electron microscopy (TEM) in the bright-field (BF) mode, dark-field (DF) mode, selected area electron diffraction (SAED) and high-resolution imaging combined with fast Fourier transform (FFT) was performed to clarify the micro/nanostructural features of phases. For TEM, the samples were crushed in ethanol and dispersed on carbon grids and examined by an aberration-corrected microscope in an acceleration voltage of 200 kV.

Electron paramagnetic resonance (EPR) was conducted at ambient temperature using a 9.4688 GHz microwave source to study the electron spins and evaluate the presence of oxygen vacancies and formation of $Ti^{3+}$ states.

X-ray photoelectron spectroscopy (XPS) was conducted using a Mg $K_\alpha$ source to investigate the electronic states of different elements, examine the formation of oxygen vacancies and estimate the bottom of valence band.

Ultraviolet-visible (UV-vis) diffuse reflectance spectroscopy was performed to investigate the light absorbance of samples and calculate the bandgap using the Kubelka-Munk analysis. A combination of UV-vis spectroscopy and XPS was used to determine the band structure of samples.

The steady-state photoluminescence (PL) emission spectroscopy with a 325-nm laser source and time-resolved photoluminescence decay (PL decay) with a 285-nm laser source were used to investigate the recombination of electrons and holes and decay time of exited electrons.

Attenuated total reflectance - Fourier transform infrared spectroscopy (ATR-FTIR) was conducted at room temperature using a Jasco FT/IR-610 device.

Temperature-programmed desorption (TPD) was conducted using a commercial Micotrac Bel instrument equipped with a quadrupole mass spectrometric detector and thermal conductivity detector. For TPD, 30 mg of samples were first placed in pure (99.99%) $CO_2$ with a gas flow rate of 100 mL/min under 0.1 MPa at 323 K or 773 K for 2 h. After evacuation with a vacuum pump at 323 K for 15 min, the samples were then heated from 323 K to 773 K with a heating rate of 5 K/min and the TPD signals were recorded.

#### *3.2.3. Photocurrent test*

Photocurrent experiment was performed using a Xe lamp in 1 M $Na_2SO_4$ electrolyte to investigate the photoactivity. In these tests, thin film of $TiO_2$ sample on FTO (fluorine-doped tin oxide) glass, Pt wire and Ag/AgCl were used as working, counter and reference electrodes, respectively. An electrochemical analyzer was utilized to investigate the photocurrent generation

by potentiostatic amperometry during time (30 s light ON and 60 s light OFF). For making the thin films, 5 mg of samples were crushed in 0.2 mL ethanol and uniformly dispersed on 0.1-mm thick FTO glass with 15×25 $mm^2$ surface area and baked in furnace at 473 K for 1 h.

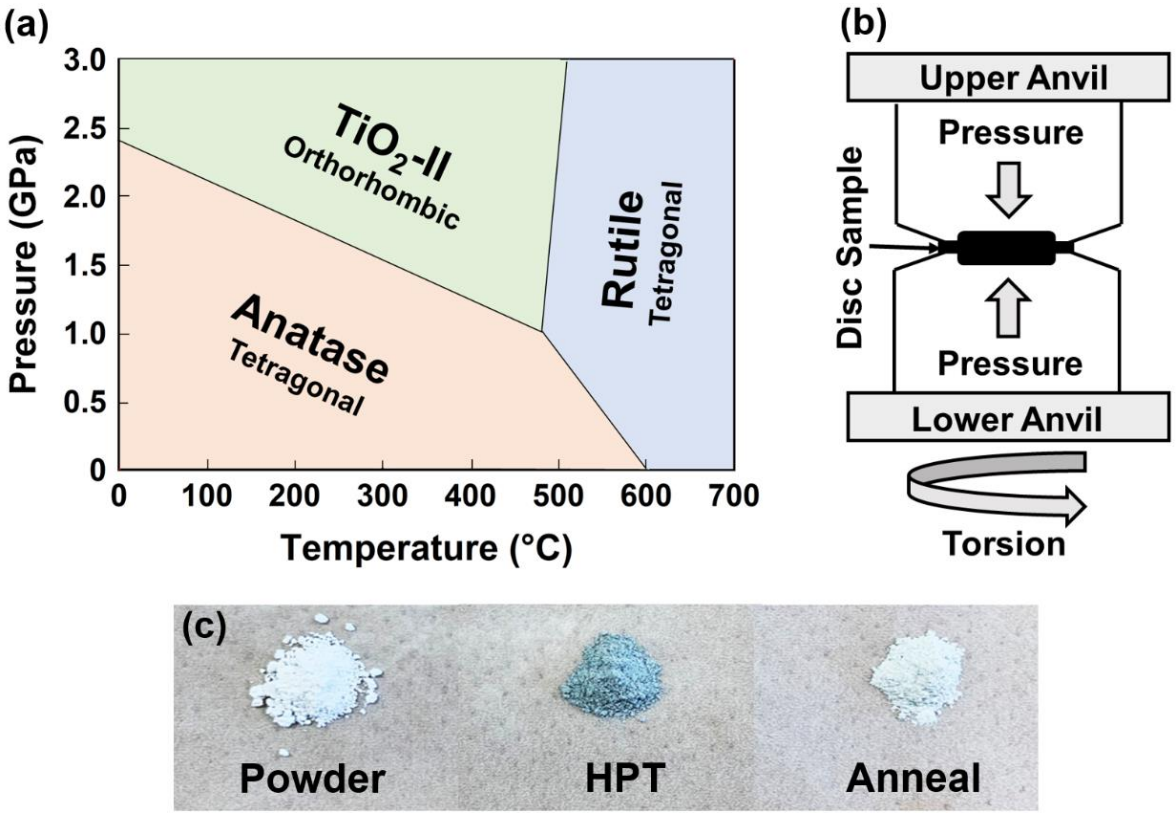


Fig. 3.1. (a) Pressure-temperature phase diagram of $TiO_2$, (b) schematic of high-pressure torsion (HPT) process and (c) appearance of three samples before HPT, after HPT and after annealing.

### *3.2.4. Photocatalytic test*

For photocatalytic $CO_2$ conversion, 100 mg of samples were dispersed in 30 mL solution of 1 M $NaHCO_3$ in a $CO_2$ flow reactor system, and after bubbling with $CO_2$ (3mL/min) in dark for 1 h, irradiated with a 300 W Hg-Xe light source (Newport, Arc Lamp Housing 66905, 300 W), as schematically shown in Fig. 3.2a. The photoreactor, as shown in Fig. 3.2a, was made from quartz, and had a cuboid shape with a total volume of 105 mL (30x50x70 $mm^3$ internal dimensions with a quartz thickness of 10 mm). The reactor had three holes on top for $CO_2$ gas inflow and outflow and for sampling the atmosphere of reactor for chemical analysis. The light intensity on the

photocatalysts was 0.63 W/cm$^2$ and the spectral composition of light source, examined with Hamamatsu Photonics PMA-11, is shown in Fig. 3.2b. The gas phase was analyzed using a gas chromatograph (Shimadzu GC-8A). The CO and $CH_4$ production were evaluated using a flame ionization detector equipped with a methanizer (Shimadzu MTN-1) and $H_2$ and $O_2$ production were evaluated using a thermal conductivity detector. Here, it should be noted although some systematic studies suggested an optimum $TiO_2$ concentration of 1 g/L for photocatalytic reactors [25], a higher concentration of 3.3 g/L was used in this study due to the low specific surface area of HPT-processed samples.

## 3.3. Results and discussion

### *3.3.1. $TiO_2$-II phase formations*

Examination of phase transformations using the XRD profiles and Raman spectra are shown in Figs. 3.3a and 3b, respectively. As shown in Fig. 3.3a, the initial powder contains the anatase phase, while new peaks corresponding to the $TiO_2$-II phase appear after HPT processing. The $TiO_2$-II peaks remain in the XRD profile after annealing and some other peaks corresponding to the rutile phase appear. Quantitative analysis of phase fractions using the Rietveld method, as given in Table 3.2, confirms the high stability of $TiO_2$-II phase even after annealing at 773 K. The Raman spectra also confirms that the initial powder mainly contains an anatase phase, while a $TiO_2$-II phase is formed after HPT processing (see the peaks at wavenumber of 171, 283, 316, 340, 357, 428, 533 and 572 cm$^{-1}$). A rutile phase is also formed after HPT processing and the intensity of its peaks increases after annealing. These results are reasonably consistent with the reported effect of pressure on $TiO_2$-II phase formation and the temperature effect on the formation of rutile phase, as shown in Fig. 3.1a [1]. However, the stability of $TiO_2$-II phase at ambient pressure and the formation of rutile phase at relatively low temperature compared to the phase diagram should be due to the effect of straining by HPT, as discussed in earlier publications [26].

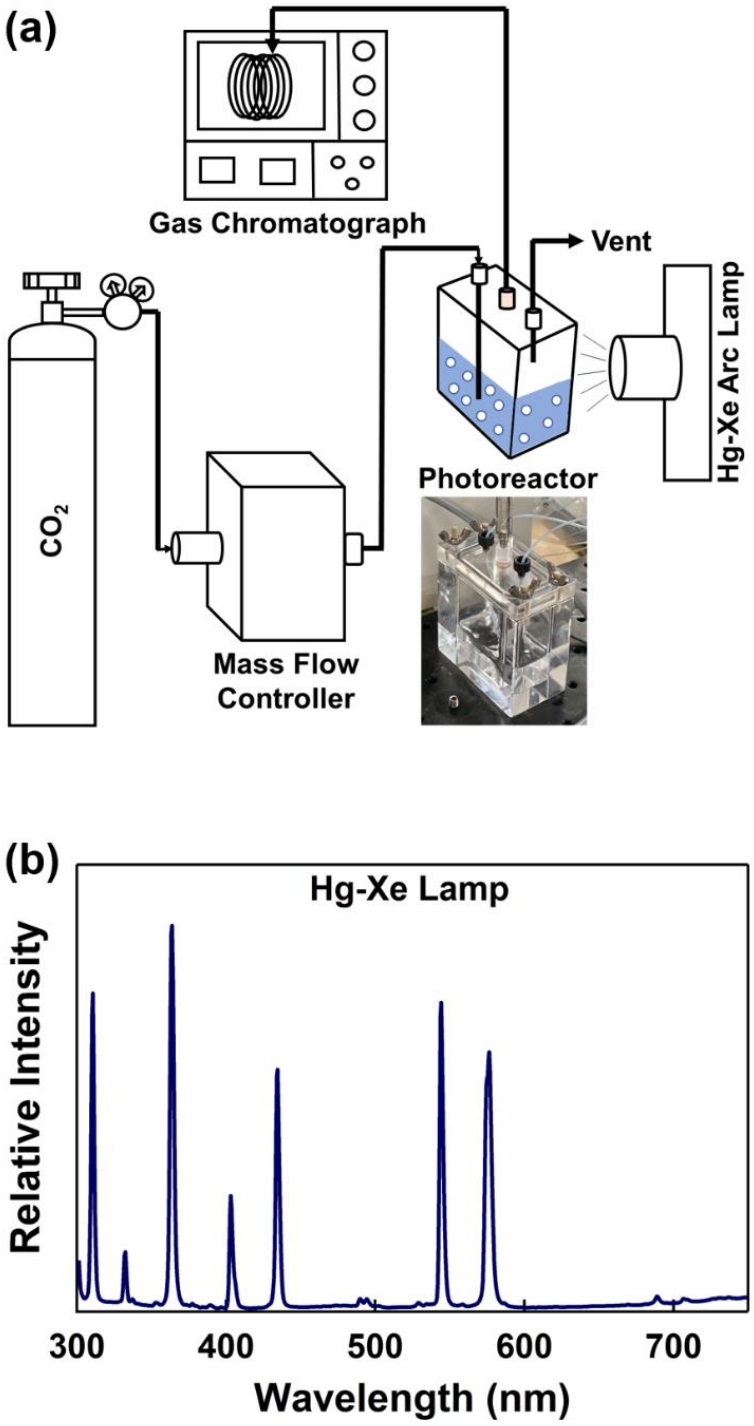


Fig. 3.2. (a) Schematic illustration of photocatalytic $CO_2$ conversion system and photo of its photoreactor, and (b) spectral composition of He-Xe lamp used for photocatalytic test.

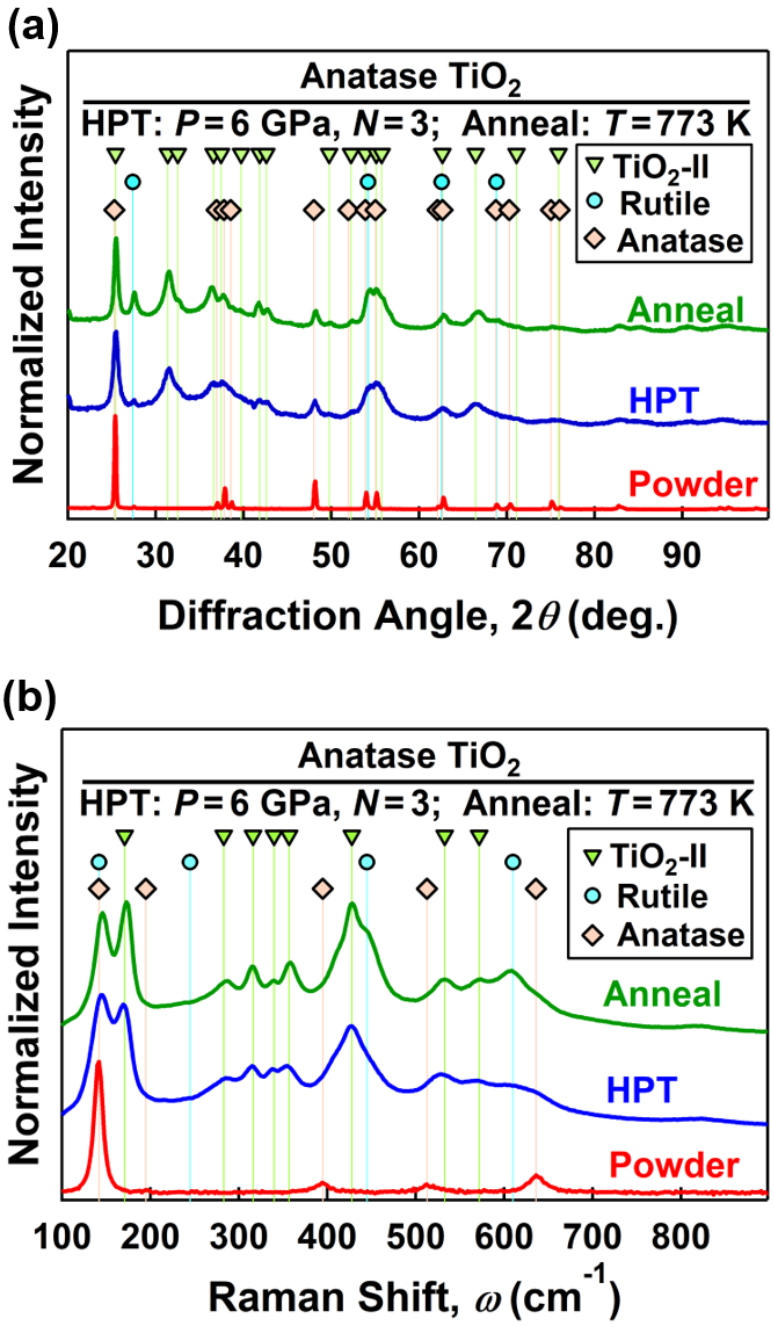


Fig. 3.3. Formation of $TiO_2$-II phase after HPT processing and its stability during annealing. (a) XRD profiles and (b) Raman spectra for initial powder and for samples processed by HPT and annealing.

Table 3.2. Fraction of anatase, $TiO_2$-II and rutile phases, average lattice strain and average crystallite size determined from XRD profiles, and mean grain size measured by TEM for initial powder and for samples processed by HPT and annealing.

| Sample | Phase Fractions (wt%) | | | Lattice Strain | Crystallite Size | Grain Size |
|---|---|---|---|---|---|---|
| | Rutile | Anatase | $TiO_2$-II | (%) | (nm) | (nm) |
| Powder | 2.7 | 97.3 | 0 | 0.1 | 60 | 130 ± 40 |
| HPT | 11.8 | 27.5 | 60.7 | 0.8 | 9 | 32 ± 16 |
| Anneal | 23.2 | 20.0 | 56.8 | 0.5 | 11 | 43 ± 22 |

***3.3.2. Microstructure of catalysts***

Microstructural features examined using TEM BF and DF images and corresponding SAED patterns are shown in Fig. 3.4 for (a-c) initial powder, (d-f) sample processed by HPT and (g-i) samples processed by annealing, where DF images were taken with the diffracted beams indicated by arrows in the SAED patterns. The initial sample has an average particle size of 130 nm and most of the particles contain only one crystal. After HPT processing, the particle sizes become larger due to HPT-induced partial consolidation [18], but the grain sizes (white regions in the DF images) are refined to the range of nanometer due to the effect of severe strain [16,17]. The grain sizes remain at the range of nanometer even after annealing at 773 K and many crystals still exist in one particle. The ring shapes of the SAED patterns for the samples processed by HPT and annealing in comparison with the net shape of the SAED pattern for the initial powder also confirms smaller crystal sizes in these two samples. For the three samples, Table 3.2 gives the mean grain sizes measured by TEM, average crystallite sizes determined by XRD and the average lattice strain determined by XRD. The grain/crystallite size decreases and the lattice strain increases by HPT processing, while the grain/crystallite size slightly increases and the lattice strain increases by subsequent annealing.

To examine the nanostructural features, high-resolution TEM was performed as shown in Fig. 3.5 for (a, b) initial powder, (c, d) sample processed by HPT and (e, f) sample processed by annealing. The initial powder contains large crystals of anatase phase which was confirmed by FFT analyses. After HPT processing, many nanocrystals with the $TiO_2$-II structure are visible, while some small amount of the rutile phase is also detectable. The nanostructural changes after

annealing are not so significant and many nanocrystalline with the $TiO_2$-II phase are still visible within the microstructure. In addition to nanograins, many $TiO_2$-II/anatase phase boundaries are formed by HPT processing. These results are consistent with the phase analyses in Fig. 3.3, microstructural analysis in Fig. 3.4 and reported data about the effect of strain on the microstructural evolution of various oxides [17-21].

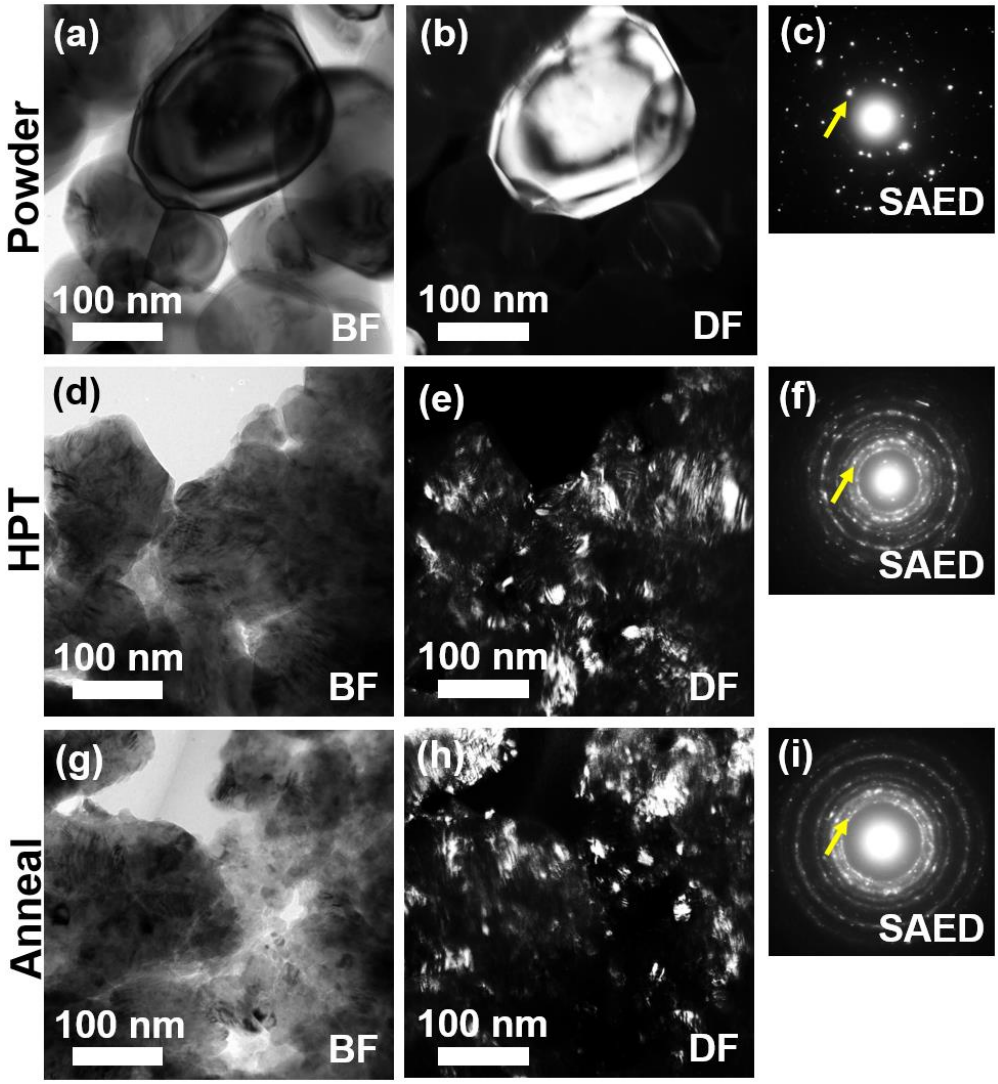


Fig. 3.4. Reduction of crystal size after HPT processing and stability of nanocrystals during annealing. TEM BF images, DF images and SAED patters for (a-c) initial powder, (d-f) HPT-processed sample and (g-i) annealed sample.

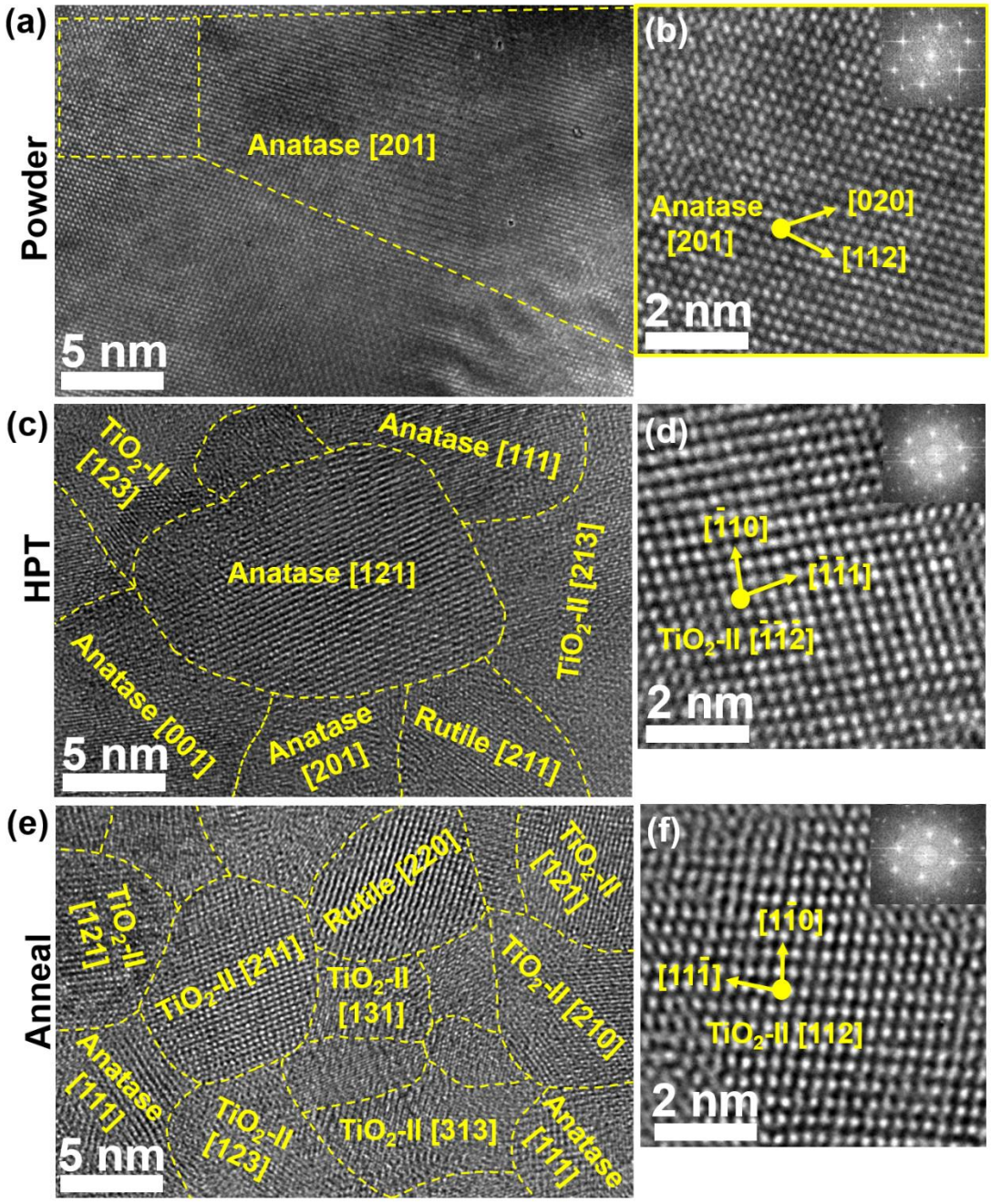


Fig. 3.5. Co-existence of nanocrystalline $TiO_2$-II phase with anatase and rutile phases after HPT processing and annealing. TEM (a, c, e) high-resolution images and (b, d, f) lattice images and corresponding FFT diffractograms for (a, b) initial powder, (c, d) HPT-processed sample and (e, f) annealed sample.

### *3.3.3. Vacancy formation/annihilation*

The appearance of three samples is shown in Fig. 3.1c. The initial anatase powder has a white color, but its color becomes dark green after HPT processing, indicating the formation of color centers such as oxygen vacancies in the sample [20,21]. The color of samples becomes almost white after annealing, indicating that many color centers are thermally annihilated. The formation of oxygen vacancies was examined by XPS, as shown in Fig. 3.6 for (a) O 1s and (b) Ti 2p.

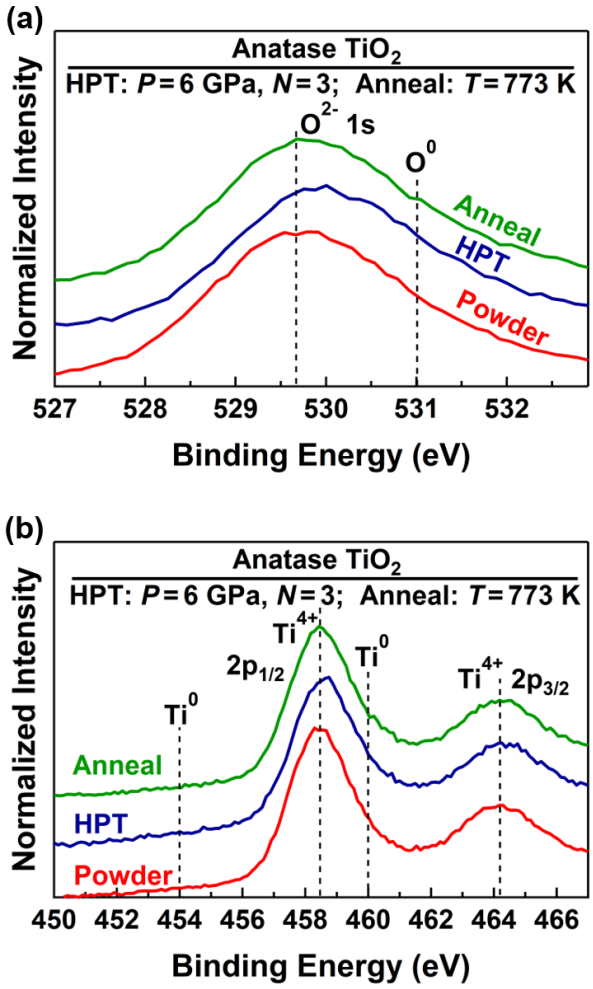


Fig. 3.6. Formation of oxygen vacancies by HPT processing and their annihilation after annealing. XPS profiles with (a) O 1s and (b) Ti 2p for initial powder and for samples processed by HPT and annealing.

Note that the XPS peak positions were corrected by considering the C 1s peak position at 284.8 eV. Figs. 3.6a and 5b demonstrate the presence of oxygen anion and titanium cations in all samples, but the main difference is that the O 1s peak shifts slightly to higher energies after HPT processing and return to its original position after annealing (Ti 2p peaks do not show clear changes). These shifts, which are consistent with the changes in the color of samples, are probably due to the formation and annihilation of oxygen vacancies after HPT processing and annealing, respectively. The formation of vacancies by HPT processing is a consequence of strain effect on microstructure which was reported in various metallic and ceramic materials [16-18].

The nature of oxygen vacancies was examined by EPR, as shown in Fig. 3.7. The initial powder contains various characteristic peaks of the anatase phase [27]. After HPT processing, characteristic peaks of anatase disappear and several pair peaks appear which corresponds to different defects: the one with a *g* value higher than 2 (i.e., inflection point at 2.004) is related to hole trapping sites such as oxygen-centered radicals or oxygen vacancies, and those with the *g* values smaller than 2 (i.e., inflection points at 1.991 and 1.984) are related to electron trapping sites such as $Ti^{3+}$ radicals in the bulk [27-29]. Since the $Ti^{3+}$ sites in the bulk are considered as recombination sites [30], their presence is not appropriate for photocatalytic activity [31,32]. After annealing, the peak pairs corresponding to the $Ti^{3+}$ radicals disappear, while the oxygen vacancy peak is still visible. It should be noted that the presence of oxygen vacancies on the surface with an optimum concentration is positive for photocatalytic activity because they can act as active sites for reaction, but their presence in the bulk can enhance the electron-hole recombination and destroy the photocatalytic activity [30].

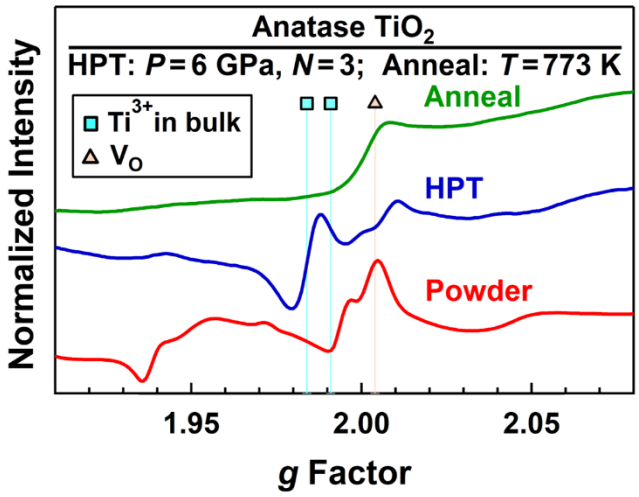


Fig. 3.7. Formation of $Ti^{3+}$ radicals and oxygen vacancies ($V_O$) by HPT processing and disappearance of $Ti^{3+}$ radicals in bulk by annealing. EPR spectra for initial powder and for samples processed by HPT and annealing.

### *3.3.4. Light absorbance and band structure*

The light absorbance and band structure of samples were examined by UV-vis spectroscopy and XPS and compared with the energy requirements for the photocatalytic $CO_2$ conversion. UV-vis spectra are shown in Fig. 3.8a, indicating that the three samples mainly absorb the UV light. The light absorbance in the visible light region increases by HPT processing and decreases after annealing. Fig. 3.8b shows the bandgap calculation using the Kubelka-Munk theory. The bandgap of initial powder is 3.0 eV and it decreases to 2.5 eV after HPT processing and reaches 2.7 eV after annealing. The estimated bandgap for the HPT-processed sample is close to the reported theoretical bandgap of $TiO_2$-II [33,34]. Therefore, the formation of $TiO_2$-II phase and oxygen vacancies should have led to higher light absorbance and narrowing the optical bandgap. Increasing the bandgap after annealing should be due to the annihilation of oxygen vacancies and partial reduction of the $TiO_2$-II phase fraction. Fig. 3.8c demonstrates the XPS profiles to calculate the top of valence band. Top of valence band for the initial powder, HPT-processed sample and annealed sample are 2.2, 2.1 and 2.0 eV, respectively. From the calculated bandgaps, the bottom of conduction band can be calculated by subtraction of bandgap from the top of valence band. Fig. 3.8d summarizes the band structure of three samples. All samples satisfy the energy requirement for $CO_2$ conversion [35,36]. Higher level of conduction band in the annealed sample compared

with the HPT-processed sample suggests that the annealed sample can thermodynamically be more appropriate for $CO_2$ reduction [37,38].

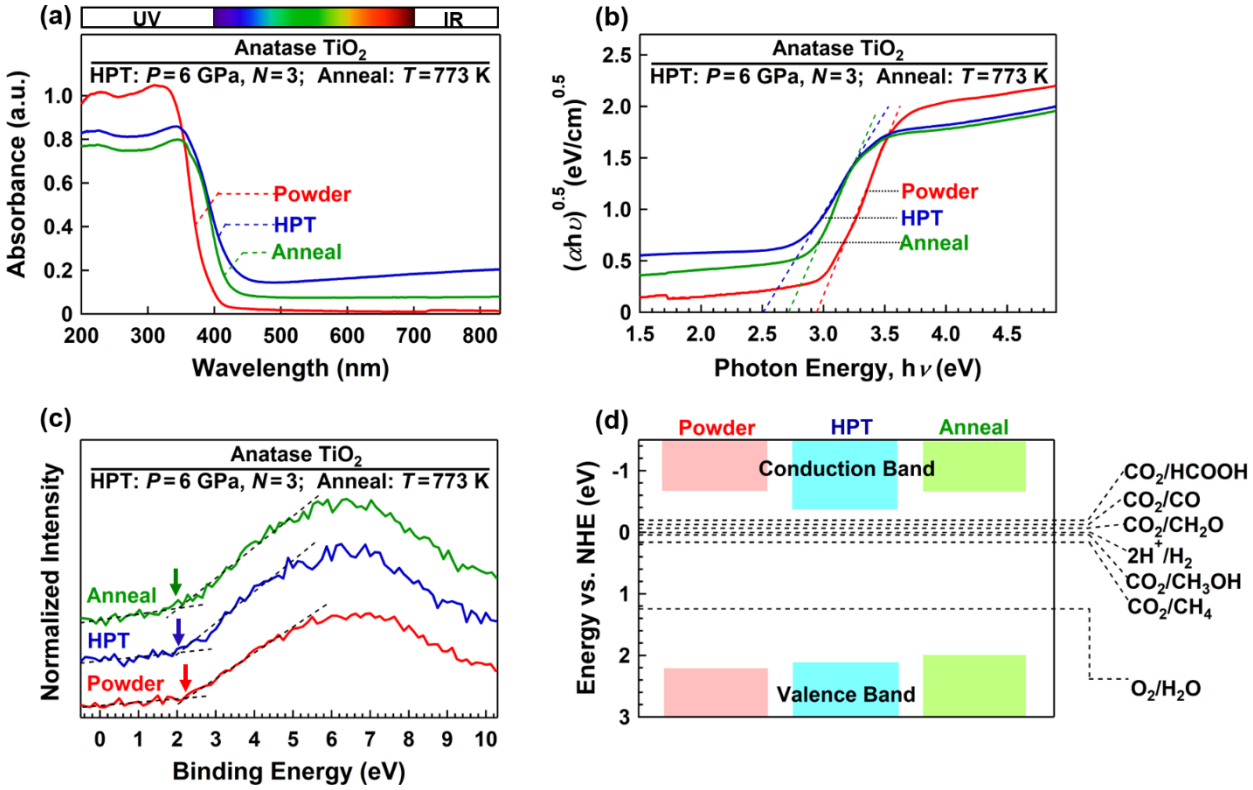


Fig. 3.8. Larger light absorbance and improvement of band structure for $CO_2$ conversion by introduction of $TiO_2$-II phase. (a) UV-vis spectra, (b) bandgap calculation using Kubelka-Munk analysis ($\alpha$: light absorption, h: Planck's constant, $v$: photon frequency), (c) XPS of top of valence band and (d) band structure compared to energy requirements for $CO_2$ conversion for initial powder and for samples processed by HPT and annealing.

### *3.3.5. Charge carrier decay and photocurrent generation*

The steady-state PL emission spectroscopy (Fig. 3.9a), PL decay spectroscopy (Fig. 3.9b) and photocurrent measurements (Fig. 3.9c) were used to examine the mobility of excited charge carriers for movement to the activation/recombination sites. The steady-state PL spectra in Fig. 3.9a shows that the PL intensity for the HPT-processed and annealed samples is significantly lower than that for the anatase powder. This suggests that the recombination of electrons and holes is suppressed in these two samples. Three PL peaks are detectable in Fig. 3.9a at three wavelengths:

~420 nm corresponding to the band-to-band transition [39], ~510 nm corresponding to surface oxygen vacancies or shallow bulk traps in anatase [40], and ~830 nm (mainly in the annealed sample) corresponding to the deep traps in rutile [41].

The PL decay intensity versus time, $I(t)$, exhibits a two-exponential kinetic function in Fig. 3.9a [42].

$$I(t) = A_1 \exp\left(-\frac{t}{\tau_1}\right) + A_2 \exp\left(-\frac{t}{\tau_2}\right) \quad (3.3)$$

In this equation, $A_1$ and $A_2$ are the amplitude of each exponential function and $\tau_1$ and $\tau_2$ are the fast decay time and the slow decay time, respectively. As summarized in Table 3.3, the decay times decrease by HPT processing and decrease further by annealing. Here it should be noted that the decay time estimation of $TiO_2$ by PL decay spectroscopy can be influenced by both radiative and non-radiative recombination [43]. For the HPT-processed and annealed samples with surface defects as shallow traps or photocatalytic activation sites, the fast movement of charge carriers results in fast decay time [44-46]. The hetero-phase junctions such as anatase/rutile or anatase/$TiO_2$-II can also transfer the electron to the surface defects and reduce the decay time [47]. In contrast, the bulk defects which are formed by HPT processing and disappear by annealing can act as recombination centers and lead to a decrease in the lifetime and a decrease in the photocatalytic activity [48,49]. Decreasing the decay time by HPT processing and annealing also indicate that the change of the electronic structure between the ground state and the excited state decreases under light irradiation. This phenomenon can lead to decreasing the re-organization energy and improving the photocatalytic activity.

Photocurrent measurements, as shown in Fig. 3.9b, show that the current density for initial powder is smaller than the HPT-processed and annealed samples and the current density for the annealed sample is somehow higher than that for the HPT-processed sample. The reason for higher photocurrent density of annealed and HPT-processed samples can be due to lower bandgap, the presence of $TiO_2$-II/anatase heterojunctions which can ease the separation of electrons from the valence band, and the presence of vacancies as shallow traps [26]. Better photocurrent for the annealed sample should be due to the thermal annihilation of bulk vacancies as recombination sites [26]. The high photocurrent density shows the efficient charge separation which can contribute to increasing the $CO_2$ conversion efficiency on the HPT-processed and annealed samples. Here it should be noted that the authors' attempt to estimate the flat-band potential and carrier density

using the Mott-Schottky method [50] was not successful due to the technical limits in making uniform films with perfect FTO/$TiO_2$ and $TiO_2$/$TiO_2$ connections.

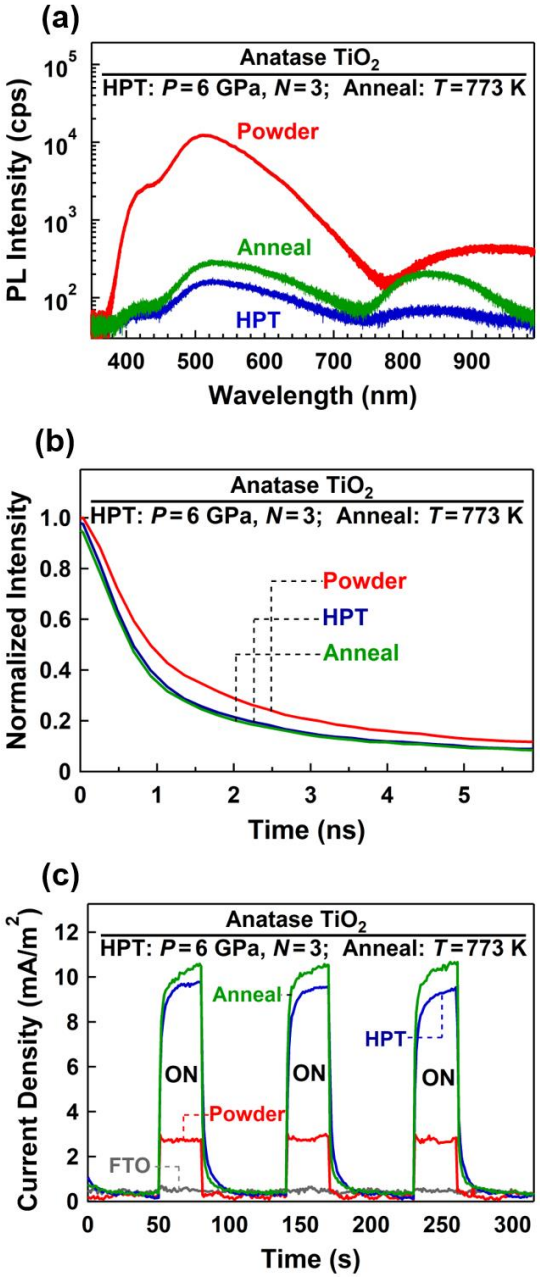


Fig. 3.9. Suppression of recombination and enhancement of charge carrier mobility by HPT processing and annealing. (a) Steady-state photoluminescence emission spectra, (b) time-resolved photoluminescence decay spectra and (c) photocurrent density against time for initial powder and for samples processed by HPT and annealing. ON in (c) indicates application of UV light irradiation.

Table 3.3. Decreasing decay time by HPT processing and subsequent annealing. Fitted parameters of PL decay spectra for initial powder and for samples processed by HPT and annealing.

| Samples | $\tau_1$ (ns) | $\tau_2$ (ns) | $A_1$ | $A_2$ |
|---|---|---|---|---|
| Powder | 1.24 | 11.46 | 41.98 | 58.02 |
| HPT | 0.95 | 11.40 | 40.23 | 59.77 |
| Anneal | 0.93 | 10.97 | 39.65 | 60.35 |

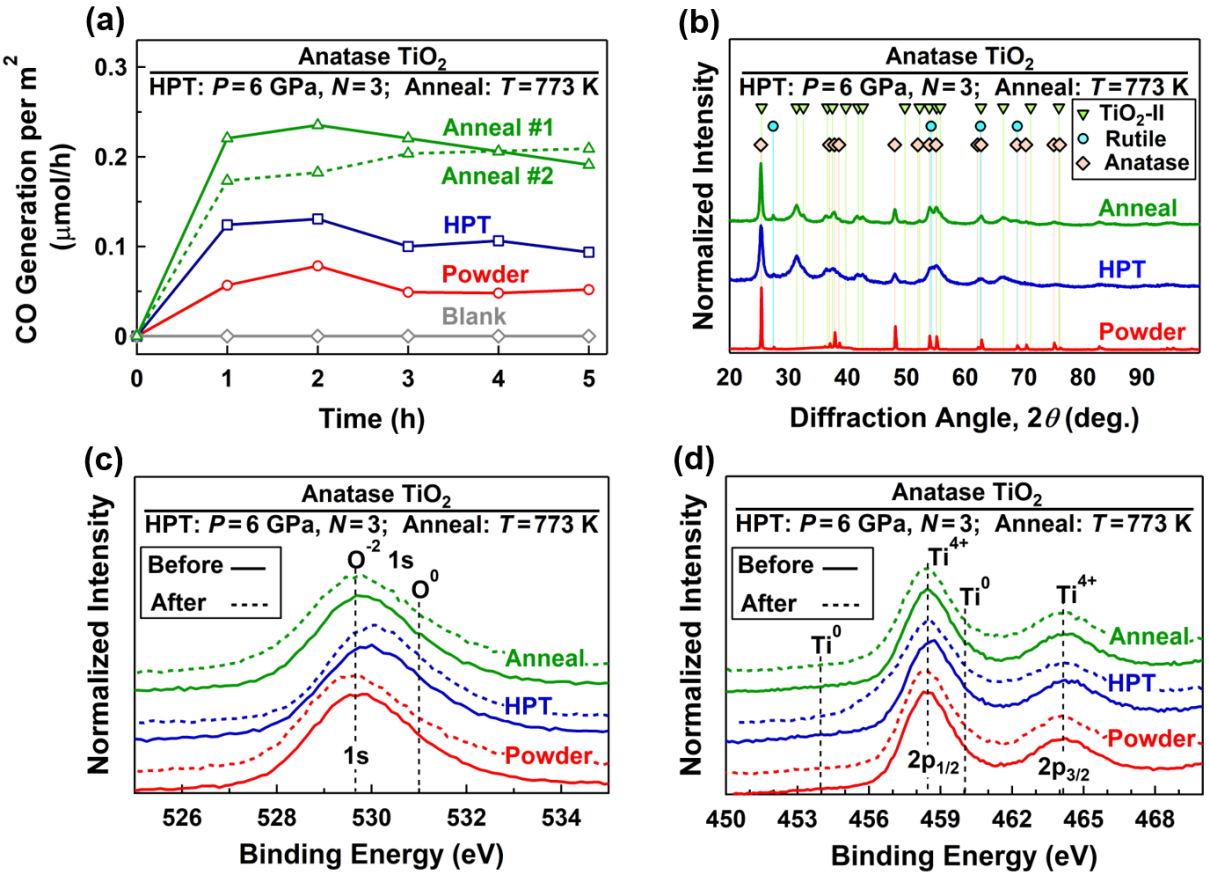


Fig. 3.10. Enhancement of photocatalytic $CO_2$ conversion by introduction of $TiO_2$-II phase via HPT processing and further activity enhancement by removing vacancies from bulk via annealing. (a) Amount of CO produced by photocatalytic $CO_2$ conversion under UV light, (b) XRD profiles after photocatalytic tests, and XPS profiles of (c) O 1s and (d) Ti 2p before and after photocatalytic test for initial powder and for samples processed by HPT and annealing.

### *3.3.6. Photocatalytic $CO_2$ conversion*

The activity of samples under UV light was examined by photocatalytic $CO_2$ conversion, as attempted in earlier studies [2,35,36,51-54]. As shown in Fig. 3.10a, all samples convert $CO_2$ to CO without addition of a co-catalyst, and similar to photocurrent measurements, the efficiency of annealed sample is higher than the two other samples (the standard deviation of gas chromatography for three different tests was less than 10%). Independent synthesis of the annealed sample (as the most active catalyst) and repeating the photocatalytic test, as shown as Anneal #2 in Fig. 3.10a, also confirm a reasonable reproducibility of the synthesis method and CO generation. Examination of gas and liquid phases by gas chromatography and nuclear magnetic resonance suggests that CO is the only product of photoreaction within the detection limits of the measurement system. Blank test by illumination of solution and without the addition of catalysts does not lead to the production of CO, as shown in Fig. 3.10a. Moreover, none of the samples show CO generation after 1 h process in dark (i.e. the data points at the time of 0 in Fig. 3.10a). It is worth mentioning that the authors' earlier attempts for water splitting using these samples under UV light resulted in no $H_2$ or $O_2$ generation without addition of a co-catalyst and sacrificial agent.

Examination of the stability of catalysts by XRD after photocatalytic test, as shown in Fig. 3.10b, confirms that the bulk of all samples remains stable during the photocatalytic test. Moreover, XPS analysis before and after photocatalytic test, as shown in Fig. 10c for O 1s and in Fig. 3.10d for Ti 2p, confirms that the surface of samples also remains stable after photocatalytic test. Although the recyclability of these three samples were not examined in detail in this study, an annealed sample used for achieving the photocatalytic data of Annealed #1 in Fig. 3.10a, was reused for photocatalysis after 10-month storage in air atmosphere. Its CO production rate per surface area was determined as 0.15 μmol/h within 1 h which is 30% lower than the activity of the sample in the first cycle. Although this experiment suggests that the sample was deactivated after recycling, but its CO production rate is still better than the activity of anatase powder. Taken altogether, the current results confirm the significance of $TiO_2$-II phase for photocatalytic $CO_2$ conversion, although the quantum yield analysis should be conducted in future to quantify its yield efficiency compared to other photocatalysts [55].

To understand the binding mode of $CO_2$ with the surface of photocatalysts, the ATR-FTIR spectroscopy was conducted before and after immersion of the samples in 1 M $NaHCO_3$. Fig. 3.11a shows the difference between the intensity of ATR-FTIR spectra before and after immersion. For

the three samples, a peak appears at wavenumbers of 2300-2400 $cm^{-1}$ and the main difference is the higher intensity of peak for the annealed sample compared to the two other samples. Such peaks are typical of $CO_2$ in air or physiosorbed $CO_2$ on the surface of oxides [56,57]. The ATR-FTIR spectra in Fig. 3.11a provide no clear evidence for carboxylate, bicarbonate, monodentate, bidentate and tridentate modes [58]. Here, it should be noted that $NaHCO_3$ was used in the photocatalytic tests of this study mainly to enhance the solubility of $CO_2$ in the solution and to enhance the basicity [59].

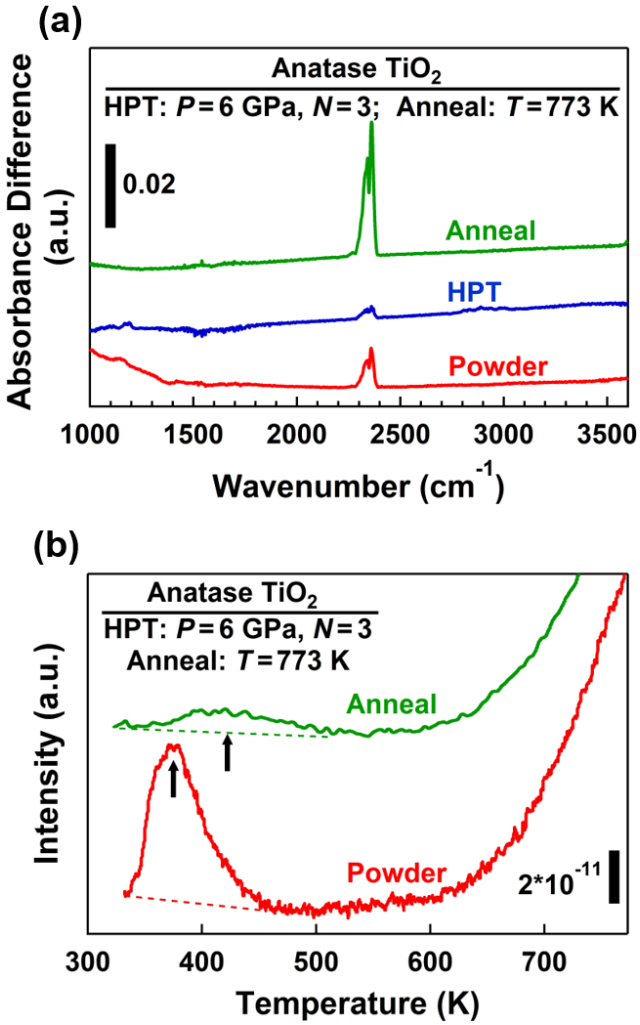


Fig. 3.11. Adsorption behavior of $CO_2$ on surface of photocatalysts. (a) Difference between ATR-FTIR spectra before and after immersion of photocatalysts in 1 M $NaHCO_3$ for initial powder and samples processed by HPT and annealing, and (b) TPD spectra after $CO_2$ adsorption at 773 K for initial powder and annealed sample.

To further investigate the adsorption of $CO_2$ to the surface of photocatalysts, TPD was conducted. None of the samples could absorb $CO_2$ at 323 K perhaps because of weak basicity of the three samples. Here, it should be noted that a main difference between the TPD tests and photocatalytic reaction is that the photocatalytic test is conducted in an aqueous solution of 1 M $NaHCO_3$, but the TPD test is conducted under gaseous atmosphere. To have an insight into the $CO_2$ adsorption on the surface of samples, the adsorption temperature was increased to 773 K. At this temperature, the initial powder and the sample annealed at 773 K are stable, but the HPT-processed sample shows structural changes and cannot be tested by TPD. Both powder and annealed samples show small amounts of hydrogen adsorption, with the desorption behaviors shown in Fig. 3.11b. The powder sample has an intense peak at low temperature, but the annealed sample reveals a low-intensity broad peak but at higher temperatures (no CO or $O_2$ desorption was detected for the samples). These TPD results suggest that the bonding of $CO_2$ to the surface of annealed sample is somehow stronger than that for the initial anatase powder, although the amount of adsorbed $CO_2$ on the surface of initial powder is higher perhaps because of its larger surface area or its higher basicity in the gaseous atmosphere.

Three main pathways for $CO_2$ photoreduction including carbene, formaldehyde and glyoxal have been suggested by in situ examinations; however, there are still significant arguments regarding the photocatalytic $CO_2$ conversion pathways on $TiO_2$ due to the effects of impurities, structure and lattice defects [60,61]. The absence of HCOOH, $CH_3OH$ and $CH_4$ in the liquid and gas phases within the detection limits of our experiments suggests that the formaldehyde may not be the main pathway for $CO_2$ photodegradation. Moreover, the absence of HCOOH and $CH_4$ in our study suggests that the glyoxal may not be the main pathway. The production of only CO suggests that the carbene can be the main pathway, although the nonappearance of $CH_4$ indicates that the carbene pathway probably stops at intermediate stages [58]. One reason for the absence of $CH_4$ can be explained by the presence of surface defects. Since the $TiO_2$ samples in this study have surface defects such as oxygen vacancies, $CO_2$ in combination with $H_2O$ as a Lewis acid desires to adsorb on oxygen vacancy sites [58]. Such adsorption can lead to degradation of C=O bonding to produce $^{\bullet}CO$ radicals and subsequently produce CO gas. Since CO is the main product and it is not willing to adsorb on the surface defects again [58], the carbene pathway at this stage does not move forward appreciably to produce detectable amount of $CH_4$. Some other studies also reported that although the formation of $CH_4$ is thermodynamically more favorable than the formation of

CO, the $CH_4$ formation is kinetically more difficult because it needs more electrons and protons [55].

### *3.3.7. Role of $TiO_2$-II and comparison with other photocatalysts*

Taken altogether, the current results on the first application of $TiO_2$-II phase for photocatalytic $CO_2$ conversion confirm the high potential of the phase to enhance the activity compered to pure anatase phase. Unlike doped photocatalysts [3-11] which may experience impurity-induced recombination [29], the introduction of $TiO_2$-II modifies the band structure and enhances the activity for $CO_2$ conversion without addition of impurities. Examination of light absorbance, PL, PL decay and photocurrent suggests that the formation of $TiO_2$-II not only enhances the light absorbance but also suppress the recombination and improve the charge carrier mobility to surface to generate photocurrent and contribute to photocatalytic reactions. Moreover, the introduction of $TiO_2$-II induces heterojunctions with other phases such as anatase and rutile which can further enhance the charge separation for photocatalysis [47,62]. The presence of phase heterojunctions, formation of surface vacancies, narrowing the bandgap and easier separation and mobility of charge carriers should be responsible for the improvement of the photocatalytic activity of the samples after HPT processing and annealing. For the annealed sample, removing the vacancies from the bulk by annealing and increasing the energy position of conduction band should contribute to higher photocatalytic activity of this sample compared with the HPT-processed sample. Based on the ATR-FTIR and TPD spectra, $CO_2$ may make a stronger adsorption to the surface of annealed sample, which can be another reason for higher activity of this catalyst.

To have an insight into the photocatalytic activity of the annealed sample (i.e. the activist $TiO_2$-II-containing catalyst in this study), its CO production rate is compared with some reported data in the literature [63-73]. The reported data deviate in a wide range of 0.01-10.16 $\mu mol\ g^{-1}h^{-1}$. Such a wide range of variations is not only due to the differences in the activity of photocatalysts, but also due to the differences in the experimental setup such as light source, gas flow rate, catalyst concentration, specific surface area, etc. Despite differences in the experimental setup, Table 3.4 suggests that the first application of $TiO_2$-II phase for photocatalytic $CO_2$ conversion has led to a good activity ($1.39\pm0.13$ $\mu mol.g^{-1}h^{-1}$ CO production rate) compared to the reported data in the literature. We consider that this activity can be further improved in future by combining the effect of $TiO_2$-II with the other strategies developed so far to enhance the activity such as optimizing the

synthesis method, production of composites, and production of nanosheets, nanoparticles or mesoporous samples with large specific surface area.

Table 3.4. Photocatalytic CO production on annealed $TiO_2$ sample, compared with reported data for other photocatalysts.

| **Photocatalyst** | **Light Source** | **CO Production ($\mu molg^{-1}h^{-1}$)** | **Reference** |
|---|---|---|---|
| $TiO_2$ with $TiO_2$-II by HPT and Anneal | 300 W Hg-Xe | 1.39±0.13 | This Study |
| $TiO_2$ Nanosheet | 150 W Xe | 0.16 | [63] |
| $TiO_2$ Isotropic | 150 W Xe | 1.32 | [63] |
| $TiO_2$ Nanosheet - CN | 150 W Xe | 2.04 | [63] |
| $TiO_2$ Isotropic - CN | 150 W Xe | 1.55 | [63] |
| $TiO_2$ P25 | 150 W Xe | 1.49 | [63] |
| $TiO_2$ Nanosheet - CN Nanosheet | 150 W Xe | 0.12 | [63] |
| $TiO_2$ Nanosheet - CN | 150 W Xe | 0.80 | [63] |
| $TiO_2$ P25 | 300 W Xe | 1.84 | [64] |
| $TiO_2$ Mesoporous | 300 W Xe | 7.0 | [64] |
| $TiO_2$ - $SiO_2$ | 300 W Xe | 6.47 | [64] |
| $TiO_2$ - Graphitic Carbon | 300 W Xe | 10.16 | [64] |
| $TiO_2$ Nanosheets Exposed {001} Facet | 2x18W Hg | 0.12 | [65] |
| $TiO_2$ Pure | 150W UV410 | 0.68 | [66] |
| $TiO_2$ - $CoO_x$ | 150W UV410 | 0.90 | [66] |
| $TiO_2$ - $CoO_x$ Calcined in Air | 150W UV410 | 0.57 | [66] |
| $TiO_2$ Calcined in $N_2/H_2$ | 150W UV410 | 0.49 | [66] |
| $TiO_2$ Hydrogenated - $CoO_x$ | 150W UV410 | 0.81 | [66] |
| $TiO_2$ - $CoO_x$ Hydrogenated | 150W UV410 | 1.24 | [66] |
| $TiO_2$ P25 | 300 W Xe | 1.8 | [67] |
| $TiO_2$ 3D Ordered Microporous | 300 W Xe | 2.9 | [67] |
| $TiO_2$ 3D Ordered Microporous - Au | 300 W Xe | 0.3 | [67] |
| $TiO_2$ 3D Ordered Microporous - $Au_3Pd$ | 300 W Xe | 1.2 | [67] |
| $TiO_2$ 3D Ordered Microporous -$Au_2Pd_2$ | 300 W Xe | 1.8 | [67] |
| $TiO_2$ 3D Ordered Microporous - $AuPd_3$ | 300 W Xe | 2.6 | [67] |
| $TiO_2$ 3D Ordered Microporous - Pd | 300 W Xe | 3.9 | [67] |

| | | | |
|---|---|---|---|
| $C_3N_4$ Nanosheet | 150 W Xe | 0.19 | [63] |
| $C_3N_4$ Graphitic | 150 W Xe | 0.01 | [63] |
| $C_3N_4$ by Thermal Condensation | 350 W Xe | 4.83 | [68] |
| $C_3N_4$ by Solvothermal Process | 350 W Xe | 1.12 | [68] |
| $C_3N_4$ Solvothermal Melamine | 350 W Xe | 0.43 | [68] |
| $C_3N_4$ Solvothermal Melamine | 350 W Xe | 1.69 | [68] |
| $C_3N_4$ by Carbon Tetrachloride Process | 350 W Xe | 0.33 | [68] |
| $C_3N_4$ by Cyclohexane Process | 350 W Xe | 1.23 | [68] |
| $C_3N_4$ by Tetrahydrofuran Process | 350 W Xe | 2.13 | [68] |
| $C_3N_4$ by Solvothermal and Calcination | 350 W Xe | 3.52 | [68] |
| $Cd_{1-x}Zn_xS$ | 100 W LED | 2.9 | [69] |
| BiOI | 300 W Xe | 4.1 | [70] |
| $xCu_2O$ - $Zn_{2-2x}Cr$ | 200-W Hg-Xe | 2.5 | [71] |
| $CeO_{2-x}$ | 300 W Xe | 1.65 | [72] |
| $Cu_2O$ - $RuO_x$ | 150 W Xe | 0.88 | [73] |

### 3.4. Conclusion

Effect of high pressure $TiO_2$-II phase on photocatalytic $CO_2$ conversion was examined for the first time. The introduction of nanostructured $TiO_2$-II phase and $TiO_2$-II/anatase heterojunctions modified the band structure and enhanced the photocurrent and photocatalytic activity, despite the formation of strain-induced vacancies in the bulk. Thermal annihilation of vacancies in the bulk led to further improvement of photocatalytic $CO_2$ conversion, confirming the significance of the $TiO_2$-II phase for photocatalytic reactions.

### References


[1] D.H. Hanaor, C.C. Sorrell, Review of the anatase to rutile phase transformation, J. Mater. Sci. 46 (2011) 855-874.

[2] K. Bourikas, C. Kordulis, A. Lycourghiotis, Titanium dioxide (anatase and rutile): surface chemistry, liquid-solid interface chemistry, and scientific synthesis of supported catalysts, Chem. Rev. 114 (2014) 9754-9823.

[3] W.J. Ong, L.L. Tan, S.P. Chai, S.T. Yong, A.R. Mohamed, Self-assembly of nitrogen-doped $TiO_2$ with exposed 001 facets on a graphene scaffold as photo-active hybrid nanostructures for reduction of carbon dioxide to methane, Nano Res. 7 (2014) 1528-1547.

[4] J.C. Yu, W. Ho, J. Yu, H. Yip, P.K. Wong, J. Zhao, Efficient visible-light-induced photocatalytic disinfection on sulfur-doped nanocrystalline titania, Environ. Sci. Technol. 39 (2005) 1175-1179.

[5] Q. Zhang, Y. Li, E.A. Ackerman, M. Gajdardziska-Josifovska, H. Li, Visible light responsive iodine-doped $TiO_2$ for photocatalytic reduction of $CO_2$ to fuels, Appl. Catal. A 400 (2011) 195-202.

[6] D. Li, H. Haneda, S. Hishita, N. Ohashi, Visible-light-driven N-F-codoped $TiO_2$ photocatalysts. 2. optical characterization, photocatalysis, and potential application to air purification, Chem. Mater. 17 (2005) 2596-2602.

[7] O. Ola, M.M. Maroto-Valer, Synthesis, characterization and visible light photocatalytic activity of metal based $TiO_2$ monoliths for $CO_2$ reduction, Chem. Eng. J. 283 (2016) 1244-1253.

[8] Ş. Neaţu, J.A. Maciá-Agulló, P. Concepción, H. Garcia, Gold-copper nanoalloys supported on $TiO_2$ as photocatalysts for $CO_2$ reduction by water, J. Am. Chem. Soc. 136 (2014) 15969-15976.

[9] K. Kočí, K. Matějů, L. Obalová, S. Krejčíková, Z. Lacný, D. Plachá, L. Čapek, A. Hospodková, O. Šolcová, Effect of silver doping on the $TiO_2$ for photocatalytic reduction of $CO_2$, Appl. Catal. B 96 (2010) 239-244.

[10] S. Linic, P. Christopher, D.B. Ingram, Plasmonic-metal nanostructures for efficient conversion of solar to chemical energy, Nat. Mater. 10 (2011) 911-921.

[11] L. Zhang, Q. Zheng, Y. Xie, Z. Lan, O.V. Prezhdo, W.A. Saidi, J. Zhao, Delocalized impurity phonon induced electron-hole recombination in doped semiconductors, Nano Lett. 18 (2018) 1592-1599.

[12] S. Qamar, F. Lei, L. Liang, S. Gao, K. Liu, Y. Sun, W. Ni, Y. Xie, Ultrathin $TiO_2$ flakes optimizing solar light driven $CO_2$ reduction, Nano Energy, 26 (2016) 692-698.

[13] P. Kar, S. Zeng, Y. Zhang, E. Vahidzadeh, A. Manuel, R. Kisslinger, K.M. Alam, U.K.Thakur, N. Mahdi, P. Kumar, K. Shankar, High rate CO2 photoreduction using flame annealed TiO2 nanotubes, Appl. Catal. B 243 (2019) 522-536.

[14] B. Fang, A. Bonakdarpour, K. Reilly, Y. Xing, F. Taghipour, D.P. Wilkinson, Large-scale synthesis of $TiO_2$ microspheres with hierarchical nanostructure for highly efficient photodriven reduction of $CO_2$ to $CH_4$, ACS Appl. Mater. Interfaces 6 (2014) 15488-15498.

[15] F. Xu, J. Zhang, B. Zhu, J. Yu, J. Xu, $CuInS_2$ sensitized $TiO_2$ hybrid nanofibers for improved photocatalytic $CO_2$ reduction, Appl. Catal. B 230 (2018) 194-202.

[16] A.P. Zhilyaev, T.G. Langdon, Using high-pressure torsion for metal processing: fundamentals and applications, Prog. Mater. Sci. 53 (2008) 893-979.

[17] K. Edalati, Z. Horita, A review on high-pressure torsion (HPT) from 1935 to 1988, Mater. Sci. Eng. A 652 (2016) 325-352.

[18] K. Edalati, Review on recent advancements in severe plastic deformation of oxides by high-pressure torsion (HPT), Adv. Eng. Mater. 21 (2019) 1800272.

[19] H. Razavi-Khosroshahi, K. Edalati, M. Hirayama, H. Emami, M. Arita, M. Yamauchi, H. Hagiwara, S. Ida, T. Ishihara, E. Akiba, Z. Horita, M. Fuji, Visible-light-driven photocatalytic hydrogen generation on nanosized $TiO_2$-II stabilized by high-pressure torsion, ACS Catal. 6 (2016) 5103-5107.

[20] H. Razavi-Khosroshahi, K. Edalati, J. Wu, Y. Nakashima, M. Arita, Y. Ikoma, M. Sadakiyo, Y. Inagaki, A. Staykov, M. Yamauchi, Z. Horita, M. Fuji, High-pressure zinc oxide phase as visible-light-active photocatalyst with narrow band gap, J. Mater. Chem. A 5 (2017) 20298-20303.

[21] Q. Wang, K. Edalati, Y. Koganemaru, S. Nakamura, M. Watanabe, T. Ishihara, Z. Horita, Photocatalytic hydrogen generation on low-bandgap black zirconia ($ZrO_2$) produced by high-pressure torsion, J. Mater. Chem. A 8 (2020) 3643-3650.

[22] P. Thompson, D.E. Cox, J.B. Hastings, Rietveld refinement of Debye-Scherrer synchrotron X-ray data from $Al_2O_3$, J. Appl. Crystallogr. 20 (1987) 79-83.

[23] S.A. Howard, K.D. Preston, Profile fitting of powder diffraction patterns, Rev. Mineral. 20 (1989) 217-275.

[24] R. Delhez, T.H. de Keijser, J.L. Langford, D. Louer, E.J. Mittemeijer, E.J. Sonneveld, Crystal imperfection broadening and peak shape in the Rietveld method, in: R.A. Young (Ed.), The Rietveld Method, Oxford University Press, Oxford, 1995, pp. 132-166.

[25] M.M. Ballari, R. Brandi, O. Alfano, A. Cassano, Mass transfer limitations in photocatalytic reactors employing titanium dioxide suspensions: I. Concentration profiles in the bulk, Chem. Eng. J. 136 (2008) 50-65.

[26] K. Edalati, Q. Wang, H. Razavi-Khosroshahi, H. Emami, M. Fuji, Z. Horita, Low-temperature anatase-to-rutile phase transformation and unusual grain coarsening in titanium oxide nanopowders by high-pressure torsion straining, Scr. Mater. 162 (2019) 341-344.

[27] K. Kočí, L. Obalová, L. Matějová, D. Plachá, Z. Lacný, J. Jirkovský, O. Šolcová, Effect of $TiO_2$ particle size on the photocatalytic reduction of $CO_2$, Appl. Catal. B 89 (2009) 494-502.

[28] M.J. Munoz-Batista, M.M. Ballari, A. Kubacka, O.M. Alfano, M. Fernandez-Garci, Braiding kinetics and spectroscopy in photo-catalysis: the spectro-kinetic approach, Chem. Soc. Rev. 48 (2019) 637-682.

[29] T. Berger, M. Sterrer, O. Diwald, E. Knözinger, D. Panayotov, A.T.L. Thompson, J.J.T. Yates, Light-induced charge separation in anatase $TiO_2$ particles, J. Phys. Chem. B (2005) 6061-6068.

[30] J. Yan, G. Wu, N. Guan, L. Li, Z. Lib, X. Caob, Understanding the effect of surface/bulk defects on the photocatalytic activity of $TiO_2$: anatase versus rutile, Phys. Chem. Chem. Phys. 15 (2013) 10978-10988.

[31] S. Ikeda, N. Sugiyama, S. Murakami, H. Kominami, Y. Kera, H. Noguchi, K. Uosaki, T. Torimoto, B. Ohtani, Quantitative analysis of defective sites in titanium (IV) oxide photocatalyst powders, Phys. Chem. Chem. Phys. 5 (2003) 778-783.

[32] S. Murakami, H. Kominami, Y. Kera, S. Ikeda, H. Noguchi, K. Uosaki, B. Ohtani, Evaluation of electron-hole recombination properties of titanium (IV) oxide particles with high photocatalytic activity, Res. Chem. Intermed. 33 (2007) 285-296.

[33] M.Y. Kuo, C.L. Chen, C.Y. Hua, H.C. Yang, P.J. Shen, Density functional theory calculations of sense $TiO_2$ polymorphs: implication for visible-light-responsive photocatalysts, Phys. Chem. B 109 (2005) 8693-8700.

[34] T. Zhu, S.P. Gao, The Stability, electronic structure, and optical property of $TiO_2$ polymorphs, J. Phys. Chem. C 2014, 118, 11385-11396.

[35] X. Li, J. Yu, M. Jaroniec, Hierarchical photocatalysts, Chem. Soc. Rev. 45 (2016) 2603-2636.

[36] E. Kalamaras, M.M. Maroto-Valer, M. Shao, J. Xuan, H. Wang, Solar carbon fuel via photoelectrochemistry, Catal. Today 317 (2018) 56-75.

[37] U. Ulmer, T. Dingle, P.N. Duchesne, R.H. Morris, A. Tavasoli, T. Wood, G.A. Ozin, Fundamentals and applications of photocatalytic $CO_2$ methanation, Nat. Commun. 10 (2019) 3169.

[38] B. AlOtaibi, S. Fan, D. Wang, J. Ye, Z. Mi, Wafer-level artificial photosynthesis for $CO_2$ reduction into $CH_4$ and CO using GaN nanowires, ACS Catal. 5 (2015) 5342-5348.

[39] J. Yan, G. Wu, N. Guan, L. Li, Z. Li, X. Cao, Understanding the effect of surface/bulk defects on the photocatalytic activity of $TiO_2$: anatase versus rutile, Phys. Chem. Chem. Phys. 15 (2013) 10978-10988.

[40] D.K. Pallotti, L. Passoni, P. Maddalena, F.D. Fonzo, S. Lettieri, Photoluminescence mechanisms in anatase and rutile $TiO_2$, J. Phys. Chem. C 121 (2017) 9011-9021.

[41] A. Yamakata, J.J. M. Vequizo, H. Matsunaga, Distinctive behavior of photogenerated electrons and holes in anatase and rutile $TiO_2$ powders, J. Phys. Chem. C 119 (2015) 24538-24545.

[42] Z. Zhang, K. Liu, Z. Feng, Y. Bao, B. Dong, Hierarchical sheet-on-sheet $ZnIn_2S_4$/g-$C_3N_4$ heterostructure with highly efficient photocatalytic $H_2$ production based on photoinduced interfacial charge transfer, Sci. Rep. 6 (2016) 19221.

[43] R. Brüninghoff, K. Wenderich, J.P. Korterik, B.T. Mei, G. Mul, A. Huijser, Time-dependent photoluminescence of nanostructured anatase $TiO_2$ and the role of bulk and surface processes, J. Phys. Chem. C 123 (2019) 26653-26661.

[44] X.H. Wang, J.G. Li, H. Kamiyama, M. Katada, N. Ohashi, Y. Moriyoshi, T.J. Ishigaki, Pyrogenic iron(III)-doped $TiO_2$ nanopowders synthesized in RF thermal plasma: phase formation, defect structure, band gap, and magnetic properties, J. Am. Chem. Soc. 127 (2005) 10982-10990.

[45] I. Nakamura, N. Negishi, S. Kutsuna, T. Ihara, S. Sugihara, K.J. Takeuchi, Role of oxygen vacancy in the plasma-treated $TiO_2$ photocatalyst with visible light activity for NO removal, J. Mol. Catal. A: Chem. 161 (2000) 205-212.

[46] F.J. Knorr, J. McHale, Spectroelectrochemical photoluminescence of trap states of nanocrystalline $TiO_2$ in aqueous media, J. Phys. Chem. C 117 (2013),13654-13662.

[47] M.C. Wu, C.H. Chen, W.K. Huang, K.C. Hsiao, T.H. Lin, S.H. Chan, P.Y. Wu, C.F. Lu, Y.H. Chang, T.F. Lin, K.H. Hsu, J.F. Hsu, K.M. Lee, J.J. Shyue, K. Kordás, W.F. Su,

Improved solar-driven photocatalytic performance of highly crystalline hydrogenated $TiO_2$ nanofibers with core-shell structure, Sci. Rep. 7 (2017) 40896.

[48] M. Kong, Y. Li, X. Chen, T. Tian, P. Fang, F. Zheng, X. Zhao, Tuning the concentration ratio of bulk defects to surface defects in $TiO_2$ nanocrystals leads to high photocatalytic efficiency, J. Am. Chem. Soc. 133 (2011) 16414-16417.

[49] W. Sun, Y. Li, W. Shi, X. Zhao, P. Fang, Formation of AgI/$TiO_2$ nanocomposite leads to excellent thermochromic reversibility and photostability, J. Mater. Chem. 21 (2011) 9263-9270.

[50] Y. Wang, J. Li, Y. Zhou, Z. Gao, W. Zhu, L. Liu, Interfacial defect mediated charge carrier trapping and recombination dynamics in $TiO_2$-based nanoheterojunctions, J. Alloy Compd. 872 (2021) 159592.

[51] A.J. Morris, G.J. Meyer, E. Fujita, Molecular approaches to the photocatalytic reduction of carbon dioxide for solar fuels. Acc. Chem. Res. 42 (2009) 1983-1994.

[52] J. Ran, M. Jaroniec, S.Z. Qiao, Cocatalysts in semiconductor-based photocatalytic $CO_2$ reduction: achievements, challenges, and opportunities, Adv. Mater. 30 (2018) 1704649.

[53] T.P. Nguyen, D.L.T. Nguyen, V.H. Nguyen, T.H. Le, D.V.N. Vo, Q.T. Trinh, S.R. Bae, S.Y. Chae, S.Y. Kim, Q.V. Le, Recent advances in $TiO_2$-based photocatalysts for reduction of $CO_2$ to fuels, Nanomaterials 10 (2020) 337.

[54] K. Li, B. Peng, T. Peng, Recent advances in heterogeneous photocatalytic $CO_2$ conversion to solar fuels, ACS Catal. 6 (2016) 7485-7527.

[55] L.Y. Lin, S. Kavadiya, X. He, W.N. Wang, B.B. Karakocak, Y.C. Lin, M.Y. Berezin, P. Biswas, Engineering stable Pt nanoparticles and oxygen vacancies on defective $TiO_2$ via introducing strong electronic metal-support interaction for efficient $CO_2$ photoreduction, Chem. Eng. J. 389 (2020) 123450.

[56] A.A. Davydov, Infrared Spectroscopy of Adsorbed Species on the Surface of Transition Metal Oxides, Wiley and Sons, Chichester, UK, 1990.

[57] K.L. Kauffman, J.T. Culp, A. Goodman, C. Matranga, FT-IR study of $CO_2$ adsorption in a dynamic copper (II) benzoate - pyrazine host with $CO_2$-$CO_2$ interactions in the adsorbed state, J. Phys. Chem. C 115 (2011) 1857-1866.

[58] K. Wang, J. Lu, Y. Lu, C.H. Lau, Y. Zheng, X. Fan, Unravelling the C-C coupling in $CO_2$ photocatalytic reduction with $H_2O$ on Au/$TiO_{2-x}$: combination of plasmonic excitation and oxygen vacancy, Appl. Catal. B 292 (2021) 120147.

[59] S.R. Lingampalli, M.M. Ayyub, C.N.R. Rao, Recent progress in the photocatalytic reduction of carbon dioxide, ACS Omega 2 (2017) 2740-2748.

[60] S.N. Habisreutinger, L. Schmidt-Mende, J.K. Stolarczyk, Photocatalytic reduction of CO2 on TiO2 and other semiconductors, Angew. Chem. Int. Ed. 52 (2013) 7372-7408.

[61] S. Zeng, E. Vahidzadeh, C.G. VanEssen, P. Kar, R. Kisslinger, A. Goswami, Y. Zhang, N. Mahdi, S. Riddell, A.E. Kobryn, S. Gusarov, P. Kumar, K. Shankar, Optical control of selectivity of high rate $CO_2$ photoreduction via interband- or hot electron Z-scheme reaction pathways in Au-$TiO_2$ plasmonic photonic crystal photocatalyst, Appl. Catal. B 267 (2020) 118644.

[62] J. Knorr, J.L. McHale, Spectroelectrochemical photoluminescence of trap states of nanocrystalline $TiO_2$ in aqueous media fritz, J. Phys. Chem. C 117 (2013) 13654-13662.

[63] A. Crake, K.C. Christoforidis, R. Godin, B. Moss, A. Kafizas, S. Zafeiratos, J.R. Durrant, C. Petit, Titanium dioxide/carbon nitride nanosheet nanocomposites for gas phase $CO_2$ photoreduction under UV-visible irradiation, Appl. Catal. B 242 (2019) 369-378.

[64] Y. Wang, Y. Chen, Y. Zuo, F. Wang, J. Yao, B. Li, S. Kang, X. Li, L. Cui, Hierarchically mesostructured $TiO_2$/graphitic carbon composite as a new efficient photocatalyst for the reduction of $CO_2$ under simulated solar irradiation, Catal. Sci. Technol. 3 (2013) 3286-3291.

[65] Z. He, L. Wen, D. Wang, Y. Xue, Q. Lu, C. Wu, J. Chen, S. Song, Photocatalytic reduction of $CO_2$ in aqueous solution on surface-fluorinated anatase $TiO_2$ nanosheets with exposed {001} facets, Energy Fuels. 28 (2014) 3982-3993.

[66] Y. Li, C. Wang, M. Song, D. Li, X. Zhang, Y. Liu, $TiO_{2-x}$/$CoO_x$ photocatalyst sparkles in photothermocatalytic reduction of $CO_2$ with $H_2O$ steam, Appl. Catal. B 243 (2019) 760–770.

[67] J. Jiao, Y. Wei, Y. Zhao, Z. Zhao, A. Duan, J. Liu, Y. Pang, J. Li, G. Jiang, Y. Wang, AuPd/3DOM-$TiO_2$ catalysts for photocatalytic reduction of $CO_2$: High efficient separation of photogenerated charge carriers, Appl. Catal. B 209 (2017) 228-239.

[68] P. Xia, M. Antonietti, B. Zhu, T. Heil, J. Yu, S. Cao, Designing defective crystalline carbon nitride to enable selective $CO_2$ photoreduction in the gas phase, Adv. Funct. Mater. 29 (2019) 1900093.

[69] E.A. Kozlova, M.N. Lyulyukin, D.V. Markovskaya, D.S. Selishchev, S.V. Cherepanova, D.V. Kozlov, Synthesis of $Cd_{1-x}Zn_xS$ photocatalysts for gas-phase $CO_2$ reduction under visible light, Photochem. Photobiol. Sci. 18 (2019) 871-877.

[70] L. Ye, H. Wang, X. Jin, Y. Su, D. Wang, H. Xie, X. Liu, X. Liu, Synthesis of olive-green few-layered BiOI for efficient photoreduction of $CO_2$ into solar fuels under visible/near-infrared light, Sol. Energy Mater. Sol. Cells 144 (2016) 732-739.

[71] H. Jiang, K. Katsumata, J. Hong, A. Yamaguchi, K. Nakata, C. Terashima, N. Matsushita, M. Miyauchi, A. Fujishima, Photocatalytic reduction of $CO_2$ on $Cu_2O$-loaded Zn-Cr layered double hydroxides, Appl. Catal. B 224 (2018) 783-790.

[72] T. Ye, W. Huang, L. Zeng, M. Li, J. Shi, $CeO_{2-x}$ platelet from monometallic cerium layered double hydroxides and its photocatalytic reduction of $CO_2$, Appl. Catal. B 210 (2017) 141-148.

[73] E. Pastor, F. Pesci, A. Reynal, A. Handoko, M. Guo, X. An, A. Cowan, D. Klug, J. Durrant, J. Tang, Interfacial charge separation in $Cu_2O/RuO_x$ as a visible light driven $CO_2$ reduction catalyst, Phys. Chem. Chem. Phys. 16 (2014) 5922-5926.

# Chapter 4. Defective high-entropy oxide photocatalyst with high activity for $CO_2$ conversion

## 4.1. Introduction

High-entropy ceramics are a new type of materials which show high stability and promising structural and functional properties due to the so-called cocktail effect, lattice strain/defects, heterogenous valence electron distribution and high configurational entropy [1]. As shown in Fig. 4.1a, high-entropy ceramics are defined as multi-component materials with at least five principal elements and a configurational entropy higher than 1.5*R* (*R*: the gas constant) [2]. These materials have a low Gibbs free energy due to their high entropy and this gives a high stability to these materials under different conditions [1] including catalytic reactions [3,4]. Moreover, the presence of at least five cations with different atomic sizes in these materials results in the formation of inherent lattice strain and defects [2]. Since lattice strain and defects are effective to enhance photocatalytic $CO_2$ conversion [5-8], the high-entropy ceramics are expected to show good activity for such a conversion. High-entropy oxides (HEOs) are the most popular high-entropy ceramics which have been investigated for various applications and properties such as thermal barrier coatings [9,10], magnetic components [11,12], dielectric components [13,14], Li-ion batteries [15,16], Li-S batteries [17], Zn-air batteries [18], catalysts [19,20], electrocatalysts [21], and photocatalytic hydrogen production [22,23]. Despite the inherent defective and strained structure of HEOs, there have been no attempts to employ these materials for photocatalytic $CO_2$ conversion.

In this chapter, a HEO photocatalyst, $TiZrNbHfTaO_{11}$, is synthesized and its activity for $CO_2$ conversion is examined. The transition elements titanium, zirconium, niobium, hafnium, and tantalum are selected simply because their binary oxides with the $d^0$ electronic structure can act as photocatalysts. This first application of HEOs for photocatalytic $CO_2$ conversion confirms that the HEO photocatalyst shows higher activity compared to common binary or ternary photocatalysts such as $TiO_2$ and $BiVO_4$, suggesting HEOs as a new family of photocatalysts for $CO_2$ conversion.

## 4.2. Experimental

### *4.2.1. Sample preparation*

Although various methods have been developed in recent years for the synthesis of HEO [1-4,9-23], a two-step high-pressure mechanical alloying and high-temperature oxidation which is available in the authors' laboratory was used to synthesize the HEO. In the first step, equiatomic amounts of Ti (99.9%), Zr (95.0%), Hf (99.5%), Nb (99.9%) and Ta (99.9%) powders were mixed in acetone, treated by ultrasonic and then dried. The dried powder mixture was processed by high-pressure torsion (HPT), shown in Fig. 4.1b, to fabricate TiZrNbHfTa high entropy alloy (HEA) with the body-centered cubic (BCC) structure (see the principles of HPT and its applications to oxides in [24,25]). To produce the TiZrNbHfTa alloy, a 10 mm diameter and 1 mm thick disc was prepared by compacting the powder mixture under a pressure of 400 MPa. The compacted disc was then compressed between two HPT anvils under a high pressure of 6 GPa at room temperature and simultaneously processed by rotating the lower HPT anvil with respect to the upper one for 100 turns with a rotation rate of one turn per minute. In the second step, the HPT-processed TiZrNbHfTa alloy was exposed to hot air at a temperature of 1373 K for 24 h to produce an oxide, with the appearance shown in Fig. 4.1c. Examination of the mass of sample before and after oxidation suggested a composition of $TiZrNbHfTaO_{11}$ for the produced oxide. The oxide was crushed after oxidation into the powder form using a mortar and examined by various characterization methods, as described below.

### *4.2.2. Characterization*

To examine the crystal structure, X-ray diffraction (XRD) using the Cu Kα radiation with a wavelength of $\lambda$ = 0.1542 nm and micro-Raman spectroscopy using a laser source with a wavelength of $\lambda$ = 532 nm were utilized.

Examination of microstructure was conducted by (i) scanning electron microscopy (SEM) with energy dispersive X-ray spectroscopy (EDS) analysis under 15 keV, (ii) transmission electron microscopy (TEM) with selected area electron diffraction (SAED), bright-field (BF) images, dark-field (DF) images, high-resolution images and fast Fourier transform (FFT) analysis under 200 keV, and (iii) scanning-transmission electron microscopy (STEM) with high-angle annular dark-field (HAADF) images and EDS analysis under 200 keV.

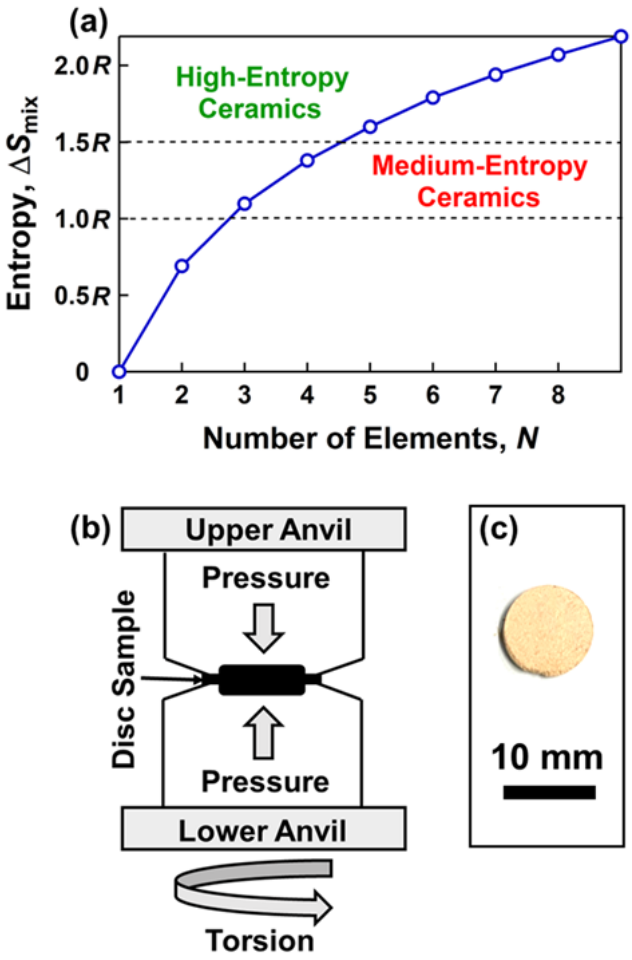


Fig. 4.1. (a) Relationship between number of elements and configurational entropy and definition of high-entropy ceramics with equiatomic fractions of elements, (b) schematic illustration of high-pressure torsion (HPT), and (c) appearance of high-entropy oxide synthesized in this study.

To investigate the presence of point defects such as oxygen vacancies, electron paramagnetic resonance (EPR) was performed at ambient temperature using a microwave source with a frequency of 9.4688 GHz.

To study the oxidation states of different elements and to estimate the valence band top position, X-ray photoelectron spectroscopy (XPS) using the Al $K_\alpha$ radiation with a wavelength of $\lambda$ = 0.989 nm was used. The XPS energy position for each element was adjusted by considering the peak position of C 1s at 284.8 eV. After correction of the energy positions, the peaks for different elements were analyzed by peak deconvolution by considering the standard energy

relations and differences reported in the handbook [26]: $f_{7/2}$:$f_{5/2}$ = 4:3, $d_{5/2}$:$d_{3/2}$ = 3:2, $p_{3/2}$:$p_{1/2}$ = 2:1, Ti $2p_{1/2}$ - Ti $2p_{3/2}$ = 5.54 eV, Zr $3d_{3/2}$ - Zr $3d_{5/2}$ = 2.43 eV, Hf $4f_{5/2}$ - Hf $4f_{7/2}$ = 1.71 eV, Nb $3d_{3/2}$ - Nb $3d_{5/2}$ = 2.72 eV, Ta $4f_{5/2}$ - Ta $4f_{7/2}$ = 1.91 eV.

To investigate the light absorbance and bandgap (Kubelka-Munk analysis), UV-vis diffuse reflectance spectroscopy was conducted, and the band structure was calculated by considering both XPS and UV-vis spectra.

To study the lifetime of exited electrons, steady-state photoluminescence (PL) emission spectroscopy with a 325 nm laser source and time-resolved photoluminescence decay (PL decay) with a 285 nm laser source were conducted.

The specific surface area of powder was examined by nitrogen gas adsorption and using the Brunauer-Emmett-Teller (BET) method.

#### *4.2.3. Photocurrent test*

Photocurrent generation was examined using a thin film of sample in a 1 M $Na_2SO_4$ electrolyte under the full arc of Xe lamp (without using any filter), as described in detail earlier [27]. The thin film was prepared by deposition of HEO powder on FTO (fluorine-doped tin oxide) glass with 2.25 mm thickness and 15×25 $mm^2$ surface area. about 5 mg of sample was crushed in 0.2 mL ethanol and carefully dispersed on the FTO glass using a drop and annealed at 473 K for 24 h. The average thickness of HEO on FTO glass was about 0.04 mm, which was estimated by measuring the thickness of glass before and after deposition of HEO using a micrometer with 0.01 mm accuracy. Photocurrent generation was examined by an electrochemical analyzer in the potentiostatic amperometry mode during time (30 s light ON and 60 s light OFF), while the counter electrode was Pt wire, the reference electrode was Ag/AgCl, and the external potential was 0.7 V vs. Ag/AgCl.

#### *4.2.4. Photocatalytic test*

Photocatalytic $CO_2$ conversion was conducted using the powder of HEO in a continuous flow quartz photoreactor. The photoreactor, as shown in Fig. 4.2a, had a cylindrical shape with a total inner volume of 858 mL. The reactor had an inner space to insert the light source. There were two holes on the top of photoreactor: one for the inlet of $CO_2$ flow, which was connected to a gas cylinder; and another one for the outlet of gas and sampling the reaction products for analysis,

which was connected to a vent and gas chromatograph. For the photocatalytic reaction, 120 mg of HEO was mixed with 500 mL of deionized water and $NaHCO_3$ with 1 M concentration and then bubbled with $CO_2$ with a flow rate of 3 mL/min. The temperature was controlled as 288 K using a water chiller and the suspension was continuously stirred using a magnetic stirrer. The process was first conducted for 2 h without light irradiation, and after confirmation that no reaction products appear, the photocatalytic test was conducted under irradiation with a high-pressure Hg light source (Sen Lights Corporation, HL400BH-8, 400 W, with the spectral composition shown in Fig. 4.2b). The light intensity irradiated on the photocatalysts was 0.5 W/cm$^2$ and no filter was used during the irradiation. The reaction products were analyzed by a gas chromatograph (Shimadzu GC-8A, Ar Carrier). A flame ionization detector equipped with a methanizer (Shimadzu MTN-1) was used to measure the CO and $CH_4$ production rate. A thermal conductivity detector also was utilized to evaluate the $H_2$ and $O_2$ production. To be sure about the absence of CO from other sources such as contamination, blank tests were conducted (i) under irradiation in the presence of $CO_2$, $NaHCO_3$ and $H_2O$ and without the photocatalyst addition and (ii) under irradiation in the presence of Ar, $NaHCO_3$ and $H_2O$ and with photocatalyst addition.

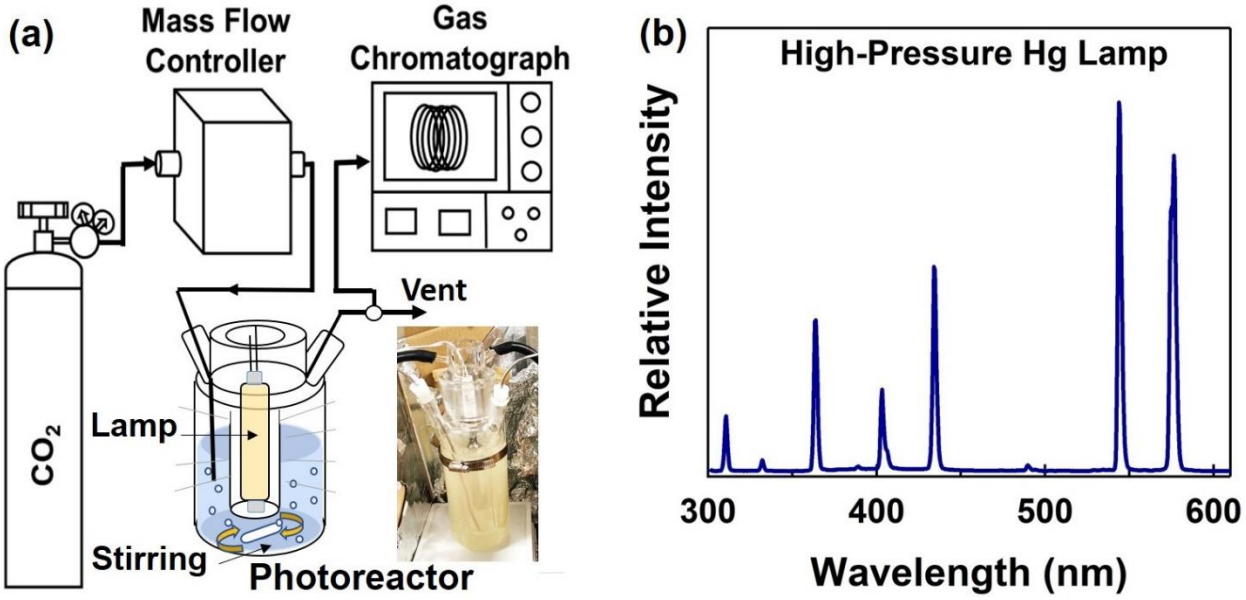


Fig. 4.2. (a) Description of experimental setting for photocatalytic $CO_2$ conversion including photograph of photoreactor, and (b) spectroscopy of light source used for photocatalytic test.

## 4.3. Results

### *4.3.1. Crystal structure and microstructure*

Fig. 4.3 shows the SEM images of HEO in various scales. Particle size measured by SEM is 25 µm. The HEO contains particles with different sizes, as shown in Fig. 4.3, and its specific surface area, achieved by the BET method, is 0.66 $m^2/g$. Although big size of some particles can have negative effect on photocatalytic activity due to decreasing the active surface area, this issue can be addressed in the future by using other synthesis method or advanced crushing techniques. The presence of numerous nanograins in each particle is obvious in higher magnification images in Fig. 4.3b, c and d. The average grain size for this material is estimated to be 192 nm, while some pores are also visible within the particles. Here, it should be noted that low specific surface area and small grain size are characteristics of materials which are synthesized/processed by the HPT method [22-25].

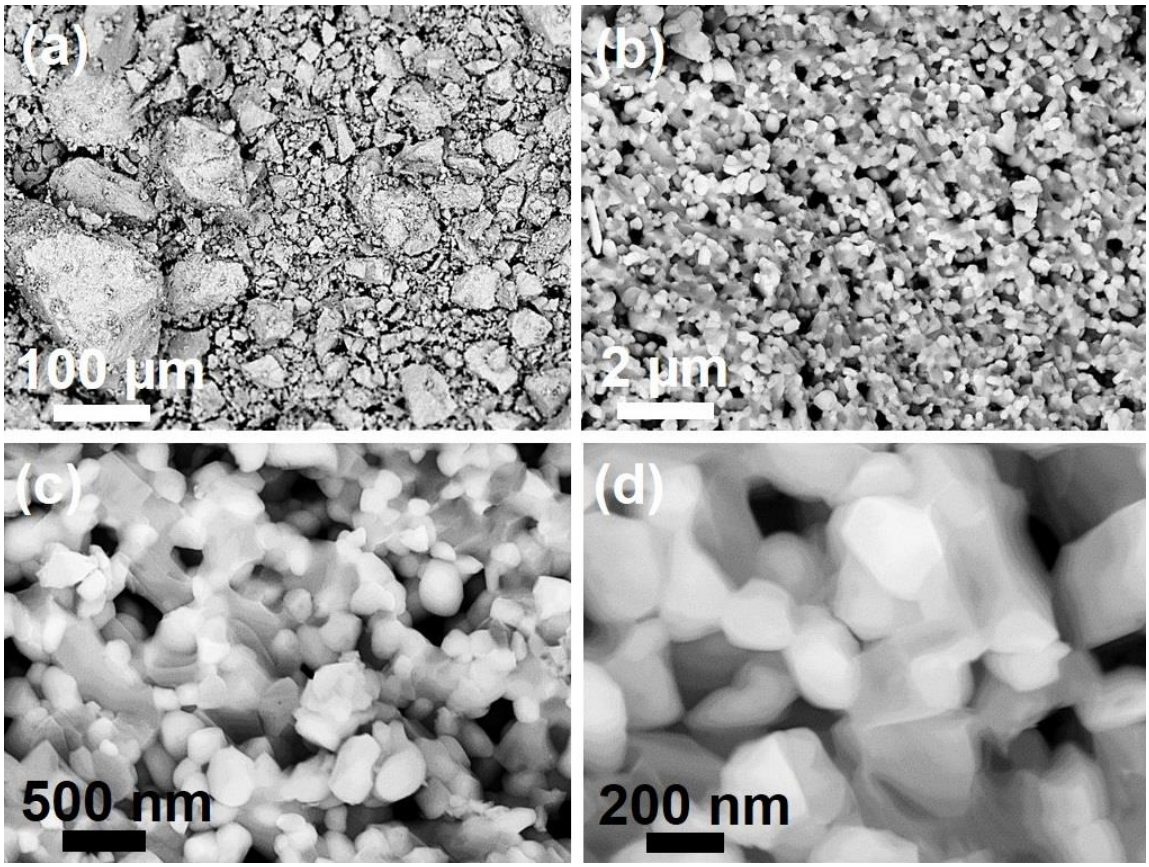


Fig. 4.3. Morphology of high-entropy oxide examined by SEM at different magnifications.

To confirm the successful oxidation of the material, electronic states of each element in the HEO are presented in Fig. 4.4 using the XPS analysis and corresponding peak deconvolution. Fig. 4.4 shows that the main cations in the sample are $Ti^{4+}$, $Zr^{4+}$, $Nb^{5+}$, $Hf^{4+}$ and $Ta^{5+}$, suggesting that the material is successfully oxidized to a $d^0$ electronic configuration during the high-temperature oxidation [26]. However, it should be noted that the peaks for Ti, Zr, Nb, Hf and Ta have some shoulders to the lower energy sides, suggesting that some oxygen-deficient regions with lower oxidation states should exist within the material, as confirmed by the peak deconvolution analysis (i.e., some oxygen vacancies present). The presence of vacancies is not surprising as similar issue can be observed in other HPT-processed materials due to the strain effect [24,25] and in other HEOs due to the atomic size mismatch effect [1,2].

To confirm the distribution of elements in the material, Fig. 4.5a and Fig. 4.5b illustrate the elemental distribution mappings in the micrometer and nanometer scales, respectively. Fig. 4.5 shows that the elements distribute appropriately in both micrometer and nanometer scales. It is confirmed that the elements are successfully mixed by high-pressure mechanical alloying and their distribution remains reasonably homogeneous even after high-temperature oxidation. SEM-EDS analysis suggests that the material should have a general composition of $TiZrNbHfTaO_{11}$. Uniform distribution of elements is a general requirement of high-entropy materials [1-4,9-23].

Crystal structure of HEO was examined using XRD analysis, as shown in Fig. 4.6a. The material contains two phases with the monoclinic and orthorhombic structures. Based on the Rietveld analysis, the HEO consists of 40 wt% of monoclinic phase (A2/m space group, $a$ = 1.193 nm, $b$ = 0.381 nm, $c$ = 2.044 nm, $\alpha$ = 90°, $\beta$ = 120.16°, $\gamma$ = 90°) and 60 wt% of orthorhombic phase (Ima2 space group, $a$ = 4.092 nm, $b$ = 0.493 nm, $c$ = 0.527 nm, $\alpha = \beta = \gamma$ = 90°). Raman spectra, shown in Fig. 4.6b from three different positions, illustrate similar patterns in different positions, suggesting the size of phases should be smaller than the spatial resolution of micro-Raman. Taken altogether, a combination of XPS, EDS and XRD confirms that a dual-phase HEO could be successfully produced in this study.

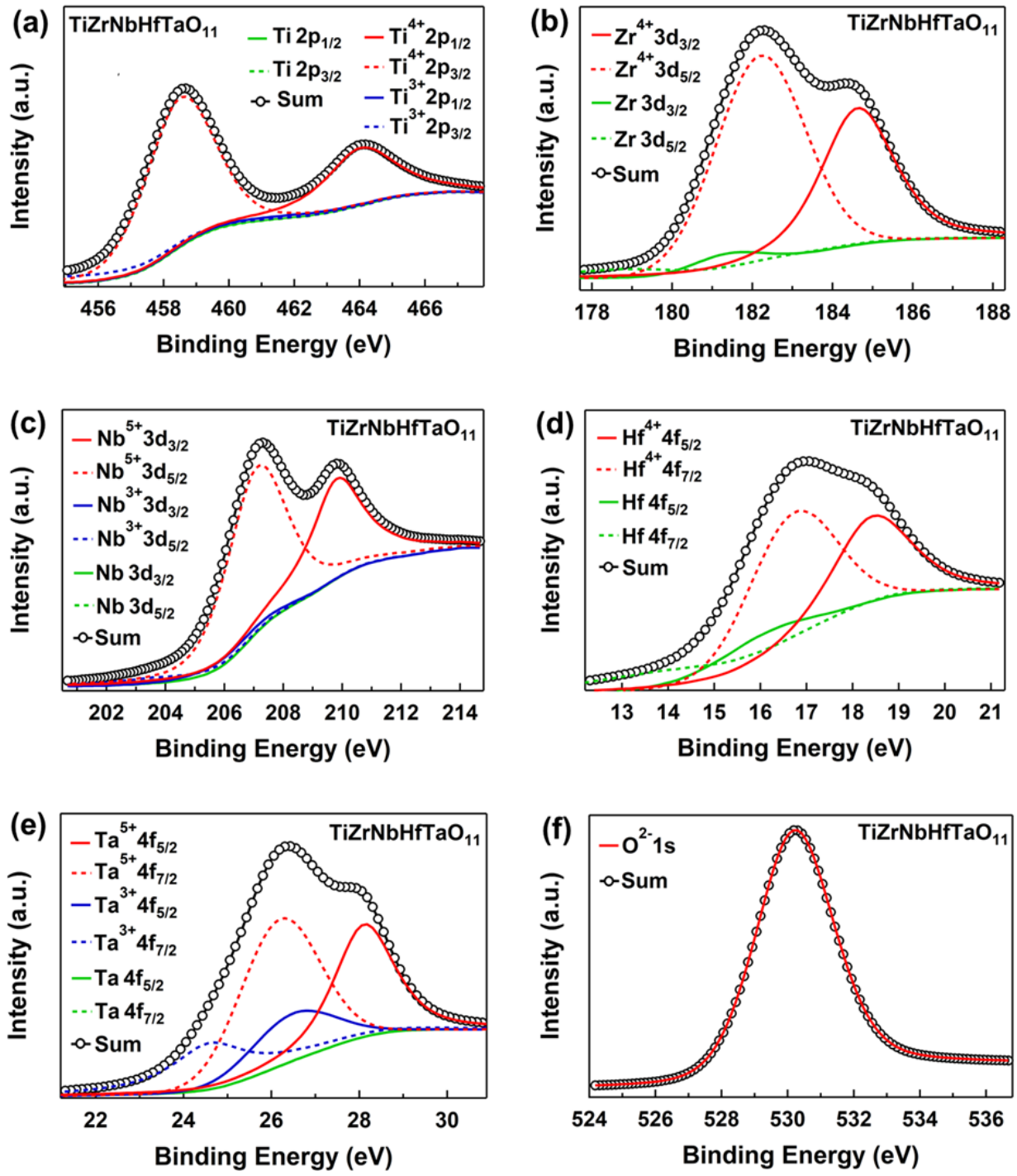


Fig. 4.4. Electronic states and relevant peak deconvolution of (a) Ti, (b) Zr, (c) Nb, (d) Hf, (e) Ta and (f) O in high-entropy oxide examined by XPS analysis.

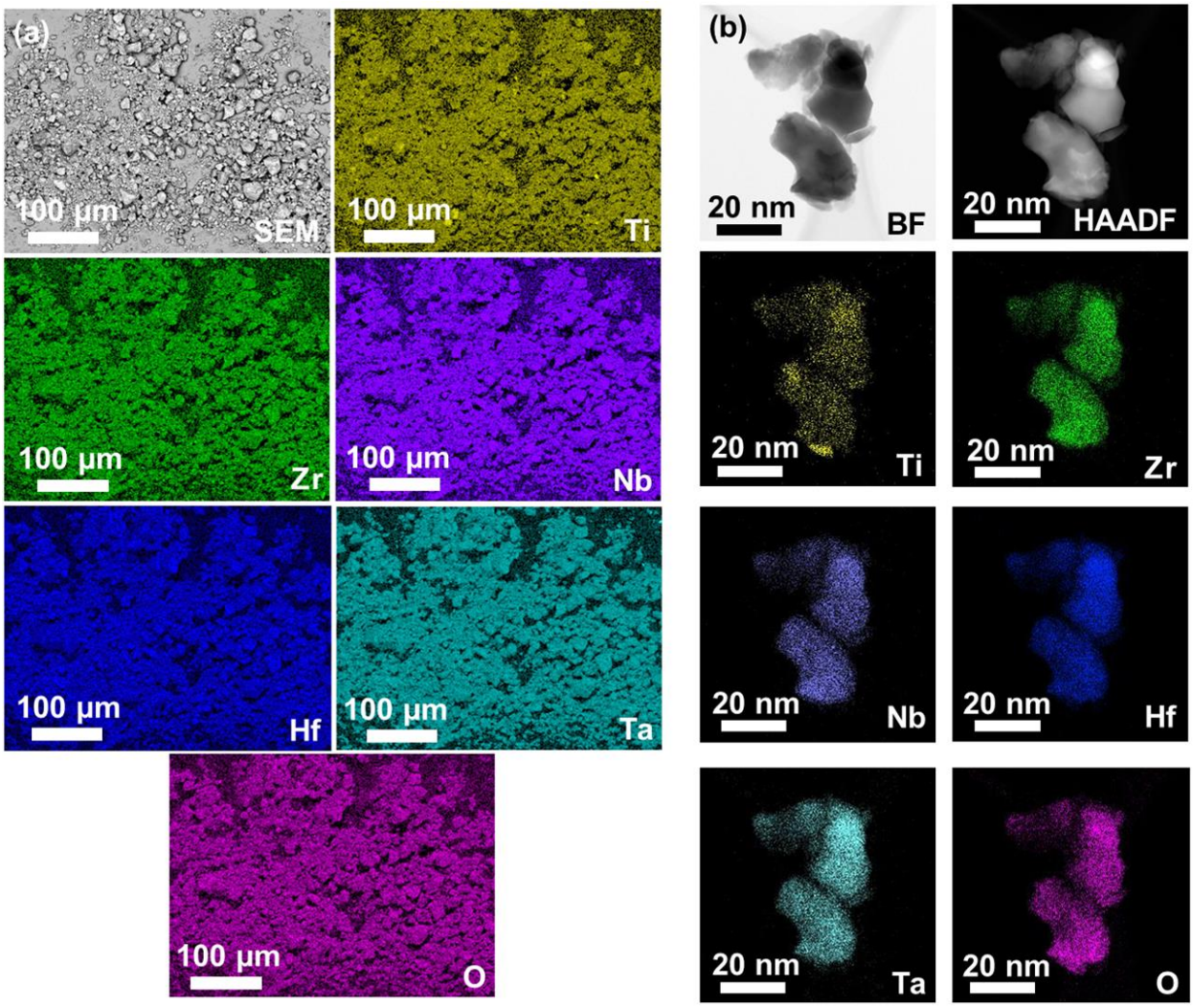


Fig. 4.5. Distribution of elements in high-entropy oxide examined at (a) micrometer scale using SEM-EDS and (b) nanometer scale using STEM-EDS.

Examination of microstructural/nanostructural features of this dual-phase HEO is shown in Fig. 4.7, where a is a BF image, b is a corresponding SAED pattern, c is a DF image, d and e are HR images, and f is a magnified lattice image of the selected squared region in e. Fig. 4.7 reveals several important points. (i) A ring pattern of SAED image confirms the presence of many nanocrystals with random orientation in Fig. 4.7a. (ii) The BF and DF images confirm that the grain sizes are quite small and less than 100 nm. This indicates that there are still smaller crystals within the grain-like regions observed in the SEM images of Fig. 4.3. (iii) The HR images confirm the co-existence of two monoclinic and orthorhombic phases at the nanoscale and large fraction of

interphase boundaries. It was shown that the presence of interphases as charge heterojunctions can improve the photocatalytic activity through enhanced charge carrier separation and mobility [28]. (iv) The lattice images are quite distorted and close examination of the lattice confirms the presence of many dislocation defects within the grains. Since it was reported that the dislocations can enhance the light absorbance and photocatalytic activity at least in some semiconductors [29], the presence of dislocations in this HEO may positively act for enhancement of photocatalytic activity.

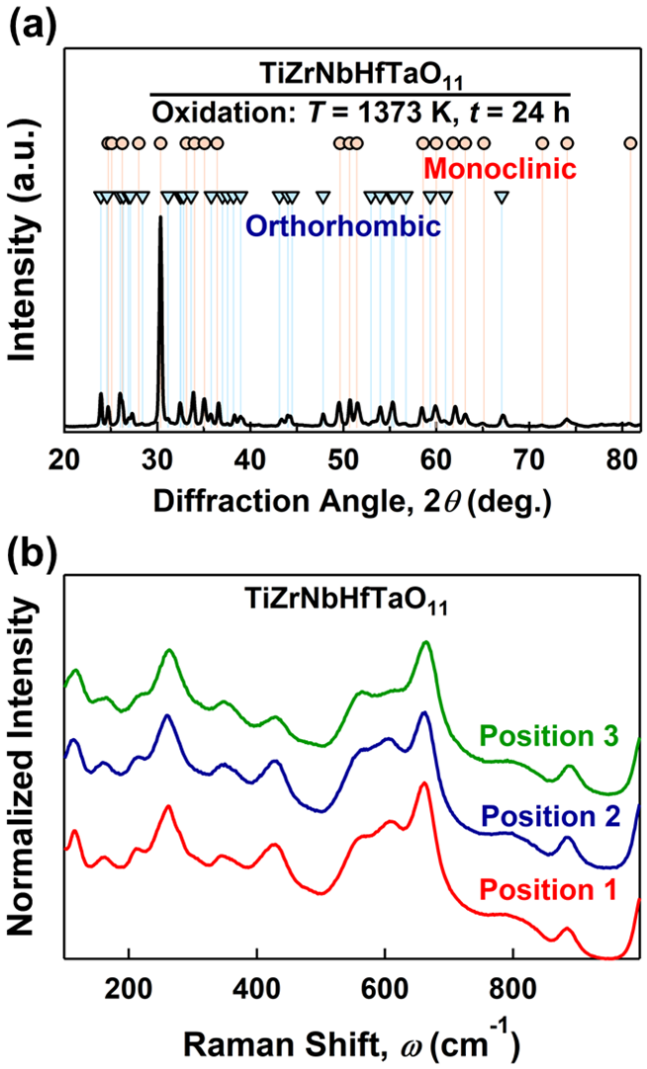


Fig. 4.6. Dual-phase structure of high-entropy oxide examined by (a) XRD profile and (b) micro-Raman spectra at three different positions.

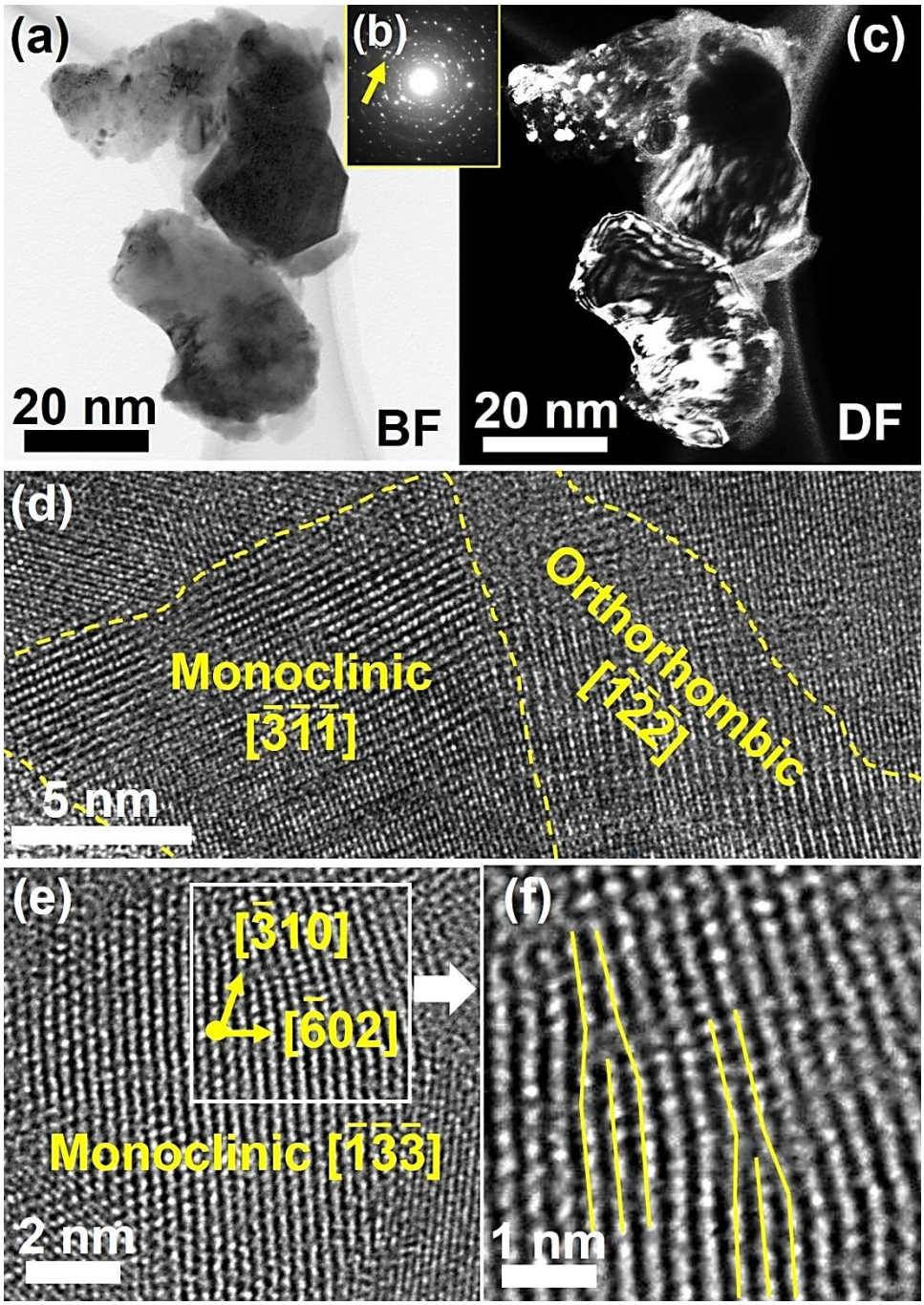


Fig. 4.7. Presence of nanoscaled dual phases with large fraction of interfaces and dislocations in high-entropy oxide examined by TEM (a) BF image, (b) SAED analysis, (c) DF image and (d-f) HR images, where (c) was taken with diffracted beams indicated by arrow in (a), and (f) is a magnified view of squared region in (e).

### *3.2. Electronic structure and defect states*

Fig. 4.8 shows (a) UV-vis absorbance spectrum, (b) Kubelka-Munk plot, (c) XPS spectrum of top of valence band and (d) electronic structure determined by a combination of UV-vis and XPS analyses. Fig. 8a indicates that the HEO can absorb light in both ultraviolet and visible light regions, although the quantity of absorbed light in the ultraviolet region is higher than that in the visible light region. Such a visible light absorbance is not detected in binary oxides such as $TiO_2$, $ZrO_2$, $HfO_2$, $Nb_2O_5$ and $Ta_2O_5$ [27,29].

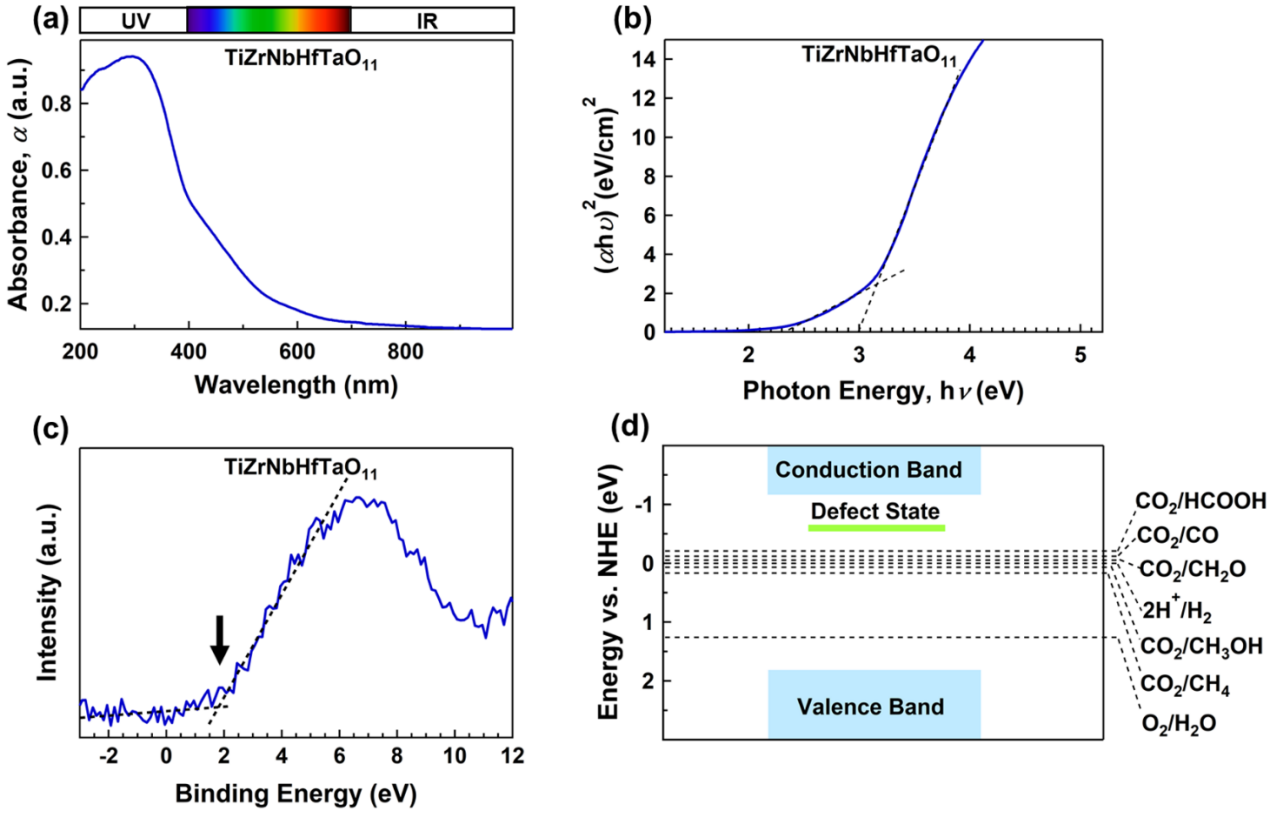


Fig. 4.8. Appropriate electronic structure of high-entropy oxide for photocatalytic $CO_2$ conversion. (a) UV-vis light absorbance spectrum, (b) Kubelka-Munk plot to calculate indirect bandgap ($\alpha$: light absorption, h: Planck's constant, $\nu$: light frequency), (c) XPS spectrum to estimate top of valence band, and (d) electronic band structure in comparison with potentials for photocatalytic $CO_2$ conversion.

Based on the Kubelka-Munk analysis, there are two apparent bandgaps of 3.0 and 2.3 eV for this HEO. The first energy gap should be related to the energy difference between the valence band and conduction band which is reasonably similar to the bandgap of $TiO_2$ and smaller than the bandgap of other binary oxides in the Ti-Zr-Hf-Nb-Ta-O system (3.1-5.7 eV) [30,31], and the second gap should be due to the defect level between the valence band and conduction band. The presence of defects (i.e., oxygen vacancies or color centers), which can be confirmed from the low energy shoulders in XPS spectra of cations, should be a main reason for the orange color of sample. The top of valence band calculated by XPS is 1.8 eV vs. NHE, which is shown by an arrow in Fig. 4.8c. The bottom of conduction band is calculated as -1.2 vs. NHE by considering an indirect bandgap of 3.0 eV and the defect state is estimated as -0.5 eV vs. NHE. As summarized in Fig. 4.8d, the potential of reactions for $CO_2$ conversion and water splitting (see Table 4.1) are between the energy levels for the top of valence band and the bottom of conduction band, and thus, this HEO can basically satisfy the requirements for photocatalytic reactions [28,32,33].

#### *4.3.3. Charge-carrier dynamics*

Charge-carrier dynamics were examined by (a) steady-state PL spectroscopy, (b) PL decay spectroscopy, (c) EPR spectroscopy and (d) photocurrent measurement, as shown in Fig. 4.9. The PL spectrum in Fig. 4.9a shows a peak at 580 nm which is equivalent to an energy level of 2.14 eV. Since this energy level is close to the energy gap of 2.3 eV, calculated using the Kubelka-Munk analysis for the defect states, it can be concluded that this peak corresponds to the recombination of excited electrons at the defect state. To have an insight into the significance of these electron-hole recombination, Table 4.2 compares the PL intensity and PL wavelength of the HEO with those measured by the current authors for anatase $TiO_2$ and $BiVO_4$ (as two popular photocatalysts for $CO_2$ conversion [34-36]). It is obvious that the PL intensity of HEO is lower than that of anatase $TiO_2$ and $BiVO_2$, despite its high light absorbance which is an indication of large electron-hole production. The lower PL intensity suggests that the recombination in this HEO is not higher than $TiO_2$ and $BiVO_2$, provided that the heat energy generation through the electron-hole recombination is considered identical for the three oxides.

Evaluation of PL decay intensity versus time, as shown in Fig. 4.9b, indicates that the PL decay of the HEO follows an exponential equation.

$$I(t) = A_1 \exp\left(-\frac{t}{\tau_1}\right) + A_2 \exp\left(-\frac{t}{\tau_2}\right) \quad (4.1)$$

where, $I(t)$, $A_1$, $A_2$, $\tau_1$ and $\tau_2$ are PL decay intensity at time $t$, amplitude of the first exponential function, amplitude of the second exponential function, fast decay time and slow decay time, respectively. Analysis of data in Fig. 4.9b suggests the values of 1.53 and 10.39 ns for $\tau_1$ and $\tau_2$, respectively. Here, the following equation can be used to estimate the average lifetime, $\tau_{ave}$ [37].

$$\tau_{ave} = \frac{A_1\tau_1^2 + A_2\tau_2^2}{A_1\tau_1 + A_1\tau_1} \quad (4.2)$$

Table 4.2 compares the average lifetime for the HEO with those for anatase $TiO_2$ and $BiVO_4$. The average lifetime for the HEO is 10.5 ns which is close to the lifetime of $TiO_2$ anatase (10.7 ns). Low recombination intensity of the HEO, measured by steady-state PL spectroscopy, and an appropriate electron lifetime close to $TiO_2$ anatase, show that the exited electrons on the surface of this material can be active for appropriate time to take part in photocatalytic reaction before recombination with holes. One reason for the appropriate charge carrier lifetime and low-intensity recombination for this HEO can be the presence of oxygen vacancies on the surface [38,39].

Prescence of oxygen vacancies, which was suggested by the orange color of sample in Fig. 4.1c, XPS spectroscopy in Fig. 4.4 and UV-vis spectroscopy in Fig. 4.8a, was examined further by EPR spectroscopy, as shown in Fig. 4.9c. Two symmetric hump peaks with a $g$ factor of 2.15 appear which may be due to the oxygen vacancies, as reported in some oxides such as $Nb_2O_5$ [40]. It should be noted that the oxygen vacancies on the surface can act as active sites for electron-hole separation and photocatalytic reaction [36]. Moreover, it was shown that the surface oxygen vacancies have a direct effect on photocatalytic CO production rate: surface oxygen vacancies can absorb $CO_2$ and contribute to breaking the C=O bonds to produce CO [36].

Table 4.2. PL wavelength and intensity, fitted parameters of PL decay spectra and photocurrent density for high-entropy oxide in comparison with anatase $TiO_2$ and $BiVO_4$ photocatalysts.

| **PL** | | Wavelength (nm) | | Intensity (cps) | |
|---|---|---|---|---|---|
| $TiZrNbHfTaO_{11}$ | | 580 | | 190 | |
| Anatase $TiO_2$ | | 510 | | 12300 | |
| $BiVO_4$ | | 640 | | 300 | |
| **PL Decay** | $\tau_1$ (ns) | $\tau_2$ (ns) | $A_1$ | $A_2$ | $\tau_{ave}$ (ns) |
| $TiZrNbHfTaO_{11}$ | 1.53 | 10.39 | 42.34 | 57.66 | 10.5 |
| Anatase $TiO_2$ | 1.24 | 11.46 | 41.98 | 58.02 | 10.7 |
| $BiVO_4$ | 2.17 | 14.90 | 56.56 | 43.44 | 12.9 |
| **Photocurrent ($mA/m^2$)** | | Cycle 1 | Cycle 2 | Cycle 3 | Cycle 4 |
| $TiZrNbHfTaO_{11}$ | | 9.6 | 8.9 | 8.4 | 8.2 |
| Anatase $TiO_2$ | | 43.5 | 32.2 | 27.9 | 25.2 |
| $BiVO_4$ | | 18.6 | 17.1 | 17.0 | 16.7 |

Fig. 4.9d shows photocurrent measurement on HEO thin film. The material successfully generates photocurrent, although its photocurrent density decreases during the time due to the accumulation of holes with positive charge on the surface. Table 4.2 compares the photocurrent density of the HEO with that of reference anatase $TiO_2$ and $BiVO_4$ for the first four cycles. It should be noted that the quantitative comparison of the photocurrent density of these three materials should be conducted by care due to the technical limits in making dense films with good FTO-oxide bonding by annealing at 473 K. The photocurrent density of HEO is apparently lower than that of the reference oxides. Despite the low photocurrent density of HEO, photocurrent generation on this material indicates that the exited electrons can have enough lifetime to separate from the surface of material and take part in the photocurrent generation. The generation of photocurrent is a positive sign for possible photocatalytic activity of this HEO, as discussed earlier for other photocatalysts [27].

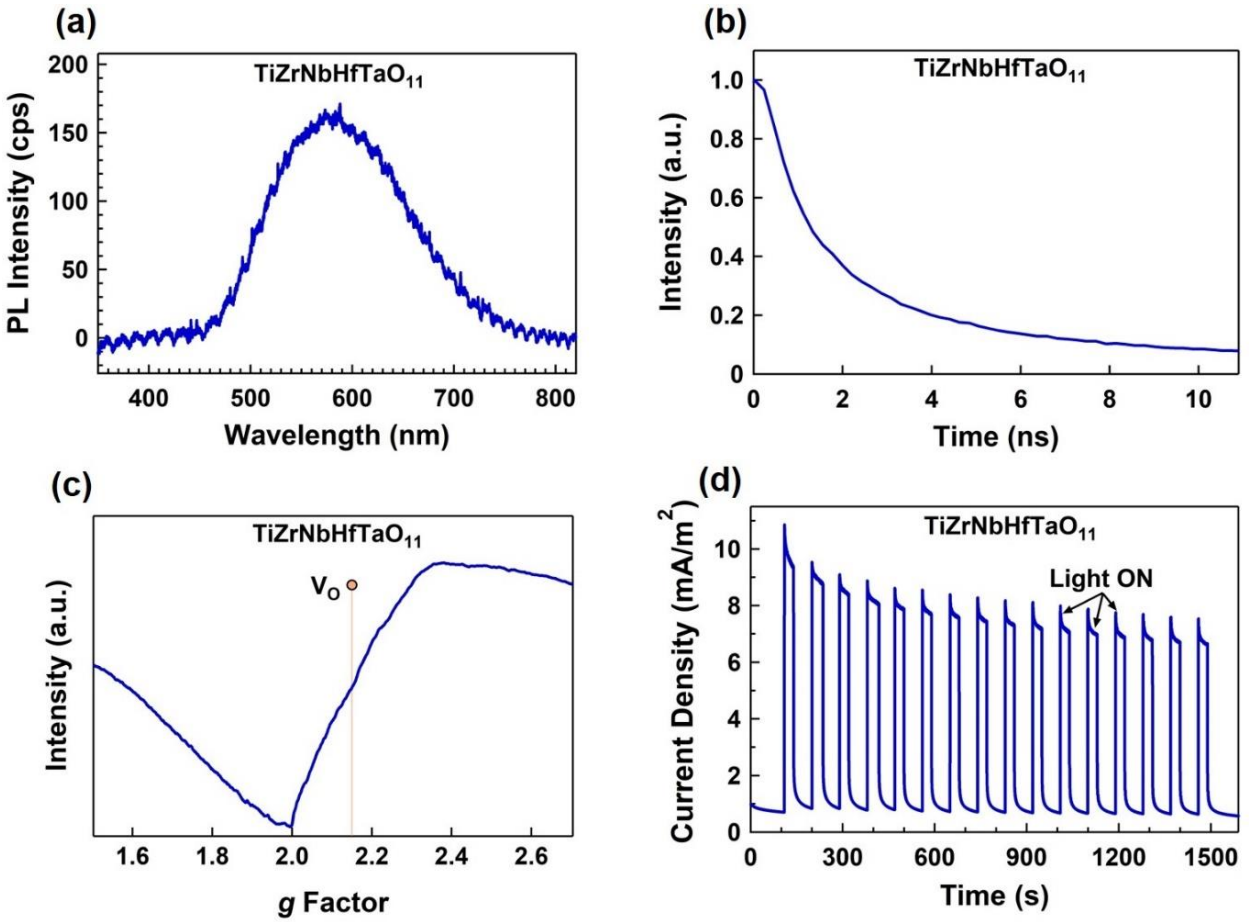


Fig. 4.9. (a) Steady-state PL emission, (b) time-resolved PL decay, (c) EPR spectra and (d) photocurrent generation for high-entropy oxide.

### *4.3.4. Photocatalytic activity*

Photocatalytic activity of HEO for $CO_2$ conversion is summarized in Fig. 4.10. As shown in Fig. 4.10a and b, the HEO could successfully produce both CO and $H_2$ under the full arc emission of high-pressure Hg lamp without any co-catalyst addition, despite its low specific surface area as 0.66 $m^2/g$ (the error bar of gas amount measurement for three repeated tests was lower than 10%). Independent synthesis of the HEO material and repeating the photocatalytic test, as indicated as Sample #2 in Fig. 4.10a, also confirm the high activity of this material for photocatalytic $CO_2$ conversion with a reasonably constant CO and $H_2$ production rate within an extended irradiation time of 10 h. The amount of CO production is higher and the amount of $H_2$ production is lower for Sample #2 compared to Sample #1, suggesting that the activity of this HEO can be still improved by modification of the synthesis method. Two points should be noted here.

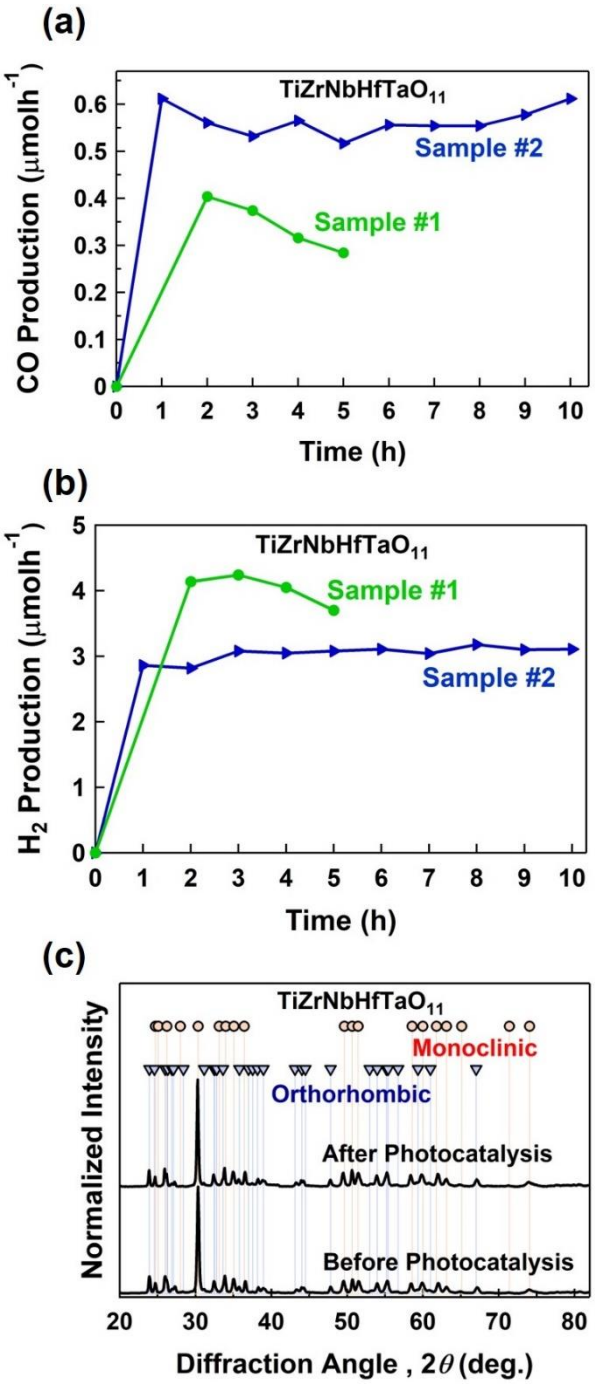


Fig. 4.10. Photocatalytic activity of high-entropy oxide for $CO_2$ conversion and $H_2O$ decomposition. (a) CO production rate versus time, (b) $H_2$ production rate versus time, and (c) XRD pattern before and after photocatalytic test.

First, CO and $H_2$ were the only reaction products within the detection limits of analyses and no other products including methane could be detected. Second, blank tests confirmed that no CO and $H_2$ are produced by (i) $CO_2$ injection in the presence of HEO under the dark condition for 2 h, (ii) Ar injection in the presence of HEO under the light irradiation for 1 h, and (iii) $CO_2$ injection without the presence of HEO under the light irradiation for 5 h. The stability of HEO, examined by XRD analysis after the photocatalytic test, is shown in Fig. 4.10c, indicating that the crystal structure of the HEO is stable after photocatalytic test. The stability of HEOs, which was also reported for other applications such thermal barrier coatings [9,10], magnetic components [11,12], dielectric components [13,14], Li-ion batteries [15,16], Li-S batteries [17], Zn-air batteries [18], catalysts [19,20] and electrocatalysts [21], is usually due to their low Gibbs free energy resulting from their high entropy [1,2].

### 4.4. Discussion

Three issues need to be discussed in detail here: (i) comparison of photocatalytic activity of the HEO with available photocatalysts, (ii) factors influencing the photocatalytic activity of the HEO, and (iii) mechanism of $CO_2$ conversion on the HEO photocatalyst.

Although the current results confirm the potential of HEOs as a new family of photocatalysts for $CO_2$ conversion, their activity should be compared with other photocatalysts to have an insight into their significance. To understand this issue, photocatalytic $CO_2$ conversion activity of the HEO with a specific surface area of 0.66 $m^2/g$ was compared with anatase $TiO_2$ (99.8%), $BiVO_4$ (99.9%) and P25 $TiO_2$ (99.5%) with the surface areas of 10.2, 0.3 and 38.7 $m^2/g$, respectively. Since various parameter such as catalyst concentration, temperature, reactor type, light source type and light intensity can influence the CO production rate, photocatalytic activity of these materials were compared in the same conditions. Fig. 4.11 shows the activity of these materials per 1 g of catalyst. The CO production rate for HEO is significantly higher than anatase $TiO_2$ and $BiVO_4$ which are some of the most popular photocatalysts for photocatalytic $CO_2$ conversion. Moreover, the CO and $H_2$ production rate on this HEO is comparable with P25 $TiO_2$ as a benchmark photocatalyst, although the surface area of current HEO is 60 times smaller than that of P25 $TiO_2$. It should be noted that the quantity of $H_2$ production on anatase $TiO_2$ and $BiVO_4$ was not within the detection limits of gas chromatograph. To get more insight on the significance of photocatalytic $CO_2$ conversion on this HEO, its activity was compared with some reported data

in the literature [5,41,42-50]. Although the experiments in the literature are not conducted under a consistent and standard condition, it is still useful to have a comparison. As given in Table 4.3, the amount of CO production rate varies in a wide range of 0.12-10.16 $\mu molh^{-1}\ g^{-1}$. The average CO production for HEO is 4.64±0.30 $\mu molh^{-1}g^{-1}$ which is higher than many of the reported values in Table 4.3.

The reason for high CO production rate on current HEO can be attributed to various factors: the presence of lattice defects such as oxygen vacancies which can act as activation sites [5,6], the presence of five cations which can enhance the activity by straining effect [7,8], appropriate electronic structure which satisfy most of the reactions for $CO_2$ conversion and water splitting [32,33], and appropriate lifetime of charge carriers to participate in photocatalytic reaction due to the defective nature of HEOs [38,39]. Moreover, the presence of two phases can improve the charge carrier separation through interfaces and enhance the photocatalytic activity [27,28]. The presence of several cations in the HEO can also produce hybridized orbitals with higher activity for chemical reactions [1,2]. To further enhance the efficiency of current HEO for photocatalytic $CO_2$ conversion, future works are required to enhance its specific surface area by improving the synthesis or crushing techniques.

Table 4.3. Summary of some reported photocatalytic $CO_2$ conversion rates in literature in comparison with results of current study.

| **Photocatalyst** | **Light Source** | **CO Production ($\mu molh^{-1}g^{-1}$)** | **References** |
|---|---|---|---|
| $TiO_2$ Nanosheet -CN | 150 W Xe lamp | 2.04 | [41] |
| $TiO_2$- Graphitic carbon | 300 W Xe lamp | 10.16 | [43] |
| $TiO_2$ nanosheets exposed {001} facet | 2 *18W Hg lamps | 0.12 | [44] |
| $TiO_2$ - Hydrogenated $CoO_x$ | 150W UV lamp | 1.24 | [45] |
| $TiO_2$ 3D Ordered Microporous - Pd | 300 W Xe lamp | 3.9 | [46] |
| $C_3N_4$ by Thermal Condensation | 350 W Xe lamp | 4.83 | [5] |
| $Cd_{1-x}Zn_xS$ | 100 W LED plate | 2.9 | [47] |
| BiOI | 300 W Xe lamp | 4.1 | [48] |
| $xCu_2O$-$Zn_{2-2x}Cr$ | 200-W Hg-Xe lamp | 2.5 | [42] |
| $CeO_{2-x}$ | 300 W Xe lamp | 1.65 | [49] |
| $Cu_2O/RuO_x$ | 150 W Xe lamp | 0.88 | [50] |
| $TiO_2$ Anatase | 400 W Hg Lamp | 0.58±0.12 | This Work |
| $BiVO_4$ | 400 W Hg Lamp | 2.16±0.21 | This Work |
| $TiO_2$ P25 | 400 W Hg Lamp | 4.63±0.33 | This Work |
| $TiZrNbHfTaO_{11}$ | 400 W Hg Lamp | 4.64±0.30 | This Work |

Regarding the third issue, three main mechanisms for photocatalytic $CO_2$ reduction have been suggested, as summarized in Table 4.4: carbene pathway, formaldehyde pathway and glyoxal pathway [35,36]. The behavior of current HEO is similar to P25 $TiO_2$, suggesting that both materials probably follow the same pathway. Although even for $TiO_2$ with different impurities and lattice defects, there are still significant arguments regarding the $CO_2$ reduction pathways, it is still possible to discuss about the possible mechanisms for current HEO photocatalyst. The nonappearance of HCOOH, $CH_3OH$ and $CH_4$ in the gas and liquid phases within the detection limits of analyses suggests that the formaldehyde pathway may not be the major mechanism [35,36]. The nonappearance of HCOOH and $CH_4$ also indicates that the glyoxal pathway may not be the major mechanism [35,36].

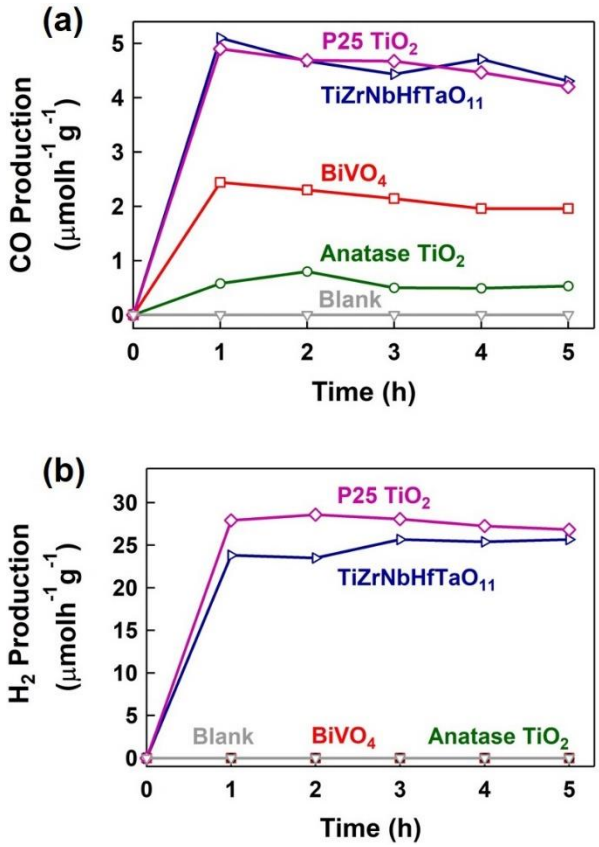


Fig. 4.11. High efficiency of high-entropy oxide compared with $TiO_2$ and $BiVO_4$ for photocatalytic $CO_2$ conversion. (a) CO production rate and (b) $H_2$ production rate versus time.

The production of CO suggests that the carbene pathway is probably the major mechanism. However, the absence of $CH_4$ and the presence of $H_2$, which is similar to the behavior of P25 $TiO_2$

in this study, indicates that the carbene pathway possibly stops at some intermediate stages due to the formation of $H_2$ gas [51]. The absence of $CH_4$ can also be explained by the defective structure of HEO. Since the HEO material has oxygen vacancies as surface defects, $CO_2$ in connection with $H_2O$ as a Lewis acid tends to adsorb on oxygen vacancies [51]. This adsorption degrades C=O bonding and produce $^{\bullet}CO$ radicals and consequently generates CO gas [36]. Compared with $CO_2$, the generated CO has lower tendency to be adsorbed on the surface defects [51], and thus, the carbene pathway does no continue to produce detectable quantity of $CH_4$. For $TiO_2$, it was also reported that although the $CH_4$ formation in the carbene pathway is thermodynamically more favorable than CO and $H_2$ formation, the formation of $CH_4$ is kinetically more difficult because it needs higher numbers of electrons and protons [52].

Table 4.4. Main mechanisms for $CO_2$ photocatalytic reduction pathway [35].

| **Carbene Pathway** | **Formaldehyde Pathway** | **Glyoxal Pathway** |
|---|---|---|
| (1) $CO_2 + e^- \rightarrow CO_2^{\bullet -}$ | (1) $CO_2 + e^- \rightarrow CO_2^{\bullet -}$ | (1) $CO_2 + e^- \rightarrow CO_2^{\bullet -}$ |
| (2) $CO_2^{\bullet -} + e^- + H^+ \rightarrow CO + OH^-$ | (2) $CO_2^{\bullet -} + H^+ \rightarrow {}^{\bullet}COOH$ | (2) $CO_2^{\bullet -} + e^- + H^+ \rightarrow CHOO^-$ |
| (3) $CO + e^- \rightarrow CO^{\bullet -}$ | (3) ${}^{\bullet}COOH + e^- + H^+ \rightarrow HCOOH$ | (3) $CHOO^- + H^+ \rightarrow HCOOH$ |
| (4) $CO^{\bullet -} + e^- + H^+ \rightarrow C + OH^-$ | (4) $HCOOH + e^- + H^+ \rightarrow H_3OOC^{\bullet}$ | (4) $HCOOH + e^- \rightarrow HOC^{\bullet}$ |
| (5) $C + e^- + H^+ \rightarrow CH^{\bullet}$ | (5) $HCOOH_2^{\bullet} + e^- + H^+ \rightarrow HCOH + H_2O$ | (5) $HOC^{\bullet} + OH^- \rightarrow C_2H_2O_2$ |
| (6) $CH^{\bullet} + e^- + H^+ \rightarrow CH_2$ | (6) $HCOH + e^- \rightarrow H_2C^{\bullet}O^-$ | (6) $C_2H_2O_2 + e^- + H^+ \rightarrow H_3O_2C_2^{\bullet}$ |
| (7) $CH_2 + e^- + H^+ \rightarrow CH_3^{\bullet}$ | (7) $H_2C^{\bullet}O^- + H^+ \rightarrow H_2OHC^{\bullet}$ | (7) $H_3O_2C_2^{\bullet} + e^- + H^+ \rightarrow C_2H_4O_2$ |
| (8) $CH_3^{\bullet} + e^- + H^+ \rightarrow CH_4$ | (8) $H_2OHC^{\bullet} + e^- + H^+ \rightarrow CH_3OH$ | (8) $C_2H_4O_2 + e^- + H^+ \rightarrow H_3OC_2^{\bullet} + H_2O$ |
| (9) $CH_3^{\bullet} + OH^- \rightarrow CH_3OH$ | (9) $CH_3OH + e^- + H^+ \rightarrow {}^{\bullet}CH_3 + H_2O$ | (9) $H_3OC_2^{\bullet} + e^- + H^+ \rightarrow C_2H_4O$ |
| | (10) ${}^{\bullet}CH_3 + e^- + H^+ \rightarrow CH_4$ | (10) $C_2H_4O + h^+ \rightarrow H_3OC_2^{\bullet} + H^+$ |
| | | (11) $H_3OC_2^{\bullet} \rightarrow CH_3^{\bullet} + CO$ |
| | | (12) $CH_3^{\bullet} + e^- + H^+ \rightarrow CH_4$ |

Taken altogether, this study introduces HEOs as active photocatalysts for $CO_2$ conversion, and this opens a path to explore numerous photocatalysts by considering the state-of-art on engineering of catalysts for $CO_2$ photoreduction [53]. Despite high activity of current HEO, future studies are required to clarify the exact $CO_2$ conversion mechanism on this new family of materials. It should be noted that although the material in this study was synthesized by a two-step high-pressure mechanical alloying and high-temperature oxidation, other methods developed earlier for the synthesis of high-entropy ceramics [54] can be used in the future to synthesize powders with high specific surface area and low economical cost. Moreover, since earlier studies showed that

the semiconductor photocatalysts with $CO_2$ conversion capability can have good activity for degradation of organic pollutants as well [55,56], it is expected that the photocatalytic activity of HEOs is not limited to CO and $H_2$ production.

### 4.5. Conclusion

A high-entropy oxide with a general composition of $TiZrNbHfTaO_{11}$ was synthesized and used for photocatalytic $CO_2$ conversion. Due to appropriate electronic band structure, good charge carrier lifetime and a defective and strained dual-phase structure, the material acted as a photocatalyst for $CO_2$ to CO conversion and $H_2O$ to $H_2$ production without addition of any co-catalyst. The photocatalytic activity of this oxide was better than well-known anatase $TiO_2$ and $BiVO_4$ photocatalysts and comparable with P25 $TiO_2$ as a benchmark photocatalyst, suggesting high-entropy oxides as a new family of photocatalysts for $CO_2$ conversion.

### References


[1] C. Oses, C. Toher, S. Curtarolo, High-entropy ceramics, Nat. Rev. Mater. 5 (2020) 295-309.

[2] A.J. Wright, Q. Wang, C. Huang, A. Nieto, R. Chen, J. Luo, From high-entropy ceramics to compositionally-complex ceramics: a case study of fluorite oxides, J. Eur. Ceram. Soc. 40 (2020) 2120-2129.

[3] H. Chen, K. Jie, C.J. Jafta, Z. Yang, S. Yao, M. Liu, Z. Zhang, J. Liu, M. Chi, J. Fu, S. Dai, An ultrastable heterostructured oxide catalyst based on high-entropy materials: a new strategy toward catalyst stabilization via synergistic interfacial interaction, Appl. Catal. B 276 (2020) 119155.

[4] H. Chen, J. Fu, P. Zhang, H. Peng, C.W. Abney, K. Jie, X. Liu, M. Chi, S. Dai, Entropy-stabilized metal oxide solid solutions as CO oxidation catalysts with high-temperature stability, J. Mater. Chem. A 6 (2018) 11129-11133.

[5] P. Xia, M. Antonietti, B. Zhu, T. Heil, J. Yu, S. Cao, Designing defective crystalline carbon nitride to enable selective $CO_2$ photoreduction in the gas phase, Adv. Funct. Mater. 29 (2019) 1900093.

[6] J.J. Li, M. Zhang, B. Weng, X. Chen, J. Chen, H.P. Jia, Oxygen vacancies mediated charge separation and collection in Pt/$WO_3$ nanosheets for enhanced photocatalytic performance, Appl. Surf. Sci. 507 (2020) 145133.

[7] Z. Liu, C. Menéndez, J. Shenoy, J.N. Hart, C.C. Sorrell, C. Cazorl, Strain engineering of oxide thin films for photocatalytic applications, Nano Energy 72 (2020) 104732.

[8] J. Di, P. Song, C. Zhu, C. Chen, J. Xiong, M. Duan, R. Long, W. Zhou, M. Xu, L. Kang, B. Lin, D. Liu, S. Chen, C. Liu, H. Li, Y. Zhao, S. Li, Q. Yan, L. Song, Z. Liu, Strain-engineering of $Bi_2O_{17}Br_2$ nanotubes for boosting photocatalytic $CO_2$ reduction, ACS Mater. Lett. 2 (2020)1025–1032.

[9] J.L. Braun, C.M. Rost, M. Lim, A. Giri, D.H. Olson, G.N. Kotsonis, G. Stan, D.W. Brenner, J.P. Maria, P.E. Hopkins, Charge-induced disorder controls the thermal conductivity of entropy-stabilized oxides, Adv. Mater. 30 (2018) 1805004.

[10] A.J. Wright, C. Huang, M.J. Walock, A. Ghoshal, M. Murugan, J. Luo, Sand corrosion, thermal expansion, and ablation of medium-and high-entropy compositionally complex fluorite oxides, J. Am. Ceram. Soc. 104 (2021) 448-462.

[11] R. Witte, A. Sarkar, R. Kruk, B. Eggert, R.A. Brand, H. Wende, H. Hahn, High-entropy oxides: an emerging prospect for magnetic rare-earth transition metal perovskites, Phys. Rev. Mater. 3 (2019) 034406.

[12] A. Mao, H.Z. Xiang, Z.G. Zhang, K. Kuramoto, H. Zhang, Y. Jia, A new class of spinel high-entropy oxides with controllable magnetic properties, J. Magn. Magn. Mater. 497 (2020) 165884.

[13] A. Radoń, Ł. Hawełek, D. Łukowiec, J. Kubacki, P. Włodarczyk, Dielectric and electromagnetic interference shielding properties of high entropy (Zn,Fe,Ni,Mg,Cd)$Fe_2O_4$ ferrite, Sci. Rep. 9 (2019) 20078.

[14] S. Zhou, Y. Pu, Q. Zhang, R. Shi, X. Guo, W. Wang, J. Ji, T. Wei, T. Ouyang, Microstructure and dielectric properties of high entropy $Ba(Zr_{0.2}Ti_{0.2}Sn_{0.2}Hf_{0.2}Me_{0.2})O_3$ perovskite oxides, Ceram. Int. 46 (2020) 7430-7437.

[15] A. Sarkar, L. Velasco, D. Wang, Q. Wang, G. Talasila, L. de Biasi, C. Kübel, T. Brezesinski, S.S. Bhattacharya, H. Hahn, B. Breitung, High entropy oxides for reversible energy storage, Nat. Commun. 9 (2018) 3400.

[16] T.X. Nguyen, J. Patra, J.K. Chang, J.M. Ting, High entropy spinel oxide nanoparticles for superior lithiation-delithiation performance, J. Mater. Chem. A 8 (2020) 18963-18973.

[17] Y. Zheng, Y. Yi, M. Fan, H. Liu, X. Li, R. Zhang, M. Li, Z.-A. Qiao, A high-entropy metal oxide as chemical anchor of polysulfide for lithium-sulfur batteries, Energy Storage Mater. 23 (2019) 678-683.

[18] G. Fang, J. Gao, J. Lv, H. Jia, H. Li, W. Liu, G. Xie, Z. Chen, Y. Huang, Q. Yuan,X. Liu, X. Lin, S. Sun, H.J. Qiu, Multi-component nanoporous alloy/(oxy) hydroxide for bifunctional oxygen electrocatalysis and rechargeable Zn-air batteries, Appl. Catal. B 268 (2020) 118431.

[19] H. Chen, W. Lin, Z. Zhang, K. Jie, D.R. Mullins, X. Sang, S.-Z. Yang, C.J. Jafta, C.A. Bridges, X. Hu, Mechanochemical synthesis of high entropy oxide materials under ambient conditions: dispersion of catalysts via entropy maximization, ACS Mater. Lett. 1 (2019) 83-88.

[20] M.S. Lal, R. Sundara, High entropy oxides - a cost-effective catalyst for the growth of high yield carbon nanotubes and their energy applications, ACS Appl. Mater. Interfaces 11 (2019) 30846-30857.

[21] T.X. Nguyen, Y.C. Liao, C.C. Lin, Y.H. Su, J.M. Ting, Advanced high entropy perovskite oxide electrocatalyst for oxygen evolution reaction, Adv. Funct. Mater. 31 (2021) 2101632.

[22] P. Edalati, Q. Wang, H. Razavi-Khosroshahi, M. Fuji, T. Ishihara, K. Edalati, Photocatalytic hydrogen evolution on a high-entropy oxide, J. Mater. Chem. A 8 (2020) 3814-3821.

[23] P. Edalati, X.F. Shen, M. Watanabe, T. Ishihara, M. Arita, M. Fuji, K. Edalati, High-entropy oxynitride as a low-bandgap and stable photocatalyst for hydrogen production, J. Mater. Chem. A 9 (2021) 15076-15086.

[24] K. Edalati, Z. Horita, A review on high-pressure torsion (HPT) from 1935 to 1988, Mater. Sci. Eng. A 652 (2016) 325–352.

[25] K. Edalati, Review on recent advancements in severe plastic deformation of oxides by high-pressure torsion (HPT), Adv. Eng. Mater. 21 (2019) 1800272.

[26] J. Chastain, Handbook of X-ray Photoelectron Spectroscopy, Perkin-Elmer Corporation, Eden Prairie, MN, USA, 1992.

[27] S. Akrami, M. Watanabe, T.H. Ling, T. Ishihara, M. Arita, M. Fuji, K. Edalati, High-pressure $TiO_2$-II polymorph as an active photocatalyst for $CO_2$ to CO conversion, Appl. Catal. B 298 (2021) 120566.

[28] Z. Liu, C. Menéndez, J. Shenoy, J.N. Hart, C.C. Sorrell, C. Cazorl, Strain engineering of oxide thin films for photocatalytic applications, Nano Energy 72 (2020) 104732.

[29] L. Ran, J. Hou, S. Cao, Z. Li, Y. Zhang, Y. Wu, B. Zhang, P. Zhai, L. Sun, Defect engineering of photocatalysts for solar energy conversion, Sol. RRL 4 (2020) 1900487.

[30] M. R. Hoffmann, S. T. Martin, W. Choi and D. W. Bahnemann, Environmental applications of semiconductor photocatalysis, Chem. Rev. 95 (1995) 69–96.

[31] K. Maeda and K. Domen, New non-oxide photocatalysts designed for overall water splitting under visible light, J. Phys. Chem. C, 111 (2007) 7851–7861.

[32] P. Xia, M. Antonietti, B. Zhu, T. Heil, J. Yu, S. Cao, Designing defective crystalline carbon nitride to enable selective $CO_2$ photoreduction in the gas phase, Adv. Funct. Mater. 29 (2019) 1900093.

[33] J.J. Li, M. Zhang, B. Weng, X. Chen, J. Chen, H.P. Jia, Oxygen vacancies mediated charge separation and collection in $Pt/WO_3$ nanosheets for enhanced photocatalytic performance, Appl. Surf. Sci. 507 (2020) 145133.

[34] A.J. Morris, G.J. Meyer, E. Fujita, Molecular approaches to the photocatalytic reduction of carbon dioxide for solar fuels, Acc. Chem. Res. 42 (2009) 1983-1994.

[35] S.N. Habisreutinger, L. Schmidt-Mende, J.K. Stolarczyk, Photocatalytic reduction of $CO_2$ on $TiO_2$ and other semiconductors, Angew. Chem. Int. Ed. 52 (2013) 7372-7408.

[36] K. Wang, J. Lu, Y. Lu, C.H. Lau, Y. Zheng, X. Fan, Unravelling the C-C coupling in $CO_2$ photocatalytic reduction with $H_2O$ on $Au/TiO_{2-x}$: combination of plasmonic excitation and oxygen vacancy, Appl. Catal. B 292 (2021) 120147.

[37] Z. Zhang, K. Liu, Z. Feng, Y. Bao, B. Dong, Hierarchical sheet-on-sheet $ZnIn_2S_4$/g-$C_3N_4$ heterostructure with highly efficient photocatalytic $H_2$ production based on photoinduced interfacial charge transfer, Sci. Rep. 6 (2016) 19221.

[38] X.H. Wang, J.G. Li, H. Kamiyama, M. Katada, N. Ohashi, Y. Moriyoshi, T. J. Ishigaki, Pyrogenic iron (III)-doped $TiO_2$ nanopowders synthesized in RF thermal plasma: phase formation, defect structure, band gap, and magnetic properties, J. Am. Chem. Soc. 127 (2005) 10982–10990.

[39] I. Nakamura, N. Negishi, S. Kutsuna, T. Ihara, S. Sugihara, K.J. Takeuchi, Role of oxygen vacancy in the plasma-treated $TiO_2$ photocatalyst with visible light activity for NO removal, J. Mol. Catal. A 161 (2000) 205–212.

[40] M. Li, X. He, Y. Zeng, M. Chen, Z. Zhang, H. Yang, P. Fang, X. Lu, Y. Tong, Solar-microbial hybrid device based on oxygen-deficient niobium pentoxide anodes for sustainable hydrogen production, Chem. Sci. 6 (2015) 6799.

[41] J. Di, P. Song, C. Zhu, C. Chen, J. Xiong, M. Duan, R. Long, W. Zhou, M. Xu, L. Kang, B. Lin, D. Liu, S. Chen, C. Liu, H. Li, Y. Zhao, S. Li, Q. Yan, L. Song, Z. Liu, Strain-engineering of $Bi_2O_{17}Br_2$ nanotubes for boosting photocatalytic $CO_2$ reduction, ACS Mater. Lett. 2 (2020)1025–1032.

[42] H. Jiang, K. Katsumata, J. Hong, A. Yamaguchi, K. Nakata, C. Terashima, N. Matsushita, M. Miyauchi, A. Fujishima, Photocatalytic reduction of $CO_2$ on $Cu_2O$-loaded Zn-Cr layered double hydroxides, Appl. Catal. B 224 (2018) 783-790.

[43] Y. Wang, Y. Chen, Y. Zuo, F. Wang, J. Yao, B. Li, S. Kang, X. Li, L. Cui, Hierarchically mesostructured $TiO_2$/graphitic carbon composite as a new efficient photocatalyst for the reduction of $CO_2$ under simulated solar irradiation, Catal. Sci. Technol. 3 (2013) 3286-3291.

[44] Z. He, L. Wen, D. Wang, Y. Xue, Q. Lu, C. Wu, J. Chen, S. Song, Photocatalytic reduction of $CO_2$ in aqueous solution on surface-fluorinated anatase $TiO_2$ nanosheets with exposed {001} facets, Energy Fuels. 28 (2014) 3982-3993.

[45] Y. Li, C. Wang, M. Song, D. Li, X. Zhang, Y. Liu, $TiO_{2-x}/CoO_x$ photocatalyst sparkles in photothermocatalytic reduction of $CO_2$ with $H_2O$ steam, Appl. Catal. B 243 (2019) 760–770.

[46] J. Jiao, Y. Wei, Y. Zhao, Z. Zhao, A. Duan, J. Liu, Y. Pang, J. Li, G. Jiang, Y. Wang, AuPd/3DOM-$TiO_2$ catalysts for photocatalytic reduction of $CO_2$: High efficient separation of photogenerated charge carriers, Appl. Catal. B 209 (2017) 228-239.

[47] E.A. Kozlova, M.N. Lyulyukin, D.V. Markovskaya, D.S. Selishchev, S.V. Cherepanova, D.V. Kozlov, Synthesis of $Cd_{1-x}Zn_xS$ photocatalysts for gas-phase $CO_2$ reduction under visible light, Photochem. Photobiol. Sci. 18 (2019) 871-877.

[48] L. Ye, H. Wang, X. Jin, Y. Su, D. Wang, H. Xie, X. Liu, X. Liu, Synthesis of olive-green fewlayered BiOI for efficient photoreduction of $CO_2$ into solar fuels under visible/near-infrared light, Sol. Energy Mater. Sol. Cells 144 (2016) 732-739.

[49] T. Ye, W. Huang, L. Zeng, M. Li, J. Shi, $CeO_{2-x}$ platelet from monometallic cerium layered double hydroxides and its photocatalytic reduction of $CO_2$, Appl. Catal. B 210 (2017) 141-148.

[50] E. Pastor, F. Pesci, A. Reynal, A. Handoko, M. Guo, X. An, A. Cowan, D. Klug, J. Durrant, J. Tang, Interfacial charge separation in $Cu_2O/RuO_x$ as a visible light driven $CO_2$ reduction catalyst, Phys. Chem. Chem. Phys. 16 (2014) 5922-5926.

[51] K. Wang, J. Lu, Y. Lu, C.H. Lau, Y. Zheng, X. Fan, Unravelling the C-C coupling in $CO_2$ photocatalytic reduction with $H_2O$ on $Au/TiO_{2-x}$: combination of plasmonic excitation and oxygen vacancy, Appl. Catal. B 292 (2021), 120147.

[52] L.Y. Lin, S. Kavadiya, X. He, W.N. Wang, B.B. Karakocak, Y.C. Lin, M.Y. Berezin, P. Biswas, Engineering stable Pt nanoparticles and oxygen vacancies on defective $TiO_2$ via introducing strong electronic metal-support interaction for efficient $CO_2$ photoreduction, Chem. Eng. J. 389 (2020), 123450.

[53] S. Wang, X. Han, Y. Zhang, N. Tian, T. Ma, H. Huang, Inside-and-out semiconductor engineering for $CO_2$ photoreduction: from recent advances to new trends, Small Struct. 2 (2021) 2000061.

[54] S. Akrami, P. Edalati, K. Edalati, M. Fuji, High-entropy ceramics: review of principles, production and applications, Mater. Sci. Eng. R 146 (2021) 100644.

[55] F.Y. Liu, Y.M. Dai, F.H. Chen, C.C. Chen, Lead bismuth oxybromide/graphene oxide: synthesis, characterization, and photocatalytic activity for removal of carbon dioxide, crystal violet dye, and 2-hydroxybenzoic acid, J. Colloid. Interface Sci. 562 (2020) 112-124.

[56] H.L. Chen, F.Y. Liu, X. Xiao, J. Hu, B. Gao, D. Zou, C.C. Chen, Visible-light-driven photocatalysis of carbon dioxide and organic pollutants by $MFeO_2$ (M = Li, Na, or K), J. Colloid. Interface Sci. 601 (2021) 758-772.

# Chapter 5. Significant $CO_2$ photoreduction on a high-entropy oxynitride

## 5.1. Introduction

Oxide photocatalysts such as $TiO_2$ [1,2] are the most common photocatalysts with high stability for $CO_2$ photoreduction application, but they have large bandgaps such as 3.1 eV for $TiO_2$ [1,2]. In contrast, there are some reports on photocatalytic activity of nitrides such as TaN [3] and $C_3N_4$ [4] for $CO_2$ conversion which have lower bandgaps compared to oxides, but nitrides are not chemically so stable [3,4]. To solve the problem of oxide and nitride photocatalysts in terms of large bandgap and low stability, respectively, oxynitrides were recommended as low bandgap and highly stable catalysts for photocatalysis [5]. Oxynitrides have been widely used for photocatalytic water splitting; however, only limited oxynitrides such as $\alpha$-$Fe_2O_3$/$LaTiO_2N$ [6] and TaON [7,8] were used for photocatalytic $CO_2$ conversion. Significant electron-hole recombination, sluggish kinetics, the low tendency for $CO_2$ adsorption and relatively low stability in the co-presence of $CO_2$ and water are some reasons for limited application of metal oxynitrides for photocatalytic $CO_2$ conversion [6,9]. Therefore, introducing a strategy to solve all or some of these problems is a key issue in using the benefits of oxynitrides for $CO_2$ conversion. Simultaneous addition of several principal elements and production of high-entropy oxynitride ceramics can be an effective strategy, although there have been few attempts in this regard. A combination of the perception of metal oxynitrides as low bandgap photocatalysts and high-entropy ceramics as highly stable materials can be a new strategy to expand the application of oxynitrides for photocatalytic $CO_2$ conversion. Although high-entropy oxynitrides (HEONs) were successfully synthesized in a few studies [10,11], there are no reports on the photocatalytic performance of HEONs for $CO_2$ photoreduction.

In this chapter, a two-phase $TiZrNbHfTaO_6N_3$ was synthesized as the first HEON for photocatalytic $CO_2$ conversion by high-pressure torsion mechanical alloying [12] and subsequent oxidation and nitriding. The HEON showed better light absorbance, lower charge carrier recombination rate, higher $CO_2$ adsorbance and larger photocatalytic $CO_2$ conversion compared to relevant HEO ($TiZrNbHfTaO_{11}$) and benchmark photocatalyst P25 $TiO_2$. Moreover, the activity of the HEON was higher than almost all photocatalysts developed in the literature for $CO_2$

photoreduction. These findings open a path to develop new high-entropy photocatalysts with significant efficiency for $CO_2$ photoreduction.

### 5.2. Experimental procedures

Despite various synthesis methods reported in the literature to produce HEOs [13-27] and HENs [13,14,28-30], the HEON was fabricated using a three-step synthesis method for this study [33]: (i) severe plastic deformation through the high-pressure torsion (HPT) method for alloying pure elemental powders [12,31], (ii) oxidation at elevated temperature and (iii) nitriding at elevated temperature. First, titanium (99.9%), zirconium (95.0%), niobium (99.9%), hafnium (99.5%) and tantalum (99.9%) powders with the same molar fraction of 0.2 were dispersed in acetone, mixed using ultrasonic and dried in air. About 700 mg of powder mixture was compacted into a 10 mm diameter disc under a pressure of 0.4 GPa and further proceeded by HPT under 6 GPa at room temperature using a rotation rate of one turn per minute for 100 turns to achieve a single-phase (body-centered cubic, BCC) alloy. Second, the HPT-processed high-entropy alloy was crushed in a mortar and inserted into a furnace for 24 h under a hot (1373 K) air atmosphere to generate the HEO, $TiZrNbHfTaO_{11}$ with dual monoclinic (40 wt%) and orthorhombic (60 wt%) structures. Third, the HEO was processed by nitriding in ammonia at 1373 K for 7 h using a heating rate of 20 $Kmin^{-1}$ with an $NH_3$ flow of 150 $mLmin^{-1}$ to generate a two-phase (40 wt% monoclinic + 60 wt% face-centered cubic, FCC) HEON, $TiZrNbHfTaO_6N_3$. The fabricated HEON was characterized by different methods, as follows.

The crystallographic features were analyzed by X-ray diffraction (XRD) using a Cu Kα source having 0.1542 nm wavelength. Phase fractions and lattice parameters were measured by the Rietveld analysis in the PDXL software.

The composition was examined by dispersing the sample on a carbon tape and conducting energy-dispersive X-ray spectroscopy (EDS) in a scanning electron microscope (SEM) under 15 keV.

The microstructure was examined by dispersing the crushed sample on carbon grids and employing a transmission electron microscope (TEM) under 200 keV by taking high-resolution (HR) images and analyzing them by fast-Fourier transform (FFT). Moreover, the distribution of elements was examined by a scanning-transmission electron microscope (STEM) under 200 kV by taking high-angle annular dark-field (HAADF) micrographs and conducting EDS analysis.

X-ray photoelectron spectroscopy (XPS) was performed to determine the top of the valence band and the electronic state of each element using a Mg Kα source.

The absorbance of light, and band structure including the level of bandgap were evaluated by UV-vis diffuse reflectance spectroscopy (followed by Kubelka-Munk calculation) and X-ray/UV photoelectron spectroscopy (XPS and UPS). The valence band top was determined by the UPS and XPS analyses and the conduction band bottom was determined by subtracting the bandgap value from the valence band top.

The electron-hole recombination was evaluated by photoluminescence (PL) spectroscopy using a UV laser (325 nm wavelength).

Photocurrent measurement on thin films of the samples was performed using the full arc of a Xe lamp in a 1 M $Na_2SO_4$ electrolyte. The experiments were conducted in the potentiostatic amperometry mode during the time (180 s light ON and 180 s light OFF) using an electrochemical analyzer. The counter and reference electrodes were Pt wire and Ag/AgCl, respectively, and the external potential was 0.7 V vs. Ag/AgCl. To prepare the thin films, 5 mg of each sample was crushed in 0.2 mL ethanol, spread on the FTO glass (fluorine-doped tin oxide with 2.25 mm thickness and 15 × 25 $mm^2$ surface area), and annealed at 473K for 2 h.

Diffuse reflectance infrared Fourier transform (DRIFT) spectrometry was performed to understand the adsorbance mode of $CO_2$ on the surface of each photocatalyst. First, 50 mg of each sample was treated at 773 K for 1 h in an argon atmosphere. Then, argon was replaced by 100% $CO_2$ gas at 773 K and the samples were kept under this condition for 30 min. The samples were then cooled down to room temperature and the $CO_2$ gas was replaced with argon. After keeping the samples in argon for 30 min, the DRIFT spectroscopy was conducted.

$CO_2$ photoreduction was examined in a cylindrical-shaped quartz photoreactor with 858 mL inner volume and specifications described in detail earlier [27]. Light source was placed in a space inside the photoreactor and $CO_2$ flow entered the reactor from a gas cylinder by a hole on the top of the reactor. Outlet gas from the reactor partly entered a gas chromatograph for the gas analysis and mainly flew to a vent. For the photoreduction experiments, 100 mg of HEON photocatalyst were dispersed in a 500 mL solution of 1 M $NaHCO_3$ and pure water. $CO_2$ gas was injected into the mixture (3 $mLmin^{-1}$) and the mixture was continuously stirred by a magnetic stirrer. It should be noted that the temperature was kept constant at 288 K utilizing a water chiller. To be sure about the nonappearance of reaction products without irradiating the mixture, the experiments were first

performed for 2 h in dark conditions. Then the photocatalytic experiment was performed under irradiation of a 400 W high-pressure mercury lamp (HL400BH-8 of Sen Lights Corporation) with 0.5 $Wcm^{-2}$ light intensity without any filtration. The gas of the photoreactor was analyzed using gas chromatography (GC-8A of Shimadzu). The generation of $CH_4$ and CO was analyzed using a methanizer and flame-ionization detector. The generation of oxygen and hydrogen was analyzed using a thermal conductivity detector. A blank test was conducted without catalyst addition under light irradiation and $CO_2$ injection to confirm that no CO was produced from other sources in the experimental system. Another blank test was conducted with catalyst addition under light irradiation and argon injection to confirm that CO was not produced without $CO_2$ injection.

### 5.3. Results

Fig. 5.1a illustrates the XRD profile of HEON. The HEON has two cubic (Fm3m space group, $a$=$b$=$c$=0.459 nm; $\alpha$=$\beta$=$\gamma$=90°) and monoclinic (P21/c space group, $a$=0.512, $b$=0.517, $c$=0.530 nm; $\alpha$=$\gamma$=90°, $\beta$=99.2°) phases with 60 and 40 wt% fractions, respectively. Fig. 5.1b illustrates the EDS profile of the HEON. The EDS analysis suggests a general composition of $TiZrHfNbTaO_6N_3$ for the synthesized HEON. The presence of two phases should be due to the thermodynamics of the Ti-Zr-Hf-Nb-Ta-O-N system at the synthesis temperature. The existence of two phases can be beneficial for charge separation in photocatalysis because the phase boundaries can act as heterojunctions for charge carrier migrations [32,33]. Although first-principle electronic structure calculations are required to clarify the migration direction of charge carriers in this HEON, it is expected that photoexcited electrons in the conduction band of one phase with a higher energy level move to the conduction band of the other phase and exited holes transfer from the valence band of one phase with the lower energy level to the valence band of another phase [32,33].

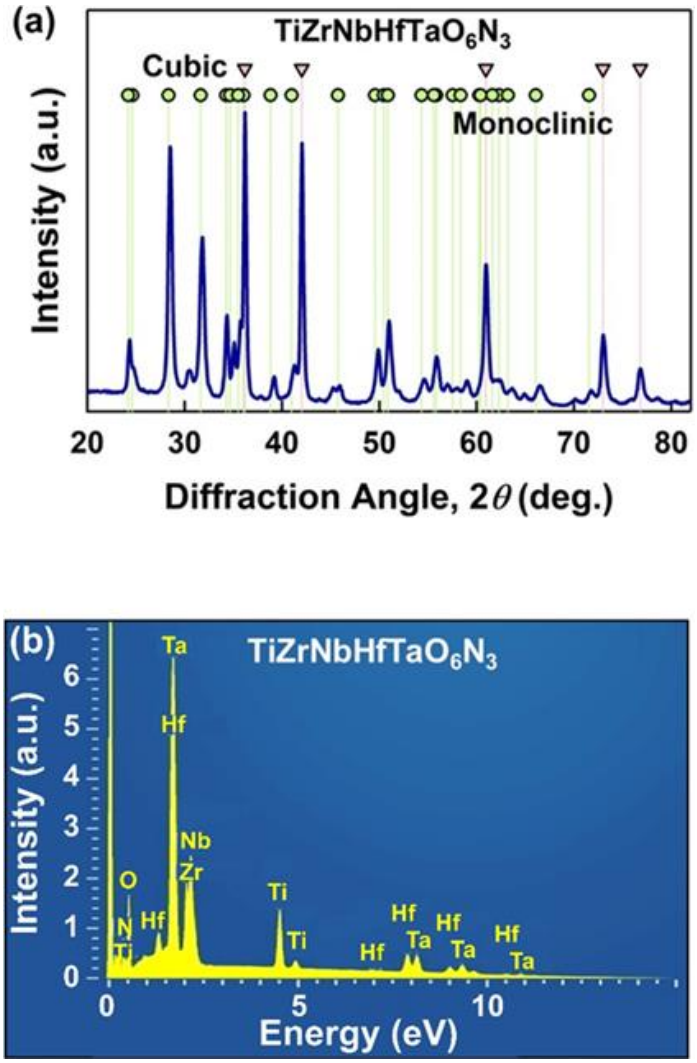


Fig. 5.1. Formation of high-entropy oxynitride with cubic and monoclinic phases and chemical composition of $TiZrNbHfTaO_6N_3$. a) XRD profile and b) EDS spectrum of high-entropy oxynitride.

The microstructure of the HEON is shown in Fig. 5.2 using different methods. Fig. 5.2a illustrates a micrograph taken by SEM, which indicates that the HEON contains large powders with an average size of 20 µm. Fig. 5.2b shows a HR image taken by TEM confirming the existence of nanocrystals of cubic and monoclinic phases which agrees with the XRD analysis. It also indicates the existence of a large fraction of interphases that can act as heterojunctions [34]. Fig. 5.2c illustrates a HAADF micrograph with relevant EDS mappings taken by STEM, showing a reasonably homogenous distribution of elements at the nanometer scale. Slight differences in the

distribution of metallic elements, oxygen and nitrogen should be mainly due to the presence of two phases. Here, it should be noted that XPS analyses, shown in Supporting Information Fig. S1, confirm that the main states of elements are $Ti^{4+}$, $Zr^{4+}$, $Hf^{4+}$, $Nb^{5+}$, $Ta^{5+}$, $O^{2-}$ and $N^{3-}$.

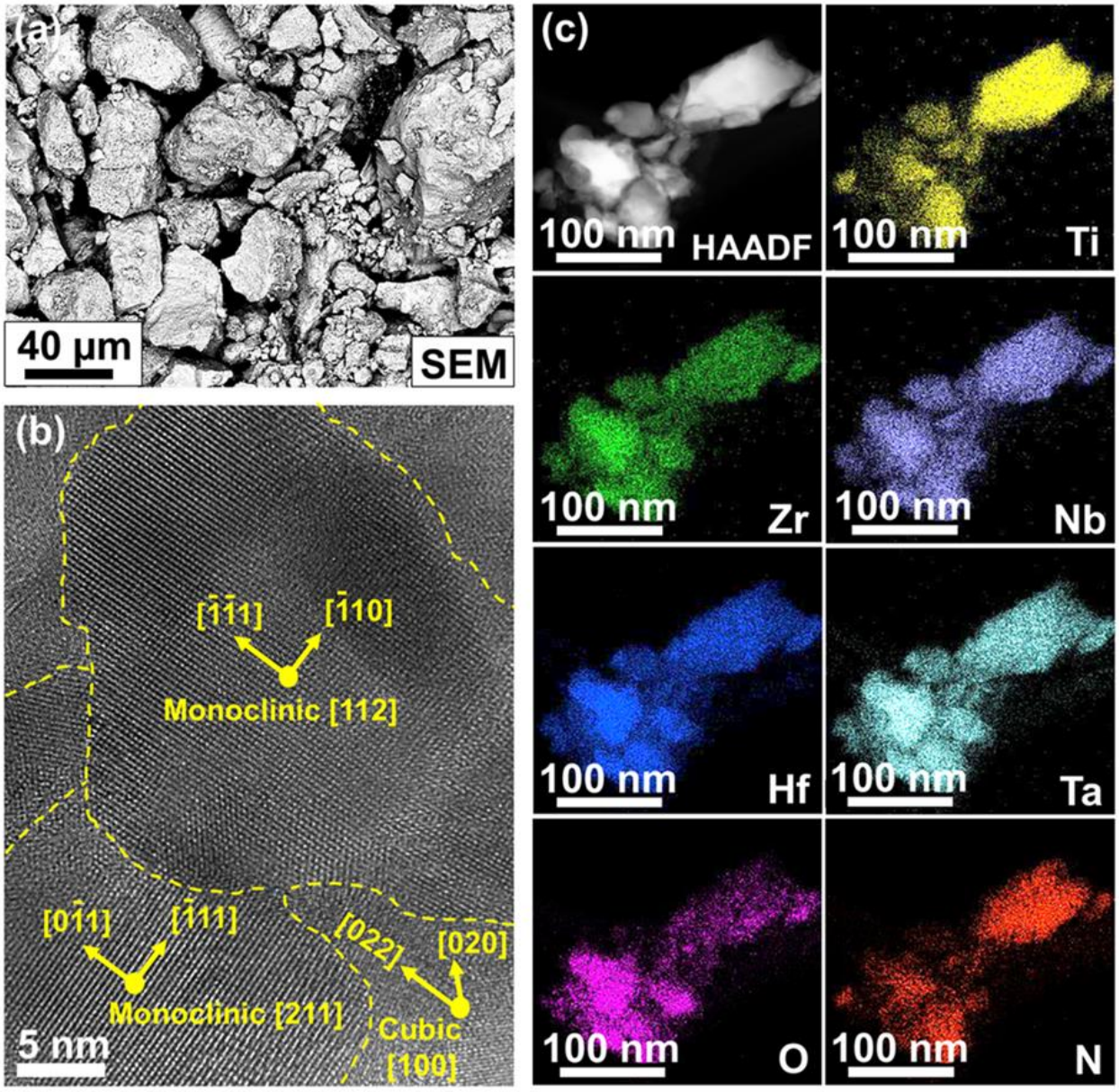


Fig. 5.2. Formation of nanocrystalline monoclinic and cubic phases with uniform elemental distribution in high-entropy oxynitride powder. a) SEM micrograph, b) HR micrograph and c) STEM-HAADF micrograph and relevant EDS mappings for high-entropy oxynitride.

Fig. 5.3a shows the light absorbance of the HEON in comparison with the relevant HEO as well as the P25 $TiO_2$ photocatalyst. The HEON exhibits significant light absorbance compared with the HEO and P25 $TiO_2$. According to the Kubelka-Munk calculation, the bandgap for the HEON is 1.6 eV which is extremely narrower compared with the bandgap of the HEO (3.0 eV) and P25 (3.1 eV) [27]. Fig. 5.3b shows the electronic band structure of the three mentioned materials including the appearance of three samples. A color change from white and orange for P25 $TiO_2$ and the HEO occurs to dark brown for the HEON, confirming the high light absorbance of the HEON in good agreement with the UV-vis absorbance data [35]. The electronic band structures were determined by considering the bandgaps calculated using the Kubelka-Munk theory, the top of the valence band was measured by XPS spectroscopy, and the bottom of the conduction band was calculated by subtracting the bandgap from the top of the conduction band. The bandgap for the P25 $TiO_2$, the HEO and the HEON are 3.0, 3.0 and 1.6 eV, respectively; the values for the top of the valence band are 2.2, 1.8 and 1.3 eV vs. NHE for P25 $TiO_2$, the HEO and the HEON, respectively; and the values for the bottom of the conduction band are -0.8, -1.2 and -0.3 eV vs. NHE for P25 $TiO_2$, the HEO and the HEON, respectively. As shown in Fig. 5.3b, the band structure of the HEON indicates its low bandgap with appropriate positions of the valence band top and the conduction band bottom for various $CO_2$ conversion reactions [36]. The low bandgap of this HEON can lead to easy separation of electrons and holes during photocatalysis.

Fig. 5.3c shows the photoluminescence spectra of the three materials to examine the electron-hole recombination. P25 $TiO_2$ and the HEO have almost the same photoluminescence intensity while the HEON shows the lowest photoluminescence. The absence of an intensive photoluminescence peak for the HEON confirms the significant suppression of electron-hole recombination which is a principal requirement for the enhancement of photocatalytic reactions [37,38]. These results show that the main problem of metal oxynitrides in terms of high electron-hole recombination [7,9] can be solved by the strategy used in this study through the concept of high-entropy ceramics.

Fig. 5.3d shows the photocurrent measurement for the three samples. Due to the different particle sizes of these three samples and their dissimilarities in making binding to the FTO glass, their current density cannot be compared quantitatively; however, the shape of their photocurrent curves can clarify their different behaviors. For P25 $TiO_2$ there is a spike peak at the beginning of irradiation, but the current density decreases rapidly to a steady state, suggesting that electron-hole

separation is followed by fast recombination. For the HEO the photocurrent curve under irradiation is almost a straight horizontal line which shows a better electron-hole separation of the HEO compared to P25 $TiO_2$. For the HEON, the current density increases by irradiation and reaches a steady state, suggesting that the ratio of electron-hole recombination to separation is the lowest for the HEON. After stopping the irradiation, the HEON still shows some reduced photocurrent due to the remained excited charge carriers, while P25 $TiO_2$ exhibits almost no photocurrent under the dark condition. The successful photocurrent generation on this HEON with an appropriate ratio of electron-hole separation to recombination suggests the potential of this material to act as a catalyst for $CO_2$ photoreduction [27,35].

Fig. 5.4a compares the CO production rate of the HEON with the relevant HEO and P25 $TiO_2$ benchmark photocatalyst. Photoreduction of $CO_2$ to CO on the HEON is considerably better than the HEO and P25. The CO production rate for the HEON reaches 14.3 $\mu molh^{-1}g^{-1}$ after 1 h; and then decreases to a constant level after 3 h. The deviations in the reaction rate in the first two hours should be due to the time needed to reach an equilibrium condition in the measurement system. The average CO production rate for this HEON is 11.6 ± 1.5 $\mu molh\text{-}^{1}g^{-1}$ after 5 h, while the HEO and P25 have lower photocatalytic CO production rates of 4.6 ± 0.3 $\mu molh^{-1}g^{-1}$. Fig. 5.4b shows the photocatalytic activity of the HEON for $H_2$ production and compares it with the HEO and P25 $TiO_2$. This figure indicates that the efficiency of the HEON is much better than the HEO and P25 for photocatalytic $H_2$ production. The average $H_2$ production rate for the HEON is 5.1 ± 0.5 $\mu molh^{-1}g^{-1}$, while the rate for the HEO and P25 $TiO_2$ is 1.3 ± 0.1 and 1.5 ± 0.1 $\mu molh^{-1}g^{-1}$, respectively. To confirm the high activity and stability of this HEON for $CO_2$ photoreduction, a long-term photocatalytic experiment for 20 h was conducted on the sample after storage in air for 7 months. As shown with dashed-line curves in Fig. 5.4a and 5.4b, the material still shows high activity with a constant CO and $H_2$ production rate, although the reaction rates are slightly lower than in the first experiment.

Here, three issues regarding the photocatalytic tests should be mentioned. First, no CO was detected in three blank tests: (i) with catalyst addition and $CO_2$ injection under dark conditions, (ii) without catalyst addition under light irradiation and $CO_2$ injection, and (iii) with catalyst addition under light irradiation and argon injection. Second, despite the high light absorbance of HEON in the visible light and near-infrared region, the material did not show any photocatalytic activity in these regions within the detection limits of gas chromatographs. Third, despite the

higher feasibility of $CH_4$ production compared to CO generation in terms of thermodynamics, no $CH_4$ was detected for these materials which can be explained by the kinetics of reactions. Due to the requirement of $CH_4$ production to more electrons and protons, its production is not kinetically more feasible than CO production [39,40]. On the other hand, once CO is produced, it does not tend to be adsorbed on active sites and thus the reaction terminates with the CO production [41].

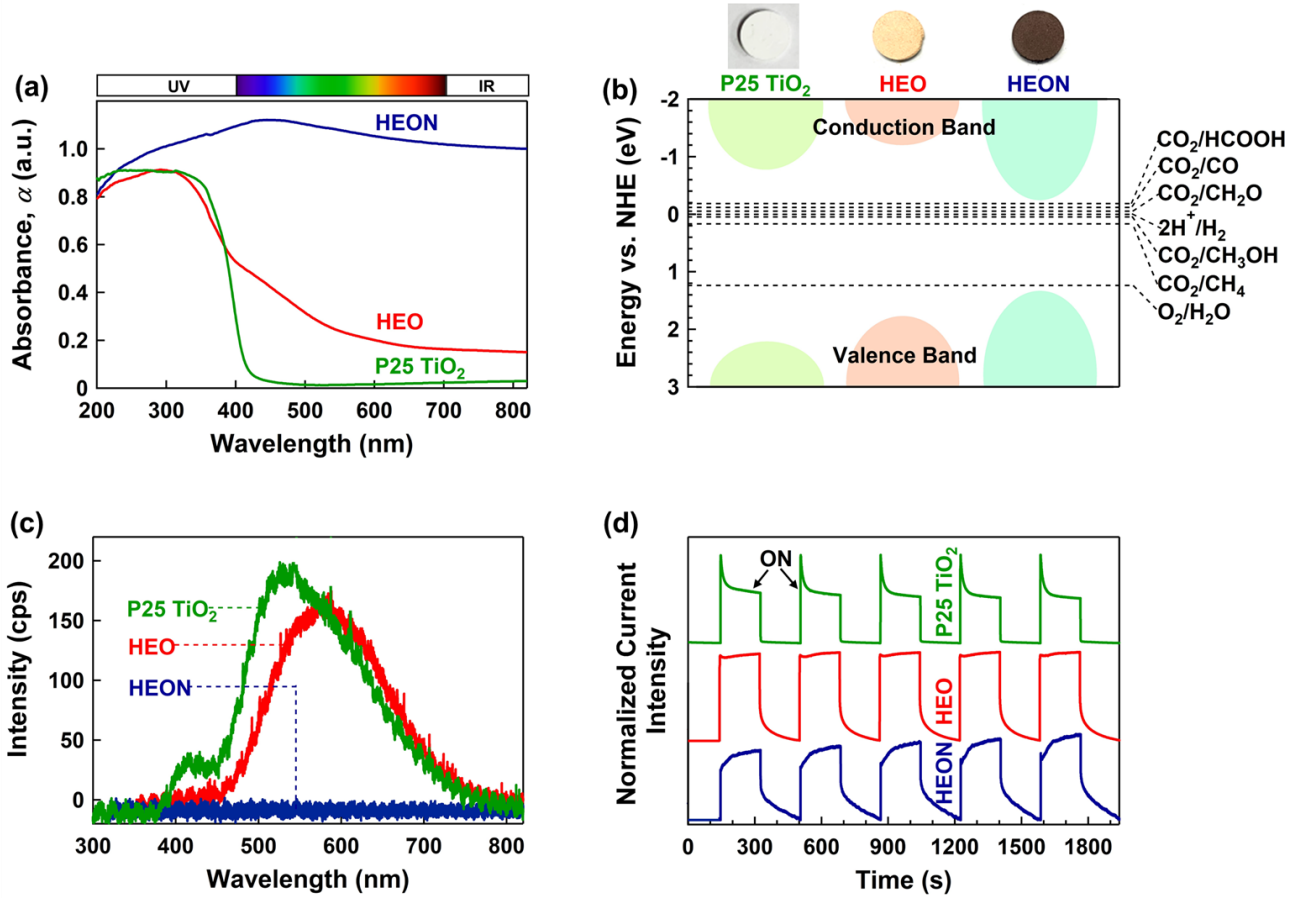


Fig. 5.3. High light absorbance, appropriate electronic band structure and low electron-hole recombination in high-entropy oxynitride. a) UV-vis spectra, b) electronic band structures including chemical potential for $CO_2$ conversion reactions and sample color, c) steady-state photoluminescence spectra and d) photocurrent generation of high-entropy oxynitride (HEON) in comparison with corresponding high-entropy oxide (HEO) and P25 $TiO_2$.

Fig. 5.4c illustrates the XRD profiles of HEON before and after photocatalysis. The profiles indicate that the crystal structures do not change after photoreduction, suggesting that the

HEON remains stable after photocatalytic $CO_2$ conversion. The high stability of $TiZrHfNbTaO_6N_3$ is partly because of the entropy-stabilization concept which leads to low Gibbs free energy in the presence of a large number of elements [13,14]. This high stability is an important issue that has led to the utilization of high-entropy ceramics for various applications with superior performance [10-30].

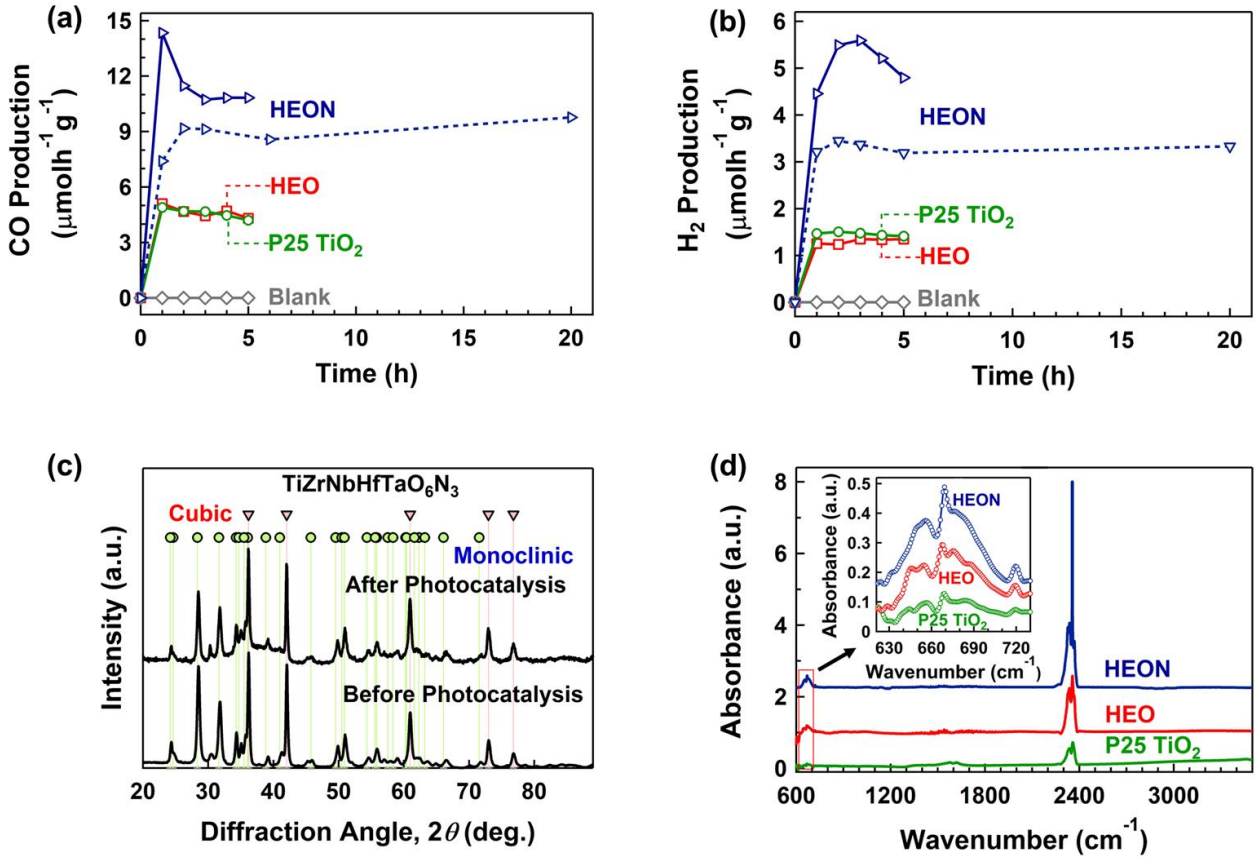


Fig. 5.4. High efficiency of high-entropy oxynitride for photocatalytic CO and hydrogen production. Rate of (a) $CO_2$ to CO photoreduction and (b) hydrogen generation versus UV irradiation time for high-entropy oxynitride (HEON) compared to corresponding high-entropy oxide (HEO) and P25 $TiO_2$. (c) XRD profiles before and after photocatalysis for high-entropy oxynitride. (d) DRIFT spectra of three samples.

Fig. 5.4d shows the DRIFT spectra for the three samples to investigate the adsorbance mode of $CO_2$ on the surface of each photocatalyst. There is a peak at 665 $cm^{-1}$ which corresponds to $CO_3^{2-}$ [423] and another one at 2340-2360 $cm^{-1}$ which is relevant to $CO_2$ gas in the beamline of

spectrometer or to physically adsorbed $CO_2$ on photocatalysts [43]. The intensity of both peaks is the maximum for the HEON, but it is hard to discuss about physically adsorbed $CO_2$ using the peak at 2340-2360 $cm^{-1}$ due to the possible differences in the $CO_2$ gas concentration in the beamline. The peak at 665 $cm^{-1}$ for P25 $TiO_2$ is so weak, but its intensity is the highest for the HEON, suggesting $CO_2$ can bond to the surface as carbonate. Since $CO_2$ is a Lewis acid, the basic active sites have a significant role in the adsorption and activation of this molecule [44]. P25 $TiO_2$ is considered a weak acid and chemisorption of $CO_2$ in the form of carbonate is weak on the surface of this material. The high intensity of carbonate peak on the HEON suggests that the concentration of basic active sites is higher in this material. These DRIFT experiments indicate the higher capability of the HEON for physisorption and chemisorption of $CO_2$ compared to the HEO and P25 $TiO_2$.

### 5.4. Discussion

Three points need to be discussed in detail here: (i) the mechanism of photocatalytic CO production, (ii) the reasons for the high activity of the HEON, and (iii) the comparison of the activity of current HEON with other photocatalysts reported so far in the literature.

Regarding the first issue, it should be noted that the first step in photocatalytic $CO_2$ reduction process is the formation of $CO_2^{\bullet-}$ intermediate which is produced by sharing the electrons between $CO_2$ and photocatalyst surface [45]. Chemisorption of $CO_2$ molecules on photocatalyst surface to produce $CO_2^{\bullet-}$occurs in three modes. (1) Nucleophilic bonding between oxygen atoms and catalyst surface (oxygen coordination), (2) electrophilic bonding between carbon atoms and catalyst surface (carbon coordination) and (3) mixed coordination between both oxygen and carbon atoms in $CO_2$ molecules with catalyst surface [45]. The chemistry of photocatalyst influences the bonding of $CO_2^{\bullet-}$ with catalyst surface and determine the reaction pathway [45]. If a photocatalyst contains Sn, Pb, Hg, In, and Cd metals, then it has a tendency to oxygen coordination to produce $^{\bullet}OCHO$ as an intermediate and formic acid (HCOOH) as the final product. Photocatalysts containing noble and transition metals have a tendency to carbon coordination which leads to producing $^{\bullet}CO$ and $^{\bullet}OCHO$ as intermediates. Since the bonding between $^{\bullet}CO$ and catalyst surface is weak, CO is usually the main product in this coordination. If a photocatalyst consists of Cu atoms, then $^{\bullet}CO$ and $^{\bullet}OCHO$ are produced as intermediates, but because of the strong bonding between $^{\bullet}CO$ and Cu, other hydrocarbons such as methane ($CH_4$) and ethanol

($C_2H_5OH$) are usually formed as final products [45]. In this study, since the HEON, the HEO and P25 $TiO_2$ consist of transition metals, the carbon coordination pathway occurs for these photocatalysts which leads to CO production. This pathway has the following reactions [45].

$$CO_2 + e^- \rightarrow CO_2^{\bullet -} \quad (5.1)$$

$$CO_2^{\bullet -} + 2e^- + 2H^+ \rightarrow CO + H_2O \quad (5.2)$$

Regarding the second issue, it should be considered that combining the concepts of metal oxynitrides and high-entropy ceramics was the spark starter of this study. Metal oxynitrides have been introduced as promising low-bandgap photocatalysts particularly for water splitting [5], while their application for $CO_2$ conversion is still in the initial steps [6-8]. The reason for the low bandgap of oxynitrides compared to oxide photocatalysts is that the valence band top of these materials is generated using hybridized 2p oxygen and nitrogen orbitals, but it is generated using only 2p oxygen orbitals in oxides. Since the energy level for nitrogen 2p orbitals is higher than oxygen 2p orbitals, the bandgap of oxynitrides is smaller than oxides [5]. However, these metal oxynitrides suffer from significant recombination of charge carriers and modest stability [6,9].

High-entropy ceramics are promising new materials with interesting properties because of the presence of multiple elements which leads to superior stability, large lattice defects/strain and heterogenous valence electron distribution [13,14]. The presence of various elements in the lattice of high-entropy ceramics leads not only to high configurational entropy and resultant high chemical stability for catalysis but also to lattice distortion and formation of inherent point defects such as vacancies which can act as active sites for catalysis [46]. Although future theoretical studies are required to determine the active sites in high-entropy photocatalysts, it was shown in conventional photocatalysts that vacancies on the surface adsorb $CO_2$ and activate it by decreasing the bonding energy between carbon and oxygen [41,45]. These vacancies trap electrons and act as active sites and lead to the improved photocatalytic activity for $CO_2$ reduction, but their fraction should be optimized to achieve the highest activity and best reaction selectivity [47,48].

The combination of the two concepts of oxynitrides and high-entropy ceramics led to the introduction of $TiZrNbHfTaO_6N_3$ as a highly stable and low-bandgap photocatalyst for $CO_2$ conversion with much better photocatalytic performance compared with P25 $TiO_2$. Such a high activity is particularly interesting because the surface area of the HEON is much smaller than P25

$TiO_2$: 2.3 $m^2g^{-1}$ for the HEON and 38.7 $m^2g^{-1}$ for P25 $TiO_2$ measured by the Brunauer-Emmett-Teller (BET) technique in the nitrogen atmosphere. The high activity of the HEON for $CO_2$ photoreduction can be attributed to high light absorbance (i.e., easy electron-hole separation), appropriate band positions compared to chemical potentials for reactions, and low electron-hole recombination, and high surface $CO_2$ adsorption [34,37]. The presence of interphase boundaries in this HEON can also partly contribute to the easy separation of charge carriers and improvement of photocatalytic activity [34].

Regarding the third issue, although the comparison between the current HEON and P25 $TiO_2$ using similar experimental procedures confirms the high photocatalytic activity of the HEON, it is worth comparing the activity of this HEON with the given data in the literature. Photocatalysis in various studies is performed in different conditions in terms of photoreactor type, temperature, catalyst concentration, $CO_2$ flow rate, type of light source and concentration of reactants, and thus, a comparison between different studies should be evaluated with care. The CO production rate per catalyst mass and catalyst surface area are given in Table 5.1 in comparison with reported photocatalysts in the literature [48-79]. Since photocatalysis occurs on the surface, normalizing the CO production rate per surface area should be more reasonable for comparison purposes. According to Table 5.1, the rate of CO production in the literature fluctuates in the 0.00095-1.33 $\mu molh^{-1}m^{-1}$ range, while the CO generation rate of 4.66 ± 0.3 $\mu molh^{-1}m^{-1}$ on the HEON is higher than all these reported data. Moreover, the HEON shows much better activity per both surface area and mass unit compared to other oxynitrides reported in the literature. Although these findings introduce HEON as the most effective photocatalyst for $CO_2$ photoreduction, future studies should focus on decreasing the particle size of these materials to increase their specific surface area.

Table 5.1. Photocatalytic $CO_2$ to CO conversion rate on high-entropy oxynitride compared to reported photocatalysts. For some catalysts which surface area was not reported in literature, CO production rate in $\mu molh^{-1}m^{-1}$ was not given.

| Photocatalyst | Catalyst Concentration | Light Source | CO Production Rate ($\mu molh^{-1}g^{-1}$) | CO Production Rate ($\mu molh^{-1}m^{-1}$) | Ref. |
|---|---|---|---|---|---|
| $TiO_2$ / Carbon Nitride Nanosheet | 25 mg (Gas System) | 150 W Xenon | 2.04 | ---- | [49] |
| $TiO_2$ / Graphitic Carbon | 100 mg (Gas System) | 300 W Xenon | 10.16 | 0.04 | [50] |
| $TiO_2$ Nanosheets Exposed {001} Facet | 1 $gL^{-1}$ (Liquid system) | Two 18 W Low-Pressure Mercury | 0.12 | 0.00095 | [51] |
| $TiO_2$ / CoOx Hydrogenated | 50 mg (Gas System) | 150 W UV | 1.24 | 0.0045 | [52] |
| $TiO_2$ 3D Ordered Microporous / Pd | 100 mg (gas system) | 300 W Xenon | 3.9 | 0.066 | [53] |
| $Pt^{2+}$–$Pt^0$ / $TiO_2$ | 100 mg (Gas System) | 300 W Xenon | ~12.14 | 0.7 | [54] |

| | | | | | |
|---|---|---|---|---|---|
| Anatase $TiO_2$ Hierarchical Microspheres | 200 mg (Gas System) | 40 W Mercury UV | 18.5 | 0.37 | [55] |
| $TiO_2$ and Zn(II) Porphyrin Mixed Phases | 60 mg (Gas System) | 300 W Xenon | 8 | 0.062 | [56] |
| Anatase $TiO_2$ Hollow Sphere | 100 mg (Gas System) | 40 W Mercury UV | 14 | 0.16 | [57] |
| Anatase $TiO_2$ Nanofibers | 50 $gL^{-1}$ (Liquid System) | 500 W Mercury Flash | 40 | ----- | [58] |
| $C_3N_4$ by Thermal Condensation | 100 mg (Gas System) | 350 W Mercury | 4.83 | ------ | [59] |
| $Cd_{1-x}Zn_xS$ | 45 mg (Gas System) | UV-LED irradiation | 2.9 | 0.015 | [60] |
| BiOI | 150 mg (Gas System) | 300 W High-Pressure xenon | 4.1 | 0.03 | [61] |
| $xCu_2O$ / $Zn_{2-2x}Cr$ | 4 $gL^{-1}$ (Liquid System) | 200 W Mercury-Xenon | 2.5 | 0.018 | [62] |
| $CeO_{2-x}$ | 50 mg (Gas System) | 300 W Xenon | 1.65 | 0.08 | [63] |
| $Cu_2O$ / $RuO_x$ | 500 mg (Gas System) | 150 W Xenon | 0.88 | --- | [64] |
| $Bi_2Sn_2O_7$ | 0.4 $gL^{-1}$ (Liquid System) | 300 W xenon | 14.88 | 0.24 | [65] |
| Ag / Bi / $BiVO_4$ | 10 mg (Gas System) | 300W Xenon Illuminator | 5.19 | 0.42 | [66] |
| g-$C_3N_4$ / BiOCl | 20 mg (Gas System) | 300 W High-Pressure Xenon | 4.73 | --- | [67] |
| Fe / g-$C_3N_4$ | 1 $gL^{-1}$ (Liquid System) | 300 W Xenon | ~22.5 | 0.06 | [68] |
| $Bi_2MoO_6$ | 0.7 $gL^{-1}$ (Liquid System) | 300 W Xenon | 41.5 | 1.26 | [69] |
| $Bi_{24}O_{31}C_{l10}$ | 50 mg (Gas System) | 300 W High-Pressure Xenon | 0.9 | --- | [70] |
| g-$C_3N_4$ / Zinc Carbodiimide / Zeolitic Imidazolate Framework | 100 mg (Gas System) | 300 W Xenon | ~0.45 | 0.014 | [71] |
| $BiVO_4$ / C / $Cu_2O$ | --- | 300 W Xenon | 3.01 | ---- | [72] |
| g-$C_3N_4$ / α-$Fe_2O_3$ | 200 mg (Gas System) | 300 W Xenon | 5.7 | ----- | [73] |
| Bicrystalline Anatase/Brookite $TiO_2$ Microspheres | 30 mg (Gas System) | 150 W Solar Simulator | 145 | 0.95 | [74] |
| 10 wt % In-Doped Anatase $TiO_2$ | 250 mg (Gas System) | 500 W Mercury Flash | 81 | 1.33 | [75] |
| 10 wt % Montmorillonite-Loaded $TiO_2$ | 50 mg (Gas System) | 500 W Mercury | 103 | 1.25 | [76] |
| $Bi_4O_5Br_2$ | 20 mg (Gas System) | 300 W High-Pressure Xenon | 63.13 | 0.58 | [77] |
| ZnGaON | --- | 1600 W Xenon | 1.05 | --- | [78] |
| $WO_3$ / $LaTiO_2N$ | 10 mg (Gas System) | 300 W Xenon | 2.21 | 0.4 | [79] |
| α-$Fe_2O_3$ / $LaTiO_2N$ | 20 mg (Gas System) | 300 W Xenon | 9.7 | 0.65 | [6] |
| RuRu / Ag / TaON | 1 $gL^{-1}$ (Liquid System) | High-Pressure Mercury | 5 | ---- | [7] |
| RuRu / TaON | 1 $gL^{-1}$ (Liquid system) | High-Pressure Mercury | 3.33 | ---- | [7] |
| Ag / TaON / RuBLRu′ | 2 $gL^{-1}$ (Liquid System) | 500 W High-Pressure Mercury | 0.056 | ---- | [8] |
| $TiZrHfNbTaO_6N_3$ | 0.2 $gL^{-1}$ (Liquid System) | 400 W High-Pressure Mercury | 10.7 ± 1.8 | 4.7 ± 0.3 | This study |

## 5.4. Conclusion

This chapter introduced a high-entropy oxynitride with low bandgap, low electron-hole recombination, high $CO_2$ adsorbance and high chemical stability for photocatalytic $CO_2$ conversion. The material, which was synthesized using high-pressure torsion and subsequent oxidation and nitriding, had two phases of face-centered cubic and monoclinic with a chemical composition of $TiZrNbHfTaO_6N_3$. The material had better photocatalytic $CO_2$ conversion performance compared with corresponding high-entropy oxide, benchmark photocatalyst P25 $TiO_2$ and all reported photocatalysts in the literature. These findings open a new path to developing highly efficient photocatalysts for $CO_2$ conversion.

## References


[1] S.N. Habisreutinger, L. Schmidt-Mende, J.K. Stolarczyk, Photocatalytic reduction of $CO_2$ on $TiO_2$ and other semiconductors, Angew. Chem. 52 (2013) 7372-7408.

[2] N. Shehzad, M. Tahir, K. Johari, T. Murugesan, M. Hussain, A critical review on $TiO_2$ based photocatalytic $CO_2$ reduction system: strategies to improve efficiency, J. $CO_2$ Util. **26** (2018) 98-122.

[3] H. Liu, H. Song, W. Zhou, X. Meng, J. Ye, A promising application of optical hexagonal TaN in photocatalytic reactions, Angew. Chem. 130 (2018) 17023-17026.

[4] A. Akhundi, A. Habibi-Yangjeh, M. Abitorabi, S.R. Pouran, Review on photocatalytic conversion of carbon dioxide to value-added compounds and renewable fuels by graphitic carbon nitride-based photocatalysts, Catal. Rev. Sci. Eng.61 (2019) 595-628.

[5] T. Takata, C. Pan, K. Domen, Recent progress in oxynitride photocatalysts for visible-light-driven water splitting, Sci. Technol. Adv. Mater. 16 (2015) 033506.

[6] J. Song, Y. Lu, Y. Lin, Q. Liu, X. Wang, W. Su, A direct Z-scheme α-$Fe_2O_3$/$LaTiO_2N$ visible-light photocatalyst for enhanced $CO_2$ reduction activity, Appl. Catal. B 292 (2021) 120185.

[7] A. Nakada, T. Nakashima, K.Sekizawa, K. Maeda, O. Ishitani, Visible-light-driven $CO_2$ reduction on a hybrid photocatalyst consisting of a Ru(II) binuclear complex and a Ag-loaded TaON in aqueous solutions, Chem. Sci. 7 (2016) 4364-4371.

[8] K. Sekizawa, K. Maeda, K. Domen, K. Koike, O. Ishitani, Artificial Z-Scheme constructed with a supramolecular metal complex and semiconductor for the photocatalytic reduction of $CO_2$, J. Am. Chem. Soc. 135 (2013) 4596-4599.

[9] L. Pei, Y. Yuan, W. Bai, T. Li, H. Zhu, Z. Ma, J. Zhong, S. Yan, Z. Zou, In situ-grown island-shaped hollow graphene on TaON with spatially separated active sites achieving enhanced visible-light $CO_2$ reduction, ACS Catal. 10 (2020) 15083-15091.

[10] D.D. Le, S.K. Hong, T.S. Ngo, J. Le, Y.C. Park, S.I. Hong, Y.S. Na, Microstructural investigation of CoCrFeMnNi high entropy alloy oxynitride films prepared by sputtering using an air gas, Met. Mater. Int. 24 (2018) 1285-1292.

[11] P. Edalati, X.F. Shen, M. Watanabe, T. Ishihara, M. Arita, M. Fuji, K. Edalati, High-entropy oxynitride as low-bandgap and stable photocatalyst for hydrogen production, J. Mater. Chem. A 9 (2021) 15076-15086.

[12] K. Edalati, Z. Horita, A review on high-pressure torsion (HPT) from 1935 to 1988, J. Mater. Sci. Eng. A 652 (2016) 325-352.

[13] S. Akrami, P. Edalati, M. Fuji, K. Edalati, High-entropy ceramics: review of principles, production and applications, Mater. Sci. Eng. R: Rep. 146 (2021) 100644.

[14] C. Oses, C. Toher, S. Curtarolo, High-entropy ceramics, Nat. Rev. Mater. 5 (2020) 295-309.

[15] S.H. Albedwawi, A. AlJaberi, G.N. Haidemenopoulos, K. Polychronopoulou, High entropy oxides-exploring a paradigm of promising catalysts: a review, Mater. Des. 202 (2021) 109534.

[16] D. Wang, Z. Liu, S. Du, Y. Zhang, H. Li, Z. Xiao, W. Chen, R. Chen, Y. Wang, Y. Zou, Low-temperature synthesis of small-sized high-entropy oxides for water oxidation, J. Mater. Chem. A 7 (2019) 24211-24216.

[17] Z. Ding, J. Bian, S. Shuang, X. Liu, Y. Hu, C. Sun, Y. Yang, High entropy intermetallic–oxide core–shell nanostructure as superb oxygen evolution reaction catalyst, Adv. Sustain. Syst. 4 (2020) 1900105.

[18] G. Fang, J. Gao, J. Lv, H. Jia, H. Li, W. Liu, G. Xie, Z. Chen, Y. Huang, Q. Yuan, X. Liu, X. Lin, S. Sun, H.J. Qiu, Multi-component nanoporous alloy/(oxy)hydroxide for bifunctional oxygen electrocatalysis and rechargeable Zn-air batteries, Appl. Catal. B 268 (2020) 118431.

[19] F. Okejiri, Z. Zhang, J. Liu, M. Liu, S. Yang, S. Dai, Room-temperature synthesis of high-entropy perovskite oxide nanoparticle catalysts through ultrasonication-based method, ChemSusChem 13 (2020) 111-115.

[20] H. Xu, Z. Zhang, J. Liu, C.L. Do-Thanh, H. Chen, S. Xu, Q. Lin, Y. Jiao, J. Wang, Y. Wang, Y. Chen, S. Dai, Entropy-stabilized single-atom Pd catalysts via high-entropy fluorite oxide supports, Nat. Commun. 11 (2020) 3908.

[21] H. Chen, K. Jie, C.J. Jafta, Z. Yang, S. Yao, M. Liu, Z. Zhang, J. Liu, M. Chi, J. Fu, S. Dai, An ultrastable heterostructured oxide catalyst based on high-entropy materials: a new strategy toward catalyst stabilization via synergistic interfacial interaction, Appl. Catal. B 276 (2020) 119155.

[22] Y. Zheng, Y. Yi, M. Fan, H. Liu, X. Li, R. Zhang, M. Li, Z.A. Qiao, A High-entropy metal oxide as chemical anchor of polysulfide for lithium-sulfur batteries, Energy Storage Mater. 23 (2019) 678-683.

[23] H. Chen, W. Lin, Z. Zhang, K. Jie, D.R. Mullins, X. Sang, S.Z. Yang, C.J. Jafta, C.A. Bridges, X. Hu, Mechanochemical synthesis of high entropy oxide materials under ambient conditions: dispersion of catalysts via entropy maximization, ACS Mater. Lett. 1 (2019) 83-88.

[24] M.S. Lal, R. Sundara, High entropy oxides - a cost-effective catalyst for the growth of high yield carbon nanotubes and their energy applications, ACS Appl. Mater. Interfaces 11 (2019) 30846-30857.

[25] Y. Shu, J. Bao, S. Yang, X. Duan, P. Zhang, Entropy-stabilized metal-$CeO_x$ solid solutions for catalytic combustion of volatile organic compounds, AIChE J. 67 (2021) e17046.

[26] P. Edalati, Q. Wang, H. Razavi-Khosroshahi, M. Fuji, T. Ishihara, K. Edalati, Photocatalytic hydrogen evolution on a high-entropy oxide, J. Mater. Chem. A 8 (2020) 3814-3821.

[27] S. Akrami, Y. Murakami, M. Watanabe, T. Ishihara, M. Arita, M. Fuji, K. Edalati, Defective high-entropy oxide photocatalyst with high activity for $CO_2$ conversion, Appl. Catal. B 303 (2022) 120896.

[28] O.F. Dippo, N. Mesgarzadeh, T.J. Harrington, G.D. Schrader, K.S. Vecchio, Bulk high-entropy nitrides and carbonitrides, Sci. Rep. 10 (2020) 21288.

[29] T. Jin, X. Sang, R.R. Unocic, R.T. Kinch, X. Liu, J. Hu, H. Liu, S. Dai, Mechanochemical-assisted synthesis of high-entropy metal nitride via a soft urea strategy, Adv. Mater. 30 (2018) 1707512.

[30] C.Y. He, X.L. Qiu, D.M. Yu, S.S. Zhao, H.X. Guo, G. Liu, X.H. Gao, Greatly enhanced solar absorption via high entropy ceramic AlCrTaTiZrN based solar selective absorber coatings, J. Materiomics 7 (2021) 460-469.

[31] K. Edalati, A. Bachmaier, V.A. Beloshenko, Y. Beygelzimer, V.D. Blank, W.J. Botta, K. Bryła, J. Čížek, S. Divinski, N.A. Enikeev, Y. Estrin, G. Faraji, R.B. Figueiredo, M. Fuji, T. Furuta, T. Grosdidier, J. Gubicza, A. Hohenwarter, Z. Horita, J. Huot, Y. Ikoma, M. Janeček, M. Kawasaki, P. Krăl, S. Kuramoto, T.G. Langdon, D.R. Leiva, V.I. Levitas, A. Mazilkin, M. Mito, H. Miyamoto, T. Nishizaki, R. Pippan, V.V. Popov, E.N. Popova, G. Purcek, O. Renk, Á. Révész, X. Sauvage, V. Sklenicka, W. Skrotzki, B.B. Straumal, S. Suwas, L.S.

Toth, N. Tsuji, R.Z. Valiev, G. Wilde, M.J. Zehetbauer, X. Zhu, Nanomaterials by severe plastic deformation: review of historical developments and recent advances, Mater. Res. Lett. 10 (2022) 163-256.

[32] J. Low, J. Yu, M. Jaroniec, S. Wageh, A.A. Al-Ghamdi, Heterojunction photocatalysts, Adv. Mater. 29 (2017) 1601694.

[33] Y. Wang, H. Huang, Z. Zhang, C. Wang, Y. Yang, Q. Li, D. Xu, Lead-free perovskite $Cs_2AgBiBr_6$@g-$C_3N_4$ Z-scheme system for improving $CH_4$ production in photocatalytic $CO_2$ reduction, Appl. Catal. B 282 (2021) 119570.

[34] K. Li, B. Peng, T. Peng, Recent advances in heterogeneous photocatalytic $CO_2$ conversion to solar fuels, ACS Catal. 6 (2016) 7485-7527.

[35] S. Akrami, M. Watanabe, T.H. Ling, T. Ishihara, M. Arita, M. Fuji, K. Edalati, High pressure $TiO_2$-II polymorph as an active photocatalyst for $CO_2$ to CO conversion, Appl. Catal. B 298 (2021) 120566.

[36] X. Li, J. Yu, M. Jaroniec, Hierarchical photocatalysts, Chem. Soc. Rev. 45 (2016) 2603-2636.

[37] J. Ran, M. Jaroniec, S.Z. Qiao, Cocatalysts in semiconductor-based photocatalytic $CO_2$ reduction: achievements, challenges, and opportunities, Adv. Mater. 30 (2018) 1704649.

[38] W. Tu, Y. Zhou, Z. Zou, Photocatalytic conversion of $CO_2$ into renewable hydrocarbon fuels: state-of-the-art accomplishment, challenges, and prospects, Adv. Mater. 26 (2014) 4607-4626.

[39] L.Y. Lin, S. Kavadiya, X. He, W.N. Wang, B.B. Karakocak, Y.C. Lin, M.Y. Berezin, P. Biswas, Engineering stable Pt nanoparticles and oxygen vacancies on defective $TiO_2$ via introducing strong electronic metal-support interaction for efficient $CO_2$ photoreduction, Chem. Eng. J. 389 (2020) 123450.

[40] L. Liu, H. Zhao, J. Andino, Y. Li, Photocatalytic $CO_2$ Reduction with $H_2O$ on $TiO_2$ Nanocrystals: Comparison of Anatase, Rutile, and Brookite Polymorphs and Exploration of Surface Chemistry, ACS Catal. 2 (2012) 1817–1828.

[41] K. Wang, J. Lu, Y. Lu, C.H. Lau, Y. Zheng, X. Fan, Unravelling the C-C coupling in $CO_2$ photocatalytic reduction with $H_2O$ on Au/$TiO_{2-x}$: combination of plasmonic excitation and oxygen vacancy, Appl. Catal. B 292 (2021) 120147.

[42] A.A. Davydov, Infrared Spectroscopy of Adsorbed Species on the Surface of Transition Metal Oxides, Wiley and Sons, Chichester, UK, 1990.

[43] Y. Pan, P. Kuai, Y. Liu, Q. Geb, C. Liu, Promotion effects of $Ga_2O_3$ on $CO_2$ adsorption and conversion over a $SiO_2$-supported Ni catalyst, Energy Environ. Sci. 3 (2010) 1322-1325.

[44] M.A.A. Aziz, A.A. Jalil, S. Wongsakulphasatch, D.V.N. Vo, Understanding the role of surface basic sites of catalysts in $CO_2$ activation in dry reforming of methane: a short review, Catal. Sci. Technol. 10 (2020) 35-45.

[45] H. Lu, J. Tournet, K. Dastafkan, Y. Liu, Y.H. Ng, S.K Karuturi, C. Zhao, Z. Yin, Noble-metal-free multicomponent nanointegration for sustainable energy conversion, Chem. Rev. 121 (2021) 10271-10366.

[46] Y. Sun, S. Dai1, High-entropy materials f or catalysis: A new frontier, Sci. Adv. 7 (2021) 20.

[47] Z. Miao, G. Wang, X. Zhang, X. Dong, Oxygen vacancies modified $TiO_2/Ti_3C_2$ derived from MXenes for enhanced photocatalytic degradation of organic pollutants: the crucial role of oxygen vacancy to schottky junction, Appl. Surf. Sci. 528 (2020) 146929.

[48] S. Akrami, Y. Murakami, M. Watanabe, T. Ishihara, M. Arita, Q. Guo, M. Fuji, K. Edalati, Enhanced $CO_2$ conversion on highly-strained and oxygen-deficient $BiVO_4$ photocatalyst, Chem. Eng. J. 442 (2022) 136209.

[49] A. Crake, K.C. Christoforidis, R. Godin, B. Moss, A. Kafizas, S. Zafeiratos, J.R. Durrant, C. Petit, Titanium dioxide/carbon nitride nanosheet nanocomposites for gas phase $CO_2$ photoreduction under UV-visible irradiation, Appl. Catal. B 242 (2019) 369-378.

[50] Y. Wang, Y. Chen, Y. Zuo, F. Wang, J. Yao, B. Li, S. Kang, X. Li, L. Cui, Hierarchically mesostructured $TiO_2$/graphitic carbon composite as a new efficient photocatalyst for the reduction of $CO_2$ under simulated solar irradiation, Catal. Sci. Technol. 3 (2013) 3286-3291.

[51] Z. He, L. Wen, D. Wang, Y. Xue, Q. Lu, C. Wu, J. Chen, S. Song, Photocatalytic reduction of $CO_2$ in aqueous solution on surface-fuorinated anatase $TiO_2$ nanosheets with exposed {001} fcets, Energy Fuels 28 (2014) 3982-3993.

[52] Y. Li, C. Wang, M. Song, D. Li, X. Zhang, Y. Liu, $TiO_{2-x}/CoO_x$ Photocatalyst sparkles in photothermocatalytic reduction of $CO_2$ with $H_2O$ steam, Appl. Catal. B 243 (2019) 760-770.

[53] J. Jiao, Y. Wei, Y. Zhao, Z. Zhao, A. Duan, J. Liu, Y. Pang, J. Li, G. Jiang, Y. Wang, AuPd/3DOM-$TiO_2$ catalysts for photocatalytic reduction of $CO_2$: high efficient separation of photogenerated charge carriers, Appl. Catal. B 209 (2017) 228-239.

[54] Z. Xiong, H.B. Wang, N.Y. Xu, H.L. Li, B.Z. Fang, Y.C. Zhao, J.Y. Zhang, C.G. Zheng, Photocatalytic reduction of $CO_2$ on $Pt^{2+}$–$Pt^0/TiO_2$ nanoparticles under UV/Vis light

irradiation: a combination of $Pt^{2+}$ doping and Pt nanoparticles deposition, Int. J. Hydrogen Energy 40 (2015) 10049-10062.

[55] B.Z. Fang, A. Bonakdarpour, K. Reilly, Y.L. Xing, F. Taghipour, D.P. Wilkinson, Large-scale synthesis of $TiO_2$ microspheres with hierarchical nanostructure for highly efficient photodriven reduction of $CO_2$ to $CH_4$, ACS Appl. Mater. Interfaces 6 (2014) 15488-15498.

[56] K. Li, L. Lin, T. Peng, Y. Guo, R. Li, J. Zhang, Asymmetric zinc porphyrin-sensitized nanosized $TiO_2$ for efficient visible-light-driven $CO_2$ photoreduction to $CO/CH_4$, J. Chem. Commun. 51 (2015) 12443-12446.

[57] B.Z. Fang, Y.L. Xing, A. Bonakdarpour, S.C. Zhang, D.P. Wilkinson, Hierarchical CuO-$TiO_2$ hollow microspheres for highly efficient photodriven reduction of $CO_2$ to $CH_4$, ACS sustainable. Chem. Eng. 3 (2015) 2381-2388.

[58] Z.Y. Zhang, Z. Wang, S.W. Cao, C. Xue, Au/Pt nanoparticle-decorated $TiO_2$ nanofibers with plasmon-enhanced photocatalytic activities for solar-to-fuel conversion, J. Phys. Chem. C 117 (2013) 25939-25947.

[59] P. Xia, M. Antonietti, B. Zhu, T. Heil, J. Yu, S. Cao, Designing defective crystalline carbon nitride to enable selective $CO_2$ photoreduction in the gas phase, Adv. Funct. Mater. 29 (2019) 1900093.

[60] E.A. Kozlova, M.N. Lyulyukin, D.V. Markovskaya, D.S. Selishchev, S.V. Cherepanova, D.V. Kozlov, Synthesis of $Cd_{1-x}Zn_xS$ photocatalysts for gas-phase $CO_2$ reduction under visible light, Photochem. Photobiol Sci. 18 (2019) 871-877.

[61] L. Ye, H. Wang, X. Jin, Y. Su, D. Wang, H. Xie, X. Liu, X. Liu, Synthesis of olive- green few-layered BiOI for efficient photoreduction of $CO_2$ into solar fuels under visible/near-infrared light, Sol. Energy Mater. Sol. Cells 144 (2016) 732-739

[62] H. Jiang, K. Katsumata, J. Hong, A. Yamaguchi, K. Nakata, C. Terashima, N. Matsushita, M. Miyauchi, A. Fujishima, Photocatalytic reduction of $CO_2$ on $Cu_2O$-loaded Zn-Cr layered double hydroxides, Appl. Catal. B 224 (2018) 783-790.

[63] T. Ye, W. Huang, L. Zeng, M. Li, J. Shi, $CeO_{2-x}$ platelet from monometallic cerium layered double hydroxides and its photocatalytic reduction of $CO_2$, Appl. Catal. B 210 (2017) 141-148.

[64] E. Pastor, F. Pesci, A. Reynal, A. Handoko, M. Guo, X. An, A. Cowan, D. Klug, J. Durrant, J. Tang, Interfacial charge separation in $Cu_2O/RuO_x$ as a visible light driven $CO_2$ reduction catalyst, Phys. Chem. Chem. Phys. 210 (2017) 141-148.

[65] S. Guo, J. Di, C. Chen, C. Zhu, M. Duan, C. Lian, M. Ji, W. Zhou, M. Xu, P. Song, R. Long, X. Cao, K. Gu, J. Xia, H. Liu, Y. Zhao, L. Song, Y. Xiong, S. Li, Z. Liu, Oxygen vacancy mediated bismuth stannate ultra-small nanoparticle towards photocatalytic $CO_2$-to-CO conversion, Appl. Catal. B 276 (2020) 119156.

[66] Z. Duan, X. Zhao, C. Wei, L. Chen, Ag-Bi/$BiVO_4$ chain-like hollow microstructures with enhanced photocatalytic activity for $CO_2$ conversion, Appl. Catal. A 594 (2020) 117459.

[67] Y. Chen, F. Wang, Y. Cao, F. Zhang, Y. Zou, Z. Huang, L. Ye, Y. Zhou, Interfacial oxygen vacancy engineered two-dimensional g-$C_3N_4$/BiOCl heterostructures with boosted photocatalytic conversion of $CO_2$, ACS Appl. Energy Mater. 3 (2020) 4610-4618.

[68] X.Y. Dao, X.F. Xie, J.H. Guo, X.Y. Zhang, Y.S. Kang, W.Y. Sun, Boosting photocatalytic $CO_2$ reduction efficiency by heterostructues of $NH_2$-MIL-101 (Fe)/g-$C_3N_4$, ACS Appl. Energy Mater. 3 (2020) 3946-3954.

[69] X. Zhang, G. Ren, C. Zhang, R. Li, Q. Zhao, C. Fan, Photocatalytic reduction of $CO_2$ to CO over 3D $Bi_2MoO_6$ microspheres: simple synthesis, high efficiency and selectivity, reaction mechanism, Catal. Lett. 150 (2020) 2510-2516.

[70] X. Jin, C. Lv, X. Zhou, L. Ye, H. Xie, Y. Liu, H. Su, B. Zhang, G. Chen, Oxygen vacancies engineering $Bi_{24}O_{31}Cl_{10}$ photocatalyst for boosted $CO_2$ conversion, ChemSusChem. 12 (2019) 2740-2747.

[71] Y. Xie, Y. Zhuo, S. Liu, Y. Lin, D. Zuo, X. Wu, C. Li, P.K. Wong, Ternary g-$C_3N_4$/ZnNCN@ZIF-8 hybrid photocatalysts with robust interfacial interactions and enhanced $CO_2$ reduction, Solar RRL. 4 (2020) 1900440.

[72] C. Kim, K.M. Cho, A. Al-Saggaf, I. Gereige, H.T. Jung, Z-scheme photocatalytic $CO_2$ conversion on three-dimensional $BiVO_4$/carbon-coated $Cu_2O$ nanowire arrays under visible light, ACS Catal. 8 (2018) 4170-4177.

[73] J. Wang, C. Qin, H. Wang, M. Chu, A. Zada, X. Zhang, J. Li, F. Raziq, Y. Qu, L. Jing, Exceptional photocatalytic activities for $CO_2$ conversion on AlO bridged g-$C_3N_4$/α-$Fe_2O_3$ z-scheme nanocomposites and mechanism insight with isotopes Z, Appl. Catal. B 224 (2018) 459-466.

[74] L.J. Liu, D.T. Pitts, H.L. Zhao, C.Y. Zhao, Y. Li, Silver-incorporated bicrystalline (anatase/brookite) $TiO_2$ microspheres for $CO_2$ photoreduction with water in the presence of methanol, Appl. Catal. A 467 (2013) 474-482.

[75] M. Tahir, N.S. Amin, Indium-doped $TiO_2$ nanoparticles for photocatalytic $CO_2$ reduction with $H_2O$ vapors to $CH_4$, Appl. Catal. B 162 (2015) 98-109.

[76] M. Tahir, N.S. Amin, Photocatalytic reduction of carbon dioxide with water vapors over montmorillonite modified $TiO_2$ nanocompositesm, Appl. Catal. B 142-143 (2013) 512-522.

[77] Y. Bai, P. Yang, L. Wang, B. Yang, H. Xie, Y. Zhou, L. Ye, Ultrathin $Bi_4O_5Br_2$ nanosheets for selective photocatalytic $CO_2$ conversion into CO, Chem. Eng. J. 360 (2019) 473-482.

[78] D. Maiti, A.J. Meier, J. Cairns, S. Ramani, K. Martinet, J.N. Kuhn, V.R. Bhethanabotla, Intrinsically strained noble metal-free oxynitrides for solar photoreduction of $CO_2$, Dalton Trans. 48 (2019) 12738-12748.

[79] N. Lin, Y. Lin, X. Qian, X. Wang, W. Su, Construction of a 2D/2D $WO_3$/$LaTiO_2N$ direct Z-scheme photocatalyst for enhanced $CO_2$ reduction performance under visible light, ACS Sustainable Chem. Eng. 9 (2021) 13686-1

# Chapter 6. Concluding remarks and outlook

Global warming has become a significant concern in recent years which seriously threatens the life of humans and creatures. Conversion of $CO_2$ molecules to other components such as CO is a way to stand this event. In this regard, photocatalytic $CO_2$ conversion, which uses solar irradiation as a clean energy source, has been introduced as a new and promising strategy in recent years. Despite the introduction of various materials, which are modified by various strategies, the efficiency of $CO_2$ photoreduction is still low compared to conventional methods for $CO_2$ conversion, as discussed in chapter 1 of this thesis. The high-pressure torsion (HPT) as a severe plastic deformation (SPD) method has been used in this research work to produce some of the most active photocatalysts for $CO_2$ conversion. The HPT method could increase the $CO_2$ photoreduction efficiency by (i) oxygen vacancy and strain engineering, (ii) stabilization of high-pressure phases, (iii) formation of defective high-entropy oxides, and (iv) synthesis of low-bandgap oxynitrides.

In chapter 2, a photocatalyst with low bandgap, improved band structure and low recombination rate of electrons and holes was produced by simultaneous introduction of oxygen vacancies and lattice strain in $BiVO_4$ via the HPT process. The material showed high photocatalytic activity for $CO_2$ to CO conversion with an activity comparable to P25 $TiO_2$ as a benchmark photocatalyst. This chpter suggests that simultaneous engineering of lattice strain and defects is an effective strategy to produce active photocatalysts for $CO_2$ conversion.

In chapter 3, effect of high pressure $TiO_2$-II phase on photocatalytic $CO_2$ conversion was examined for the first time. The introduction of nanostructured $TiO_2$-II phase and $TiO_2$-II/anatase heterojunctions modified the band structure and enhanced the photocurrent and photocatalytic activity, despite the formation of strain-induced vacancies in the bulk. Thermal annihilation of vacancies in the bulk led to further improvement of photocatalytic $CO_2$ conversion, confirming the significance of the $TiO_2$-II phase for photocatalytic reactions.

In chapter 4, a high-entropy oxide with a general composition of $TiZrNbHfTaO_{11}$ was synthesized and used for photocatalytic $CO_2$ conversion. Due to appropriate electronic band structure, good charge carrier lifetime and a defective and strained dual-phase structure, the material acted as a photocatalyst for $CO_2$ to CO conversion and $H_2O$ to $H_2$ production without

addition of any co-catalyst. The photocatalytic activity of this oxide was better than well-known anatase $TiO_2$ and $BiVO_4$ photocatalysts and comparable with P25 $TiO_2$ as a benchmark photocatalyst, suggesting high-entropy oxides as a new family of photocatalysts for $CO_2$ conversion.

In chapter 5, a high-entropy oxynitride with low bandgap, low electron-hole recombination, high $CO_2$ adsorbance and high chemical stability was introduced for photocatalytic $CO_2$ conversion. The material, which was synthesized using HPT and subsequent oxidation and nitriding, had two phases of face-centered cubic and monoclinic with a chemical composition of $TiZrNbHfTaO_6N_3$. The material had better photocatalytic $CO_2$ conversion performance compared with corresponding high-entropy oxide, benchmark photocatalyst P25 $TiO_2$ and all reported photocatalysts in the literature. This chapter opens a new path to developing highly efficient photocatalysts for $CO_2$ conversion.

All taken together, the main reason for the successful application of HPT to develop highly active photocatalysts for $CO_2$ conversion is that the method can simultaneously introduce some structural/microstructural features as effective strategies to enhance the activity. It was shown that the HPT method improves photocatalytic activity by increasing light absorbance, decreasing the optical bandgap, optimizing the electronic band structure, accelerating the electron-hole separation and migration and reducing the recombination rate of electrons and holes. The HPT method also contributed to the introduction of high-entropy photocatalysts which show high activity for $CO_2$ conversion.

Despite the high activity of HPT-processed photocatalysts, the mechanism for their high efficiency needs to be investigated further by employing theoretical calculations. Moreover, the catalysts produced by HPT have usually low surface area and new methods are expected to be developed to enhance the surface area of these catalysts. Although the HPT method has opened a new path to employing high-pressure and high-entropy phases as new photocatalysts, other synthesis methods should be used in the future for the large-scale production of these new catalysts. It is expected that HPT will continue its contribution to the field of photocatalysis, particularly due to the significance of developing a carbon-neutral society in recent years.

## Conference Presentations

[1] S. Akrami, M. Watanabe, T.H. Ling, T. Ishihara, M. Arita, M. Fuji, K. Edalati, High-pressure $TiO_2$-II polymorph as an active photocatalyst for $CO_2$ to CO conversion, *NanoSPD Conference*, Bangalore, India, February 26-March 3, 2023.

[2] S. Akrami, M. Watanabe, T.H. Ling, T. Ishihara, M. Arita, M. Fuji, K. Edalati, High-pressure $TiO_2$-II polymorph as an active photocatalyst for $CO_2$ to CO conversion, *The 59th Symposium on Powder Science and Technology*, Kyoto, Japan, December 21-23, 2022.

[3] S. Akrami, M. Watanabe, T.H. Ling, T. Ishihara, M. Arita, M. Fuji, K. Edalati, High-pressure $TiO_2$-II polymorph as an active photocatalyst for $CO_2$ to CO conversion, *Tokai Branch Meeting of Ceramic Society of Japan*, Nagoya, Japan, December 3, 2022.

[1] S. Akrami, M. Watanabe, T.H. Ling, T. Ishihara, M. Arita, M. Fuji, K. Edalati, High-pressure $TiO_2$-II polymorph as an active photocatalyst for $CO_2$ to CO conversion, *14th Pacific Rim Conference on Ceramic and Glass Technology (PACRIM 14)*, Vancouver, Canada, December 14, 2021.

## Peer-reviewed publications


[1] S. Akrami, P. Edalati, Y. Shundo, M. Watanabe, T. Ishihara, M. Fuji, K. Edalati, Significant $CO_2$ photoreduction on high-entropy oxynitride, Chemical Engineering Journal, Vol. 449, p. 137800.

[2] S. Akrami, Y. Murakami, M. Watanabe, T. Ishihara, M. Arita, Q. Guo, M. Fuji, K. Edalati, Enhanced $CO_2$ conversion on highly-strained and oxygen-deficient $BiVO_4$ photocatalyst, Chemical Engineering Journal, Vol. 442, pp. 136209.

[3] S. Akrami, Y. Murakami, M. Watanabe, T. Ishihara, M. Arita, M. Fuji, K. Edalati, Defective high-entropy oxide photocatalyst with high activity for $CO_2$ conversion, Applied Catalysis B: Environmental, Vol. 303, pp. 120896, 2022.

[4] S. Akrami, P. Edalati, M. Fuji, K. Edalati, High-entropy ceramics: Review of principles, production and applications, Materials Science and Engineering: R: Reports, Vol. 146, pp. 100644, 2021.

[5] S. Akrami, M. Watanabe, T.H. Ling, T. Ishihara, M. Arita, M. Fuji, K. Edalati, High-pressure $TiO_2$-II polymorph as an active photocatalyst for $CO_2$ to CO conversion, Applied Catalysis B: Environmental, Vol. 298, pp. 120566, 2021.

[6] S. Akrami, P. Edalati, M. Fuji, K. Edalati, High-pressure torsion for highly-strained and high-entropy photocatalysts, KONA Powder and Particle Journal, In Press.

[7] S. Akrami, T. Ishihara, M. Fuji, K. Edalati, Advanced photocatalysts for $CO_2$ conversion by severe plastic deformation (SPD), Materials, In Press.

**Acknowledgments**

I would like to express my deepest gratitude and sincere thanks to my supervisor, Prof. Masayoshi Fuji, for his full support and thoughtful guidance. I also appreciate Dr. Kaveh Edalati for his valuable contributions to perform this research work. I am also very grateful to Prof. Nobuyasu Adachi, Prof. Masaaki Haneda and Dr. Chika Takai for serving on my thesis committee and taking their time and energy to appraise my thesis. In addition, I am grateful for the support and encouragement that I have received from my parents and my wife during this difficult period of my life.